

INFORMATION TO USERS

This was produced from a copy of a document sent to us for microfilming. While the most advanced technological means to photograph and reproduce this document have been used, the quality is heavily dependent upon the quality of the material submitted.

The following explanation of techniques is provided to help you understand markings or notations which may appear on this reproduction.

1. The sign or "target" for pages apparently lacking from the document photographed is "Missing Page(s)". If it was possible to obtain the missing page(s) or section, they are spliced into the film along with adjacent pages. This may have necessitated cutting through an image and duplicating adjacent pages to assure you of complete continuity.
2. When an image on the film is obliterated with a round black mark it is an indication that the film inspector noticed either blurred copy because of movement during exposure, or duplicate copy. Unless we meant to delete copyrighted materials that should not have been filmed, you will find a good image of the page in the adjacent frame. If copyrighted materials were deleted you will find a target note listing the pages in the adjacent frame.
3. When a map, drawing or chart, etc., is part of the material being photographed the photographer has followed a definite method in "sectioning" the material. It is customary to begin filming at the upper left hand corner of a large sheet and to continue from left to right in equal sections with small overlaps. If necessary, sectioning is continued again—beginning below the first row and continuing on until complete.
4. For any illustrations that cannot be reproduced satisfactorily by xerography, photographic prints can be purchased at additional cost and tipped into your xerographic copy. Requests can be made to our Dissertations Customer Services Department.
5. Some pages in any document may have indistinct print. In all cases we have filmed the best available copy.

University
Microfilms
International

300 N. ZEEB RD., ANN ARBOR, MI 48106



8217403

Comaskey, Brian John

**COHERENT OPTICAL TRANSIENT STUDIES USING FREQUENCY
SWITCHING AND USING ARP EXCITATION**

The University of Arizona

PH.D. 1982

**University
Microfilms
International** 300 N. Zeeb Road, Ann Arbor, MI 48106

COHERENT OPTICAL TRANSIENT STUDIES USING FREQUENCY
SWITCHING AND USING ARP EXCITATION

by

Brian Comaskey

A Dissertation Submitted to the Faculty of the
COMMITTEE ON OPTICAL SCIENCES (GRADUATE)
In Partial Fulfillment of the Requirements
For the Degree of
DOCTOR OF PHILOSOPHY
In the Graduate College
THE UNIVERSITY OF ARIZONA

1 9 8 2

THE UNIVERSITY OF ARIZONA
GRADUATE COLLEGE

As members of the Final Examination Committee, we certify that we have read
the dissertation prepared by Brian J. Comaskey

entitled "Coherent Optical Transient Studies Using Frequency Switching
and Using ARP Excitation"

and recommend that it be accepted as fulfilling the dissertation requirement
for the Degree of Doctor of Philosophy.

St Jacobs

9/11/81
Date

Murray Foguel

9/11/81
Date

Richard L. Shoemaker

9/11/81
Date

Date

Date

Final approval and acceptance of this dissertation is contingent upon the
candidate's submission of the final copy of the dissertation to the Graduate
College.

I hereby certify that I have read this dissertation prepared under my
direction and recommend that it be accepted as fulfilling the dissertation
requirement.

Richard L. Shoemaker
Dissertation Director

March 23, 1982
Date

STATEMENT BY AUTHOR

This dissertation has been submitted in partial fulfillment of requirements for an advanced degree at The University of Arizona and is deposited in the University Library to be made available to borrowers under rules of the Library.

Brief quotations from this dissertation are allowable without special permission, provided accurate acknowledgement of source is made. Requests for permission for extended quotation from or reproduction of this manuscript in whole or in part may be granted by the head of the major department or the Dean of the Graduate College when in his judgment the proposed use of the material is in the interests of scholarship. In all other instances, however, permission must be obtained from the author.

SIGNED: Brian Comiskey

ACKNOWLEDGMENTS

This dissertation is the result of a protracted struggle to develop experimental expertise. That this work exists at all must be credited to my advisor, Richard L. Shoemaker. Only through his guidance and particularly his tolerance was I able to complete this research. To Rick I give my most heart-felt thanks.

I was further assisted and educated in this work through many long, often heated, but always enjoyable discussions with my co-workers. I therefore thank Ron Scotti, Jose Soto, Pam Davila, Carl Gaebe, and Eric Van Stryland for their helpfulness (not to mention sandwiches and chewing gum).

I also acknowledge my appreciation to the entire sixth floor cubicle crew who supplied the necessary environmental noise to keep me working at the Optical Sciences Center.

Finally, I thank Jeannette Gerl for typing this work and tolerating my sense of humor.

TABLE OF CONTENTS

	Page
LIST OF ILLUSTRATIONS.	vi
LIST OF TABLES	xi
ABSTRACT	xii
1. INTRODUCTION	1
2. A BRIEF OUTLINE OF THE THEORY OF COHERENT OPTICAL TRANSIENTS.	8
Basic Assumptions.	8
Development of Driven and Undriven Equations	13
The Vector Representation of the Coherent Optical Interaction	23
Extension of Theory to ARP	43
Two-pulse Delayed Nutation	48
Delayed Nutation using ARP System Preparation.	51
The Beam Profile Effects on Nutation	53
FID Effects in Nutation Studies.	53
Photon Echo.	55
3. THE FREQUENCY-SWITCHED LASER	58
The Layout of the Laser.	58
Laser Power Stability.	64
Laser Frequency Stability.	72
4. THE TRANSIENT SPECTROSCOPY LABORATORY SYSTEM	82
General Laboratory Layout.	82
Data Acquisition System's Linearity.	88
Data Taking Procedures	88
Basic Electrical and Timing Layout	92
5. THE SF ₆ EXPERIMENTS.	97
The Choice of Molecule and Transition.	97
Previous Work in SF ₆	97
Preliminary Work	98
The SF ₆ Data Runs.	104
The Reduction of the Nutation data	105
The Theory of Weak Velocity-Changing Collisions.	105
Echo Data Reduction and Results.	111
Conclusions and Discussion	120

TABLE OF CONTENTS--Continued

	Page
6. DELAYED NUTATION WITH ADIABATIC RAPID PASSAGE	
SYSTEM PREPARATION	122
Motivation	122
Optical ARP Background.	122
The Subject Gases	124
The Data Runs	
Data Reduction and Results.	133
Conclusions and Discussion.	140
LIST OF REFERENCES.	142

LIST OF ILLUSTRATIONS

<u>Figure</u>	<u>Page</u>
2.1	The two-level molecular system with pumping rates λ_A and λ_B and decay Γ_a and Γ_b 10
2.2	The vector representation of a two-level system in low temperature thermal equilibrium 19
2.3	The vector representation of a two-level system at 50% inversion. 20
2.4	The vector representation of a two-level system fully inverted. 21
2.5	The population inversion relaxation of a two-level system using the vector representation. 22
2.6	The vector representation of a two-level system under non-resonant steady-state excitation a) the pseudo-precision vectors components, b) the \underline{M} vector. . . 24
2.7	Description of the non-resonant steady-state excitation of two-level system with steady-state absorption including using the vector representation. . . 26
2.8	The vector representation of the two-level system under resonant Rabi flopping. 27
2.9	The vector representation of the two-level system under non-resonant Rabi flopping. 28
2.10	The vector representation of the two-level system under non-resonant Rabi flopping with population decay added 29
2.11	The vector representation of the two-level system commencing FID. 30
2.12	The vector representation of the two-level system undergoing FID with population decay. 31

LIST OF ILLUSTRATIONS--Continued

<u>Figure</u>	<u>Page</u>
2.13 The vector representation of the two-level system undergoing FID where $\gamma_{ab} > \gamma_a, \gamma_b$	32
2.14 The delayed notation experiment illustrated with the vector representation for a two-level system	33
2.15 The spread in \vec{F} vectors that must be considered due to the spread in contributing velocity groups.	35
2.16 The vector representation of Doppler-distributed two-level systems under steady-state excitation (allowing small steady-state absorption.	36
2.17 The vector representation of doppler-distributed two-level systems undergoing FID after steady-state excitation	37
2.18 The locus of points of the induced dipoles' phasors of a Doppler-distributed two-level gas after a $\pi/2$ pulse.	38
2.19 The dephasings of the macroscopic induced dipole of a two-level system via the resonant frequency spread	39
2.20 The effect of a π pulse on a Doppler-distributed two-level gas originally excited by a $\pi/2$ in the vector representation.	41
2.21 An ARP population inversion sweep in the vector representation	42
2.22 The doubly rotating co-ordinate frame ($\hat{U}'\hat{V}'\hat{W}'$) equations 2.24 with respect to the singly rotating frame ($\hat{U}\hat{V}\hat{W}$) equations 2.19.	44
2.23 An ARP population inversion sweep in the doubly rotating frame vector representation and assuming the \vec{M}' or \vec{F}' angle to be always maximized (worst case) . .	46
2.24 The two-functional terms S_0 and $2F_0$ versus $\kappa E_0 t$ from equations 2.35.	52
2.25 The two-pulse delayed nutation sequence experiment via frequency-switching or Stark-switching	54

LIST OF ILLUSTRATIONS--Continued

<u>Figure</u>	<u>Page</u>
3.1	The frequency-switched laser. 59
3.2	A typical cross-section scan of the frequency-switched laser's beam before the absorption cell. 61
3.3	The cross-section of the CdTe modulation mount. 62
3.4	The beat signal of a frequency-switched pulse with the output of another stable cw CO ₂ laser 66
3.5	An oscilloscope photograph (20μs/cm) of the frequency-switched laser's output for two slightly different cavity tunings of the same line indicating a change in polarity of the large switching. 67
3.6	An oscilloscope photograph (20μs/cm) of the frequency-switched laser's output for two slightly different cavity tunings of the same line indicating that the large switching transient can be reduced to zero by proper tuning. 67
3.7	A large transient producing frequency-switch as viewed with the laser gain frequency distribution. 68
3.8	Frequency-switching without large transients as viewed with the laser gain frequency distribution. 70
3.9	An oscilloscope photograph of the large transient produced by a 500 volt 8μs pulse on the crystal (2ps/cm). 73
3.10	A computer simulation of figure 3.9 using equations (3.5) (200μs/point) 73
3.11	A computer simulation of figure 3.9 using equations (3.5) and allowing a 40% spread in light intensity through activities region viewed. 73
3.12	An oscilloscope photograph of the <u>chopped</u> laser output with the large transient tuned to zero. 74
3.13	The frequency stabilization scheme for the frequency-switched laser. 79
3.14	How the laser stabilizer error signal varies with various detunes 80

LIST OF ILLUSTRATIONS--Continued

<u>Figure</u>		<u>Page</u>
4.1	The lab setup for frequency-switched experiments.	83
4.2	The lab setup for ARP experiments.	84
4.3	The boxcar window control scheme for delayed-nutation and photo echo experiments	87
4.4	A demonstration of system linearity with typical running parameters using a linear voltage ramp into the boxcar.	89
4.5	A demonstration of the breaking of system linearity with larger input signals than in figure 4.4.	90
4.6	The scheme for the initial data extraction from raw data in delayed nutation.	93
4.7	The scheme for the initial data extraction from raw data in photon echo experiments	93
4.8	The timing schemes for the coherent transient experiments .	94
5.1	The x-y plotter output for one pressure of early raw data on photon echo experiments in SF ₆	99
5.2	A plot for one pressure of early reduced data on photo echo experiments in SF ₆	100
5.3	A plot of the slopes from linear least-squares best fits to the early data versus pressure.	101
5.4	A photon echo train taken after the computer based data acquisition system was completed	102
5.5	A plot of the reduced data for one pressure clearly indicating a non-exponential decay.	103
5.6	A typical set of delayed-nutations taken at one pressure for different delays	106
5.7	A typical plot for one pressure of reduced delayed nutation data indicating a simple exponential decay	107
5.8	A plot of the simple exponential decay rate obtained for each pressure studied by delayed nutation versus pressure.	108

LIST OF ILLUSTRATIONS--Continued

<u>Figure</u>	<u>Page</u>
5.9 A plot of the linear coefficient from the best fit of equation 5.4 to the first 10 points of each pressure run of the echo experiments versus pressure.	113
5.10 A plot of the cubic coefficient from the best fit of equation 5.4 to the first 10 points of each pressure run of the echo experiments versus pressure. . . .	114
5.11 A representative plot of one pressure run of the echo experiment to show the apparent t^5 behavior for short delay times	115
5.12 A plot of one pressure run of the echo experiment and the least-squares best fit of equation 5.8 to it.	117
5.13 A plot of the ΔU parameter obtained for each pressure by least-squares best fitting equation 5.8 versus pressure.	118
5.14 A plot of the Γ_{vc} parameter obtained for each pressure by least-squares best fitting equation 5.8 versus pressure.	118
6.1 The adiabatic rapid passage sweep and pulse probe sequence studied here.	126
6.2 The effect of hindered motion on molecular level structure	127
6.3 The transition studied in the $N^{15}H_3$ work.	130
6.4 The transition studied in the $N^{14}H_3$ work.	132
6.5 An x-y plot of early ARP experiment	134
6.6 A plot of nutation data from $N^{15}H_3$ at 4mTorr and its simple exponential decay best fit curve	135
6.7 A plot of the least-squares obtained simple exponential decay rate for each pressure run of the $N^{14}H_3$ experiments versus pressure	137
6.8 A plot of the least-square obtained simple exponential decay rate for each pressure run of the $N^{15}H_3$ experiments versus pressure	138

LIST OF TABLES

<u>Table</u>		<u>Page</u>
3.1	Laser Parameters	64
3.2	Crystal Data	64
5.1	Comparison of measurements for $^{13}\text{CH}_3\text{F}$, $^{14}\text{NH}_2\text{D}$, and SF_6	119
6.1	NH_3 parameters	128
6.2	NH_3 Experimental parameters.	133
6.3	NH_3 Experimental results	139

ABSTRACT

Two different time-resolved spectroscopic techniques are discussed theoretically and demonstrated experimentally in dilute gases.

The first technique involves extending the advantages of Stark-effect based time-resolved spectroscopy to non-polar molecules. This involves the development of a stable, TEM₀₀ mode, cw, CO₂ laser capable of switching rapidly and controllably between two frequencies. Design problems and output characteristics are discussed.

The frequency switchable laser is applied to the CO₂ 10.6 μ m P(16) coincidence with the non-polar molecule SF₆. The population relaxation time, T₁, is measured using two-pulse delayed nutation. The decay of induced dipoles is studied using the phenomenon of photon echoes. It is found that the echoes decay in a manner characteristic of dephasing dominated by velocity-changing collisions. A fit of the data to a model for such decays gives values of $\gamma_{ab} \equiv 1/T_2$ (the non-velocity-changing contribution to the dipole decay rate), Γ_{VC} (the total probability of a velocity-changing collision per unit time), and Δu which is related to the mean velocity change of SF₆ upon a velocity changing collision. A comparison with the published results of the similar Stark experiments on C¹³H₃F are made.

The second technique involves the development of an alternative to the pulsed excitation typically used in time-resolved T₁ studies. This involves inversion of a portion of the velocity distribution by

adiabatic rapid passage (ARP) techniques. The center of this portion is then probed in the manner of previous delayed nutation experiments. The system preparation is shown theoretically to be different and simpler than the pulsed case. In addition, ARP preparation gives a larger signal than two-pulse delayed nutation experiments.

ARP experiments on $N^{14}H_3$ and $N^{15}H_3$ are described and compared to two-pulse delayed nutation experiments. The single exponential decay best fits to the data from the two methods are found to be in agreement.

We would expect the $N^{15}H_3$ results to be very similar to the $N^{14}H_3$ results, though reduced rotational resonance effects in its upper state should give it an overall slower decay. It is indeed found that the decay appears to be a simple exponential as did the $N^{14}H_3$ data over the time range studied. The pressure dependent single exponential decay rate for $N^{15}H_3$ is however roughly 45% larger than the rate for $N^{14}H_3$ in the pressure range from 0.5 to 9 mTorr.

CHAPTER 1

INTRODUCTION

Coherent optical transients are the optical responses of matter to changes in applied coherent radiation observed for times less than the material system's relaxation times. What generally is observed is the transient optical behavior (absorption or emission) of a sample due to a change in the intensity and/or frequency of the applied radiation. This form of spectroscopy can be used to resolve, measure, and compare with theoretical models, detailed collisional contributions to the relaxation of a population inversion and the decay of the macroscopic induced dipole, determine narrow line splittings which can be seen as beats in the system's radiation, measure the transition dipole matrix elements between levels, and make many other detailed studies of optical transitions. The techniques applied in such studies are analogous to nuclear magnetic resonance (NMR) experiments as are the working equations of the optical interaction. One incentive for optical time-resolved spectroscopy research is the hope that it can be developed to the level of power as the well developed field of NMR. Another motivation is that such experiments stand as a test for the theories which describe dynamics of the interaction of coherent radiation with matter.

In the work presented here, the relaxation of population inversions and the decay of induced dipoles in dilute gas samples are studied in the infrared. There are two basic aims in this work. First, there is the development and testing of a laser system and techniques to open

up previous high resolution techniques to a larger selection of molecules. A second aim is to develop and test an alternate perturbing method which produces a greater inversion in the test gases for transient studies.

Population relaxation is studied here by the technique of delayed nutation. In essence, this technique involves disturbing a system from thermal equilibrium (normally by a pulse of resonant coherent light) and then at some later time passing resonant radiation through the sample and monitoring the initial absorption of this radiation. A fully relaxed gas gives the most absorption, and the extent of absorption decreases as the sample system approaches zero population difference. If the system has an inverted population difference, one sees emission. Hence, by varying the delay time and repeatedly monitoring the initial absorption, we can map out in time how the sample system's population relaxes back to thermal equilibrium.

For dilute gases, as studied here, relaxation processes that are due to collisions should be directly dependent on the pressure. To measure the collisional component of the decay one typically repeats the above experimental sequence for a range of pressures and then plots the obtained decay rates of each sequence versus pressure.

The decay of the induced macroscopic dipole in the sample is studied by the technique of photon echo. A gas in thermal equilibrium has no macroscopic dipole moment. If this gas is exposed to a pulse of coherent radiation, each interacting molecule responds to the driving force of the field, inducing an oscillating charge displacement. This oscillation has a fixed phase relationship to the driving field in the

same manner as the displacement of a mass on a spring has a phase relationship to an applied oscillatory force. As the driving field is coherent, the phase of the field is well determined between any two spatial separations. Hence, there exists a simple (linear) phase relationship for the phase of the oscillating dipoles of molecules separated by any distance within the gas sample length. We thus have established a coherent macroscopic array of dipoles. In steady state, this macroscopic array radiates a beam of coherent radiation in the direction of the applied field, but 180° out of phase, giving in sum with the applied field the result of steady-state absorption.

If we suddenly turn off the driving radiation, each molecular dipole continues to oscillate, just as a mass on a spring continues to oscillate after the driving force has been removed. The oscillating macroscopic dipole does not immediately disappear, but continues to radiate coherently. This radiation is referred to as free induction decay (FID), in analogy to NMR. With the passage of time, this induced macroscopic dipole decays due to the decay of the constituent dipoles and due to the many microscopic dipoles in the array falling out of synchronization. The first sort of decay involves any process which contributes to the relaxation of the population differences as such processes represent basically a removal of the molecule from the levels involved in the transition. The second type of macroscopic dipole decay can be due to collisional processes which interrupt the phase of oscillating molecular dipoles (Phase Interrupting Collisions) and to collisions which change the velocity (but not the quantum state) of the excited molecule by a small amount and hence its lab frame frequency.

For the gases studied here, the dominant mode of decay of the macroscopic dipole is by yet another contribution to the second type of decay. This process is ergodic, unlike the previous ones. The laser radiation interacts not just with the exactly resonate velocity group but with a spread of velocity groups in the gas's velocity distribution centered about the laser frequency. Without the individual molecular dipole oscillations being forced by a driving field, each molecular dipole oscillates at its own frequency. This spread in frequency allows the constituent dipoles of the macroscopic dipole to get "out of step" with each other.

In photon echo experiments, after a delay time t , a second special pulse of coherent resonant radiation is applied to the system. This pulse is called a π pulse. After the pulse, the dipoles continue to oscillate at their own frequency, but with a phase added to their oscillation such that the phase difference between the dipoles decreases, i.e. it appears that they are moving backward in time. Thus, after another equal time t , all the velocity groups will once again be oscillating synchronously, and the macroscopic dipole is reconstituted. Over-all, this rephasing can be understood by the analogy of runners on a race track. At $t=0$ all the runners start off at the same line. As the runners race around the track, they become spread out according to their different speeds. If at time t_0 they all turn 180° and run back at their previous speed, then at $t=2t_0$ they will all cross the original start line together.

We see that by the echo technique, we can get around the effects of frequency inhomogeneity in the gas. If we perform the echo experiment

for many different pulse separations, we can resolve the homogeneous decay contributions. If we repeat this series of experiments for many pressures we can resolve the pressure dependent, thus collisionally dependent, components of this decay.

In pursuit of the first aim of this work, a frequency-switched cw CO₂ laser has been developed to perform the above experiments. This system replaces pulsed laser techniques and techniques which use a cw laser with Stark tuning of the resonance. In the pulsed system, the laser pulses described above are produced by the laser and are used to probe a gas sample in a simple sealed cell. In the latter case, the subject gas is Stark tuned into and out of resonance with a cw laser beam. The subject gas is in a specially constructed cell containing two precision spaced flat electrodes wired to high voltage pulsed electronics. The pulsed laser case has the advantage of applicability of any sample that has a transition which overlaps one of the many CO₂ lines. The pulsed laser technique suffers to the extent that the detection of the small transient signal may be buried in the large laser pulses. Also, pulse control and repeatability is generally poor with a pulsed system. This problem can be partially overcome by using an electro-optically chopped output of a cw laser. The Stark technique has the disadvantage of being applicable to only those molecular transition overlaps to CO₂ that have large Stark effects. This technique also limits the range of pressures that can be studied due to gas breakdown across the Stark plates. Laser beam cross sections must also be kept small to pass through the closely placed Stark plates which enhances

undesirable molecular transit time contributions to signal decay. On the other hand, the Stark technique allows for very precise electrical control of the timing and repetition of the pulse sequences. There are no large transients from the laser to obscure the desired signals. Also, a further signal increase is possible in the Stark technique through heterodyne detection since the Stark detuned gas's emission will beat with the strong cw laser beam's field.

With the frequency-switched cw-power laser, we combine the advantages of both the above systems. The frequency switching is easily and precisely controlled by electronics. The absorption cell is simple with no beam diameter restrictions, and we are not limited to polar molecules. There are no large power transients into the detector. Finally, heterodyne signal detection is possible with this system.

The second aim of this work has been to investigate an alternative method of system preparation for delayed nutation experiments. Traditionally, the sample has been driven from thermal equilibrium of a pulse of resonant coherent radiation. For a gas the radiation will be resonant only for the center of the hole burnt in the velocity distribution. Thus, there will be a spread in the state of excitation of the interacting molecules. This is in addition to the Gaussian beam profile effect which also tends to produce a spread in the degree of excitation of the observed molecules (this latter case can be minimized by use of large beam cross sections). The result is that only absorption nutation signals are obtainable from pulse-prepared gases. The alternative system preparation studied here is adiabatic rapid passage (ARP). This

technique involves sweeping the laser frequency from a large detuning above or below the molecular transition frequency through resonance and on to a large detuning of the opposite sign. The adiabatic aspect is that many Rabi flopping cycles must occur before there is any appreciable change in the laser frequency. This means that the sweep is slow enough for molecular populations to respond to the radiation field at each point in the frequency sweep. The "rapid" aspect is that the duration of the sweep is less than the characteristic decay times of the molecules. This technique is capable of inverting a transition across a range of the Doppler frequency distribution. This range can be much larger than the hole burned by a pulse of fixed frequency coherent radiation. Furthermore, beam profile effects enter less strongly here than in pulsed excitation experiments. Even for narrow beams, if all of that portion of the beam intercepted by the detector is only greater than a minimum intensity determined by the adiabatic condition, then all contributing velocity groups will still see the same excitation process. In this case, all the velocity groups that will contribute to a nutation signal can be inverted to an equal extent. Thus, a larger signal should be available from this technique. In fact, emissive nutation signals should be obtainable.

The spirit of these studies is more to test, develop, and evaluate the methods rather than to obtain high resolution data on these gas systems. For this reason systems which have been studied previously in the literature were used.

CHAPTER 2

A BRIEF OUTLINE OF THE THEORY OF COHERENT OPTICAL TRANSIENTS

Basic Assumptions

This chapter is an outline of the basic theoretical concepts behind the delayed nutation and photon echo experiments discussed in the following chapters. This outline draws heavily on Richard Shoemaker's work (Shoemaker, 1978).

In the theoretical development we make the following assumptions:

1. The dominant interactions are molecule-molecule and molecule-radiation field. We can ignore three or higher order molecular-interactions since the gases studied are dilute. Nonbinary collisions are ignored since at the pressures used (less than 20 mtorr) and with typical cross sections (a few hundred \AA^2), the collisional rates are of order MHz while collision interaction times are of order picoseconds. We can ignore molecular-molecular-field interactions since over the duration of the collision, field driven effects are negligible. The rate of driven effects go basically as $w_{\text{rad}} - w_{\text{laser}}$ or $\frac{\mu_T E_0}{h}$ (μ_T being the transition dipole matrix element and E_0 the field), both of these frequencies in our experiments being in MHz.
2. The molecule-molecule interaction is totally dominated by the absorber-nonabsorber decay channels. By this is meant that collision decay effects on the molecule under study are due to interactions with only one type of molecule, the non-resonant molecule. In our experiments only a small fraction of the sample gas under study is

near resonance with the laser light at any one time. The laser typically "burns" a hole in the gas's Doppler distribution of frequencies less than 1 MHz wide, while the width of the distribution is more like 100 MHz. Thus a resonant molecule will collide with only nonresonant molecules.

3. The molecule-field interaction can be described by the two-level atom model. This is a matter of the selection of the subject system. In chapter 6 calculations are presented on the $N^{14}H_3$ transition used in the ARP experiment, as there exists the possibility of multiple line coupling due to the nuclear electric quadrupole effects. In the frequency switched experiment a line is chosen that is free of hot band contributions. Since there is no static field, there is a degeneracy in M_j but with the selection rule being $\Delta M_j = 0$ each transition should behave as an independent two-level transition.

4. The pumping and decay terms for both levels involved in the interactions are independent of the laser field. The justification for this is that the overwhelming majority of the molecules present are noninteracting. An important consequence of this assumption is that such pump terms should contribute no net dipole to the resonant system. See Figure 2.1.

5. We disregard velocity changing (VC) collisions. A collision can change the state of the absorber or interrupt the phase of the absorber's induced dipole, and/or change the velocity of the absorber, thus causing a shift in the resonant frequency in the laboratory frame. To ignore VC collisions may not always be valid. In chapter 5 it is explained how VC effects are transparent to delayed nutation experiments. In echo

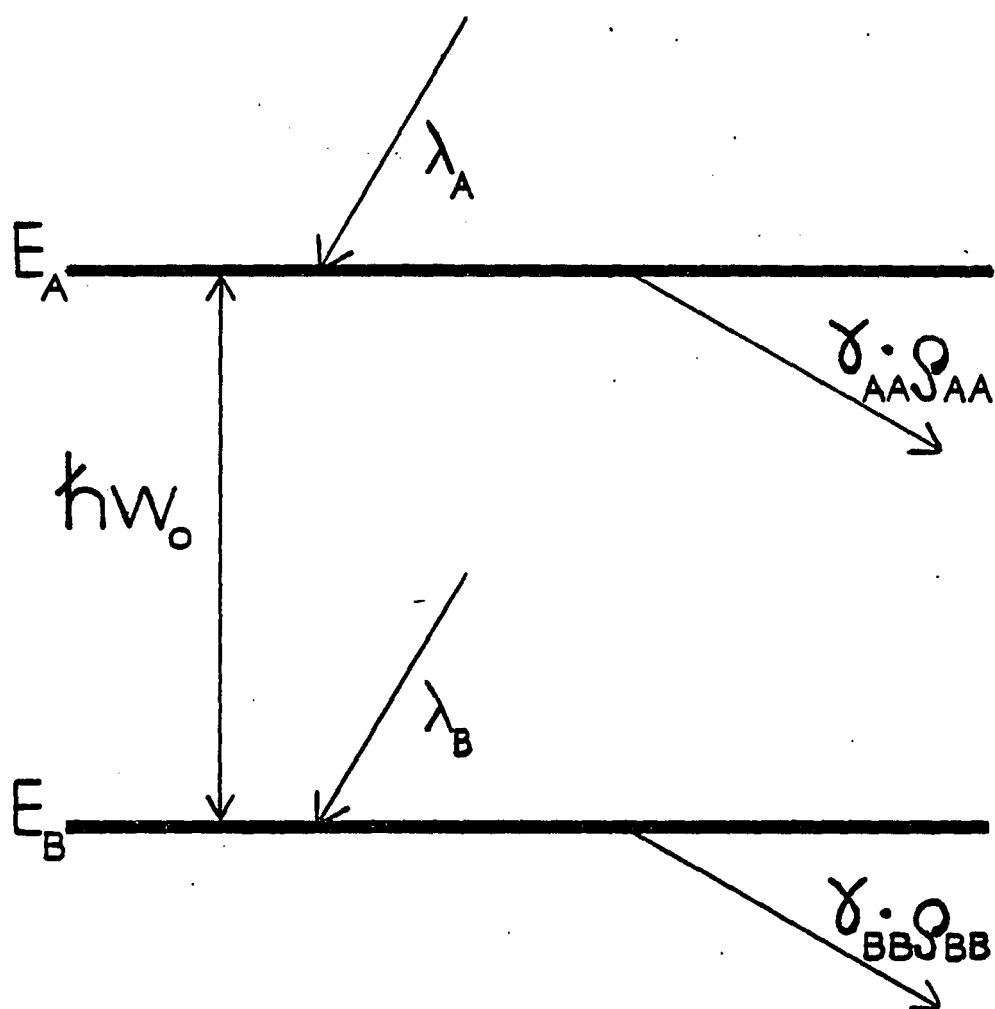


Figure 2.1. The two-level molecular system with pumping rates λ_A and λ_B and decay rates Γ_a and Γ_b .

experiments VC effects can be very evident. To retain VC effects in the theory leads to very complicated equations without changing the dynamics of echo formation. In this chapter we drop VC effects to more clearly explain echo formation and echo experiments. VC effects are discussed in Chapter 5.

6. The molecular velocities can be treated nonrelativistically. At room temperatures, gas thermal velocities are of order 100 m/sec. which is clearly nonrelativistic.

7. The molecular-field interaction can be described using semi-classical theory. This should certainly be valid as we are not dealing with spontaneous emission effects.

8. The driving radiation is a plane wave. In reality we have a Gaussian laser profile through the media. This profile manifests itself in two ways. First, by way of the molecular transit time, a pressure independent component is contributed to $1/T_1$. It appears adequate to treat this "decay channel" as exponential in time (Hall, 1973, 1975). Since this component is pressure independent, it is easily distinguishable from collisional effects. The second effect is that driven signal expressions derived using plane wave fields should be averaged over the range of field strengths intercepted in the detector area. In the frequency switched experiments this should not change anything as the beam waist is about 20 times larger than the detector diameter. In the ARP experiments the beam waists were much smaller. However, even here the averaging would not change any of the essential plane wave conclusions. Driven effects averaged over a spread in field strengths would simply damp the oscillatory signals more rapidly (Shoemaker and

Van Stryland, 1976), due to the spread in the Rabi Flopping frequency. The details of the driving effects that we are concerned with occur in the first half-cycle of the Rabi flop. This minimizes the importance of such a spread.

9. The dipole approximation can be applied. This is true because the experiments are done using the 10.6 μm band of the CO_2 laser. The molecular dimensions are very much less than this wave length of light.

10. The gas is optically thin. By this is meant that we can consider the laser field amplitude as invariant along the length of the absorption cell. This is not a severe assumption at the gas pressures used in the lab, and can easily be verified by checking the laser power out of the cell while it is charged against the power out while it is pumped out.

11. The rotating wave approximation (RWA) can be applied. The RWA is an approximation in which the highest frequency driving terms in the interaction of light with matter are neglected. These highest frequencies are optical frequencies. Material systems' responses are slow compared to the optical period so that if other driving terms are much lower than optical frequencies, they will dominate the molecule's behavior (Sargent et al., 1977). These other driving terms in the two-level system go as the differences of the system's resonance frequency and the laser frequency. In our work this difference is of order a few MHz.

12. The details of the decay processes are unimportant while the two-level system is being driven by the field. For the experiments conducted here this was the case simply because the duration of the

resonant fields were of order a few hundred nanoseconds while the field free delay times and the signal decay times were measured in microseconds

Development of Driven and Undriven Equations

The semi-classical Schrodinger equation for a molecule in a coherent field is, using the dipole approximation and the Coulomb gauge,

$$(-\hbar^2 \sum_j \frac{1}{2m_j} [\vec{\nabla}_j - \frac{e}{c} \vec{A}(R,t)]^2 + V(\vec{r}_j))\psi = i\hbar \frac{\partial}{\partial t} \psi \quad (2.1)$$

where R is the center of mass co-ordinate and \vec{r}_j is the coordinate of the j^{th} nucleous or electron and m_j is the mass of the j^{th} element. Assuming optically thin media and nonrelativistic Doppler shifts, a molecule in a velocity group with a velocity component V_z collinear with the laser beam, sees a field which can be written

$$\vec{E}(z,t) = \hat{x} E_0(t) \cos[(\Omega - KV_z)t - K(z - V_z t)] \quad (2.2)$$

where Ω is the laser frequency.

In Sargent, Scully, and Lamb (Sargent et al., 1977) a unitary transformation is shown which transforms equation (2.2) into

$$(-\hbar^2 \sum_j \frac{1}{2m_j} \vec{\nabla}_j^2 + V(\vec{r}_j) - E(z,t) \cdot \sum_j \vec{r}_j \cdot \vec{e}_j)\phi = i\hbar \frac{\partial}{\partial t} \phi \quad (2.3)$$

where it is noted that $V(\vec{r}_j)$ does not contain parital derivative operators.

We now write (2.3) in density matrix form, adding a phenomenological decay term. We get

$$\dot{\hat{\rho}}_{ij} = \frac{-i}{\hbar} \sum_n (H_{in} \hat{\rho}_{nj} - \hat{\rho}_{in} H_{nj}) - \gamma_{ij} \hat{\rho}_{ij} \quad (2.4)$$

where

$$H_{in} = \langle \phi_i | H_0 - e_j \vec{E}(z, t) \cdot \sum \vec{r}_j | \phi_n \rangle$$

$$= \epsilon_i \delta_{in} - \mu_{in} E_0 \cos[(\Omega - KV_z)t - K(z - V_z t)](1 - \delta_{in}) \quad (2.5)$$

H_0 is the unperturbed part of the Hamiltonian, and μ_{in} is the transition dipole matrix element between i and n . We note that by proper choice of the arbitrary phases of the basis wave functions, μ_{in} can be taken as real.

Equation (2.4) deals with only one two-level system in some state, α . The experiments are based on Doppler broadened gases. Thus, it is desirable to formulate the equations of motion in terms of an ensemble of molecules. To this end, the population matrix (Sargent et al., 1977) is used. The population matrix is defined as

$$\rho_{ij}(z, V_z, t) = \sum_{\alpha} \lambda_{\alpha}(V_z) \int_{-\infty}^t dt \hat{\rho}_{ij}(\alpha, z_0 = z - V_z(t - t_0), t - t_0) \quad (2.6)$$

where $\lambda_{\alpha}(V_z)$ is the rate at which molecules enter the state α , t_0 is the time at which the molecule enters the state α , and z_0 is the location where this occurred. Taking the time derivative on both sides of (2.6) gives

$$\begin{aligned} \frac{d}{dt} \rho_{ij}(z, V_z, t) &= \sum_{\alpha} \lambda_{\alpha}(V_z) [\hat{\rho}_{ij}(\alpha, z, 0) \\ &+ \int_{-\infty}^t [V_z \frac{\partial}{\partial z_0} \hat{\rho}_{ij}(\alpha, z - V_z(t - t_0), t - t_0) \\ &+ \frac{\partial}{\partial t} \hat{\rho}_{ij}(\alpha, z - V_z(t - t_0), t - t_0)] dt_0] \end{aligned} \quad (2.7)$$

We expect the first integrand to go as $v_z K \hat{\rho}$, where K is the wave number,

while the second should go roughly as $\omega \hat{\rho}$. Since the velocities are nonrelativistic, we can ignore the first integrand. By definition of t_0 and the assumption that the pump terms do not contribute off-diagonal terms,

$$\hat{\rho}_{ij}(\alpha, z, 0) = \delta_{ij} \delta_{\alpha i}. \quad (2.8)$$

Combining (2.8), (2.7), and (2.4) we find

$$\begin{aligned} \dot{\rho}_{ij}(z, V_z, t) = & \lambda_i \delta_{ij} - \frac{i}{\hbar} \int_n [H_{in} \delta_{nj}(z, V_z, t) - \rho_{in}(z, V_z, t) H_{nj}] \\ & - \gamma_{ij} \rho_{ij}(z, V_z, t) \end{aligned} \quad (2.9)$$

In zero field equilibrium

$$\dot{\rho}_{ii} = 0 = \lambda_i - \gamma_{ii} n_i; \quad n_i \equiv \delta_{ii} \text{ at equilibrium.} \quad (2.10)$$

Combining equations (2.5), (2.10), and (2.9) and noting that we are assuming a two-level system as in Figure 1.1, we get

$$\begin{aligned} \dot{\rho}_{aa} &= n_a \gamma_a + i \tilde{\kappa} E_0 \cos(\Omega' t - Kz') (\rho_{ba} - \rho_{ab}) - \gamma_a \rho_{aa} \\ \dot{\rho}_{bb} &= n_b \gamma_b + i \tilde{\kappa} E_0 \cos(\Omega' t - Kz') (\rho_{ab} - \rho_{ba}) - \gamma_b \rho_{bb} \\ \dot{\rho}_{ab} &= (-i\omega_0 - \gamma_{ab}) \rho_{ab} + i \tilde{\kappa} E_0 \cos(\Omega' t - Kz') (\rho_{bb} - \rho_{aa}) - \gamma_{ab} \rho_{ab} \\ \rho_{ab} &= \rho_{ab}^* \end{aligned} \quad (2.11)$$

with $\gamma_a \equiv \gamma_{aa}$; $\gamma_b \equiv \gamma_{bb}$; $\Omega' \equiv \Omega - KV_z$, $z' \equiv z - V_z t$, and $\tilde{\kappa} \equiv \mu_{ab}/\hbar$.

Factoring the high frequency variation out of the dipole term by defining

$$\tilde{\rho}_{ab} \equiv \rho_{ab} e^{i(\Omega' t - Kz')}, \quad (2.12)$$

writing the cosine terms using complex exponentials, and applying the RWA, we find:

$$\begin{aligned}
\dot{\rho}_{aa} &= n_a \gamma_a + i \frac{\tilde{\kappa} E_0}{2} (\tilde{\rho}_{ba} - \tilde{\rho}_{ab}) - \gamma_a \rho_{aa} \\
\dot{\rho}_{bb} &= n_b \gamma_b + i \frac{\tilde{\kappa} E_0}{2} (\tilde{\rho}_{ab} - \tilde{\rho}_{ba}) - \gamma_b \rho_{bb} \\
\dot{\tilde{\rho}}_{ab} &= [i(\Omega' - \omega_0) - \gamma_{ab}] \tilde{\rho}_{ab} + i \frac{\tilde{\kappa} E_0}{2} (\rho_{bb} - \rho_{aa}) \\
\tilde{\rho}_{ba} &= \rho_{ab}^*
\end{aligned} \tag{2.13}$$

Equations (2.13) can be written in a physically meaningful form by defining

$$\begin{aligned}
U &= \tilde{\rho}_{ab} + \tilde{\rho}_{ab}^* \\
V &= i(\tilde{\rho}_{ab} - \tilde{\rho}_{ab}^*) \\
W &= \rho_{aa} - \rho_{bb} \\
S &= \rho_{aa} + \rho_{bb}
\end{aligned} \tag{2.14}$$

S describes the total population in the two-level system, W describes its population difference, $\mu_{ab} U$ is the in-phase induced dipole, and $\mu_{ab} V$ is the (90°) out of phase component. Using equation (2.14), equations

(2.13) become:

$$\begin{aligned}
\dot{U} &= \delta V - \gamma_{ab} U \\
\dot{V} &= -\delta U + \tilde{\kappa} E_0 W - \gamma_{ab} V \\
\dot{W} &= n_a \gamma_a - n_b \gamma_b - \tilde{\kappa} E_0 V - \frac{1}{2}(\gamma_a + \gamma_b)W - \frac{1}{2}(\gamma_a - \gamma_b)S \\
\dot{S} &= n_a \gamma_a + n_b \gamma_b - \frac{1}{2}(\gamma_a + \gamma_b)S - \frac{1}{2}(\gamma_a - \gamma_b)W
\end{aligned}$$

where $\delta \equiv \Omega' - \omega_0$.

If we assume that the boundary conditions are defined at time t_s , the zero field solutions are

$$\begin{aligned}
 U &= [U(t_s)\sin(\delta(t - t_s)) + V(t_s)\cos(\delta(t - t_s))]e^{-\gamma_{ab}t} \\
 V &= [U(t_s)\cos(\delta(t - t_s)) - V(t_s)\sin(\delta(t - t_s))]e^{-\gamma_{ab}t} \\
 S &= n_a(1 - e^{-\gamma_a t}) + n_b(1 - e^{-\gamma_b t}) + \left(\frac{e^{-\gamma_a t} - e^{-\gamma_b t}}{2}\right)w + \left(\frac{e^{-\gamma_a t} + e^{-\gamma_b t}}{2}\right)S \\
 W &= n_a(1 - e^{-\gamma_a t}) - n_b(1 - e^{-\gamma_b t}) + \left(\frac{e^{-\gamma_a t} + e^{-\gamma_b t}}{2}\right)w \\
 &\quad + \left(\frac{e^{-\gamma_a t} - e^{-\gamma_b t}}{2}\right)S
 \end{aligned} \tag{2.16}$$

In this work we assume that the driving radiation is on for times much less than the decaytime of the system. Thus, after the pulse, S has not changed significantly from its equilibrium value. For $\gamma_a = \gamma_b$ or for the above type pulses we get the following:

$$\begin{aligned}
 U &= [U(t_s)\sin(\delta(t - t_s)) + V(t_s)\cos(\delta(t - t_s))]e^{-\gamma_{ab}t} \\
 V &= [U(t_s)\cos(\delta(t - t_s)) - V(t_s)\sin(\delta(t - t_s))]e^{-\gamma_{ab}t} \\
 W &= (n_a - n_b)\left[1 - \left(\frac{e^{-\gamma_a(t - t_s)} + e^{-\gamma_b(t - t_s)}}{2}\right)\right. \\
 &\quad \left. + \left(\frac{e^{-\gamma_a(t - t_s)} - e^{-\gamma_b(t - t_s)}}{2}\right)\right]w(t_s)
 \end{aligned} \tag{2.17}$$

The steady-state solutions of (2.15) give us the state of the system driven by the laser radiation for long times. We find

$$\begin{pmatrix} U \\ V \\ w \end{pmatrix} = \frac{(\gamma_a + \gamma_b)(n_a - n_b)}{(\gamma_a + \gamma_b)(\gamma_{ab}^2 + \delta^2) + 2\gamma_{ab}\tilde{\kappa}E_0} \begin{pmatrix} \delta\tilde{\kappa}E_0 \\ \gamma_{ab}\tilde{\kappa}E_0 \\ \gamma_{ab}^2 + \delta^2 \end{pmatrix} \quad (2.18)$$

Assuming that the laser field interaction times are short compared to the decay times of the system, we can reduce the equations (2.15) to:

$$\begin{aligned} \dot{U} &= \delta V \\ \dot{V} &= -\delta U + \tilde{\kappa}E_0\omega \\ \dot{W} &= -\kappa E_0 V \end{aligned} \quad (2.19)$$

If the field was turned on at time t_s , the solutions to (2.19) for small variation in S would be

$$\begin{aligned} U(t) &= U(t_s) \left[1 - \frac{\delta^2}{2} (1 - \cos[g(t - t_s)]) \right] + V(t_s) \frac{\delta}{g} \sin(g(t - t_s)) \\ &\quad + w(t_s) \frac{\delta\tilde{\kappa}E_0}{g} (1 - \cos(g(t - t_s))) \\ V(t) &= -U(t_s) \frac{\delta}{g} \sin(g(t - t_s)) + V(t_s) \cos(g(t - t_s)) + w(t_s) \frac{\tilde{\kappa}E_0}{g} \sin(g(t - t_s)) \end{aligned} \quad (2.20)$$

$$\begin{aligned} w(t) &= U(t_s) \frac{\delta\tilde{\kappa}E_0}{g} (1 - \cos[g(t - t_s)]) - V(t_s) \frac{\tilde{\kappa}E_0}{g} \sin(g(t - t_s)) \\ &\quad + w(t_s) \left[1 - \frac{\tilde{\kappa}^2 E_0^2}{2} (1 - \cos[g(t - t_s)]) \right] \end{aligned}$$

where $g = \sqrt{(\tilde{\kappa}E_0^2 + \delta^2)}$

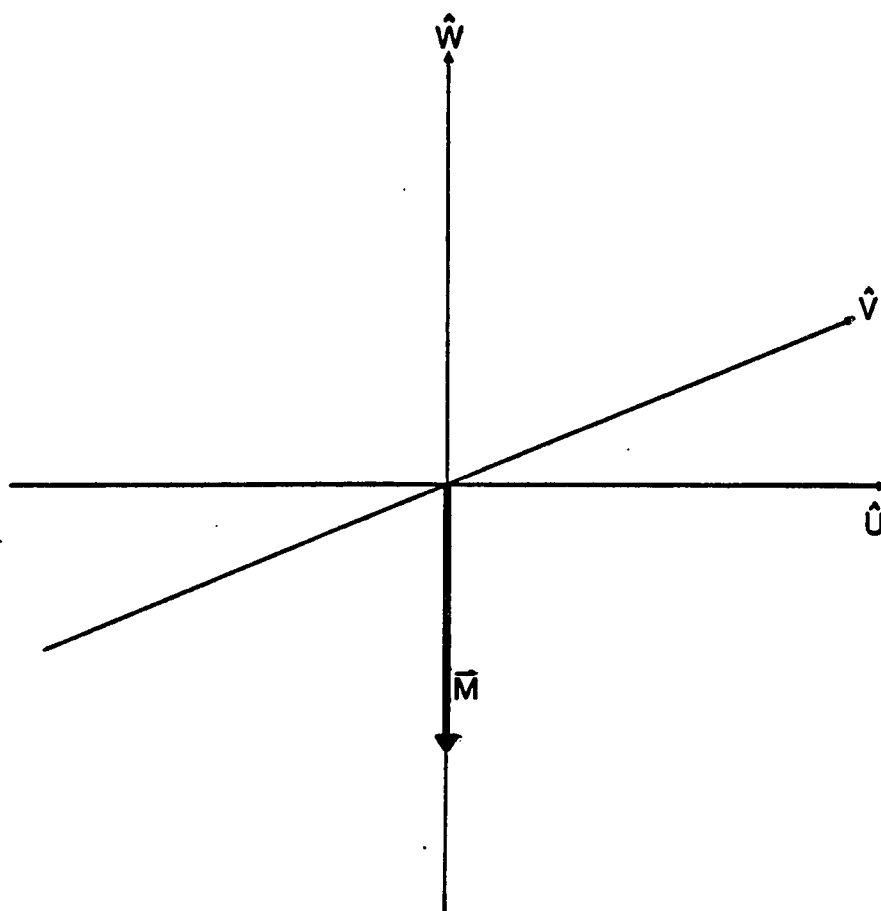


Figure 2.2. The vector representation of a two-level system in low temperature thermal equilibrium.

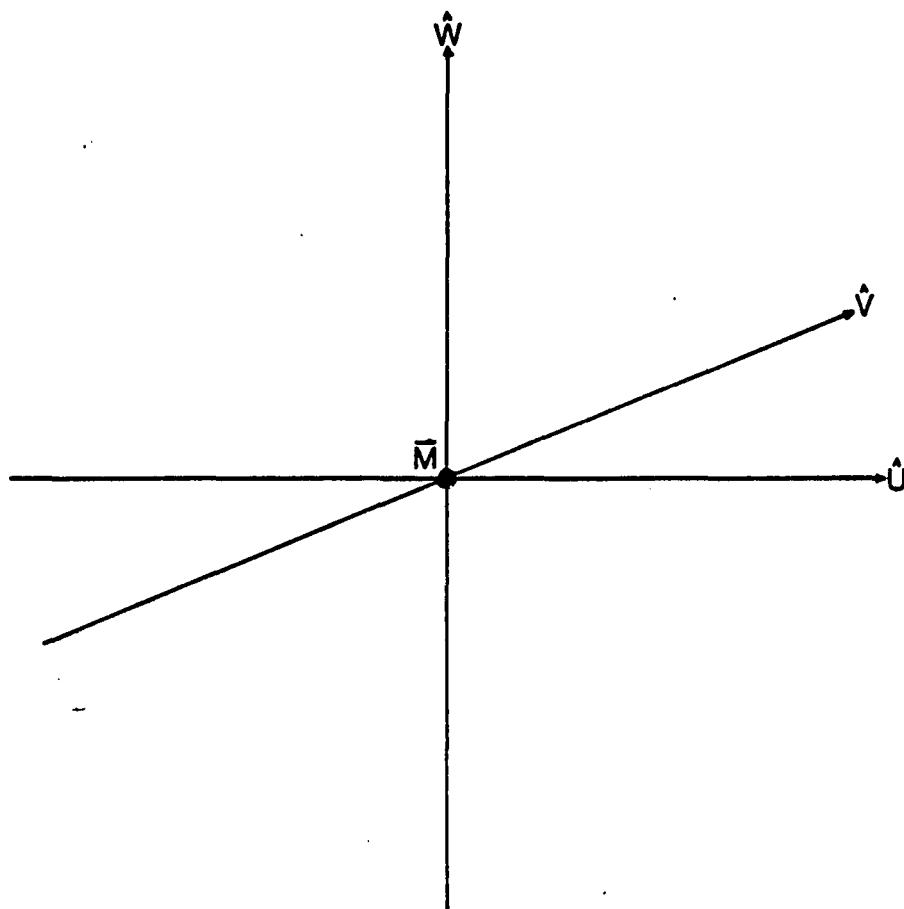


Figure 2.3. The vector representation of a two-level system at 50% inversion.

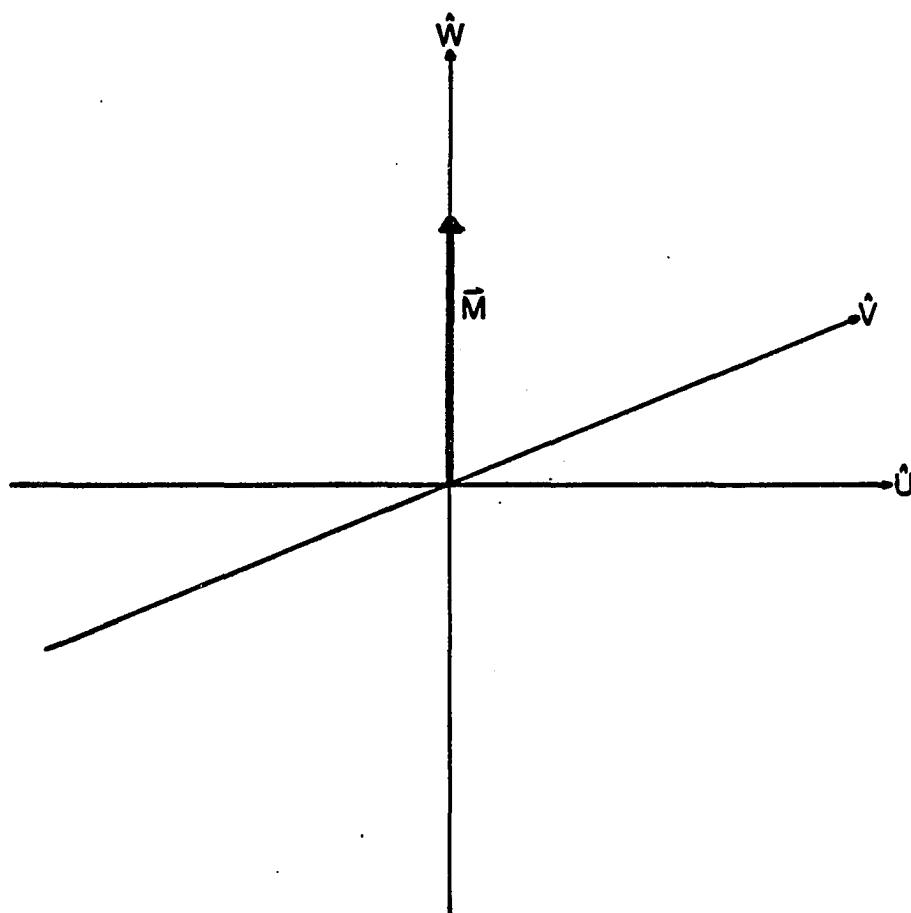


Figure 2.4. The vector representation of a two-level system fully inverted.

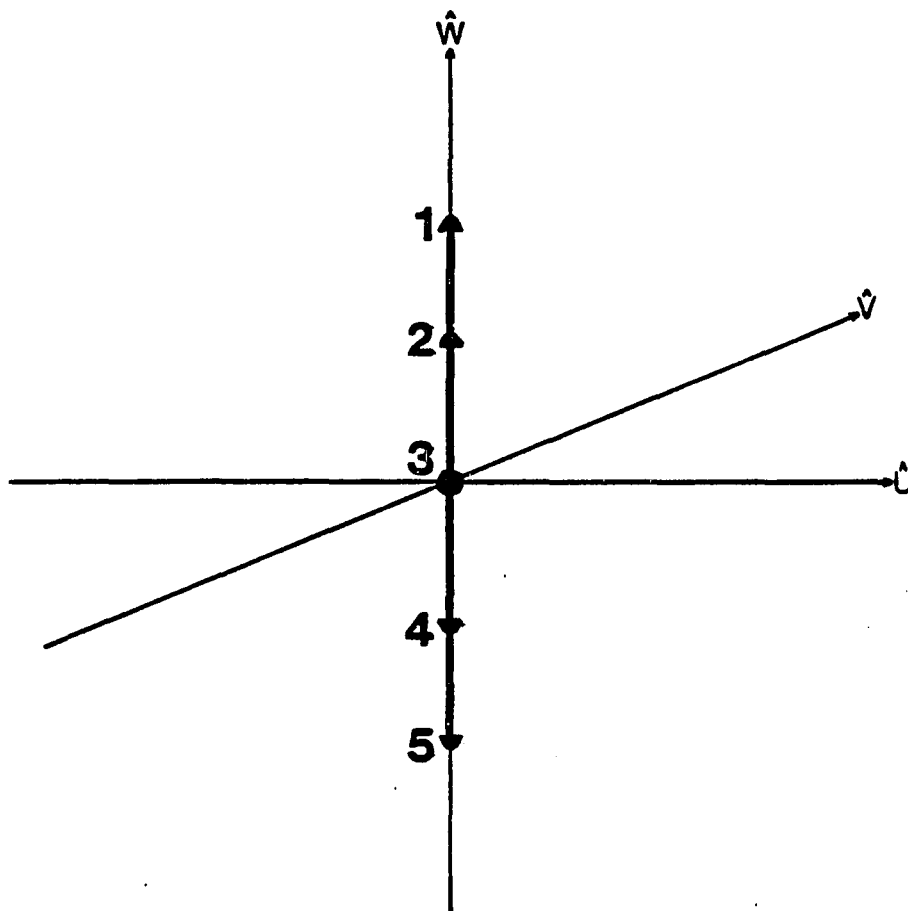


Figure 2.5. The population inversion relaxation of a two-level system using the vector representation.

Equation (2.19) leads to a very insightful vector representation (Feynman et al., 1957) of the coherent interaction which is useful even with strong decay present. To see this we note that equation (2.19) can be written as

$$\frac{d}{dt} \begin{pmatrix} U \\ V \\ W \end{pmatrix} = \begin{pmatrix} U \\ V \\ W \end{pmatrix} \times \begin{pmatrix} \tilde{k}E_0 \\ 0 \\ \delta \end{pmatrix} \equiv \vec{M} \times \vec{F} \quad (2.21)$$

The Vector Representation of the Coherent Optical Interaction

Equation (2.21) is simply the gyroscope precession equation where \vec{M} is the top's angular momentum vector and \vec{F} is the negative of the precessional angular velocity. The driven behavior of a two-level system's dipole and population difference can be easily viewed with a simple 3-space vector construction. Figures 2.2, 2.3, and 2.4 represent two-level systems in "cold" thermal equilibrium, 50% inversion, and fully inverted states. The 50% inversion case represents a system where there is no net induced dipole. The sequence 1-5 in figure 2.5 indicates qualitatively how a fully inverted system's population difference would decay in time. This demonstrates a T_1 decay. Figure 2.6 represents the steady-state excitation of a two-level system detuned from the laser line. This is the steady-state of equation (2.21) as the cross product and the derivative of \vec{M} is zero. Note that the population difference W is not predictable from (2.19). Indeed, by (2.18) we see that we should actually add a relatively small (for large δ) V component. We can understand this phenomenologically as the out-of-phase component to the system's dipole that gives the steady-

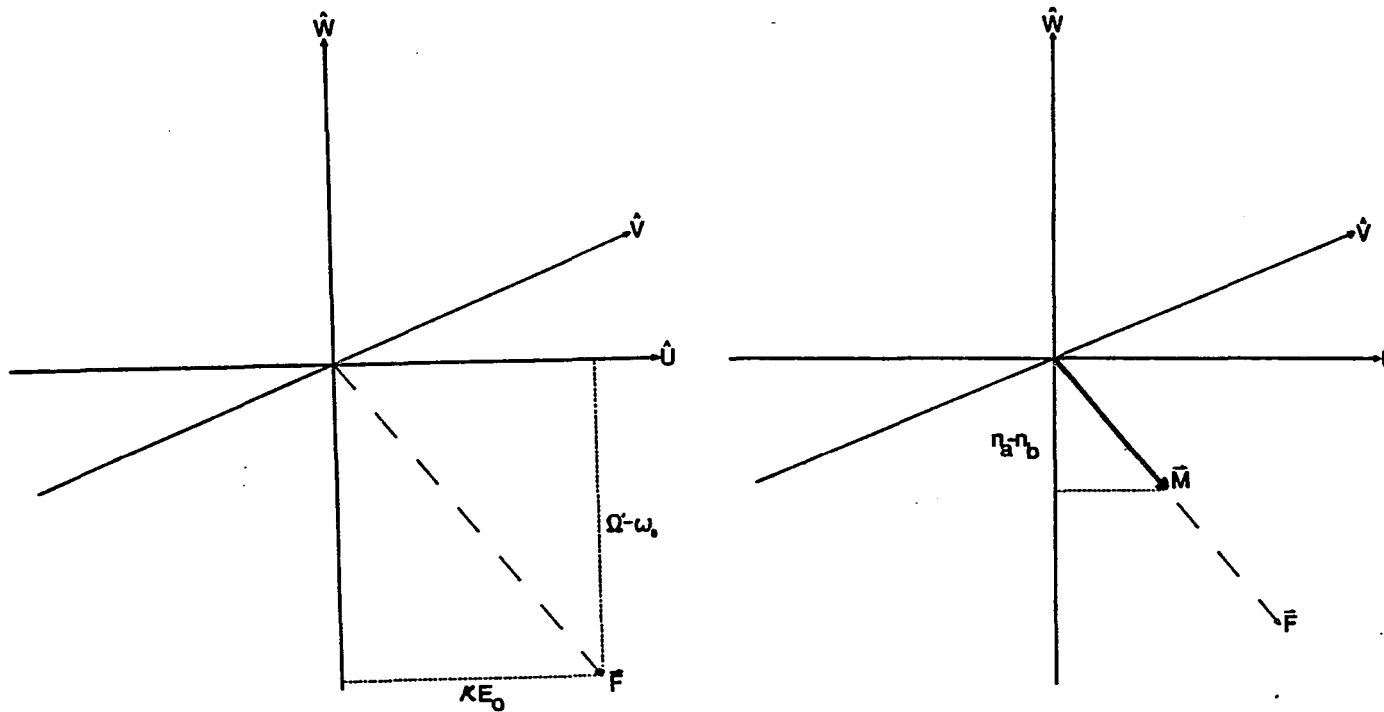


Figure 2.6. The vector representation of a two-level system under non-resonant steady-state excitation a) the pseudo-precession vector's components, b) the \hat{M} vector.

state absorption (figure 2.7). Resonant Rabi flopping is illustrated in figure 2.8. The non-resonant case is given in figure 2.9. We can also qualitatively see what the addition of decay would do to this driven process in figure 2.10. In transient spectroscopy, the observed signal from this driven effect is called optical nutation. If we suddenly turn off the driving field, we see that the system will radiate since the media's dipole remains. In this vector representation the \vec{M} vector, hence, the dipole will rotate about the \hat{w} axis with the frequency δ . This means that in the laboratory frame, the system is radiating at its Doppler-shifted frequency. See figure 2.11. This is the source of free induction decay (FID) radiation. Figure 2.12 illustrates how the FID case would behave with population decay added. If we also add decay processes which disrupt the average dipole but not the population difference, the process would be like figure 2.13 in the case of $\gamma_{ab} \gg \gamma_a, \gamma_b$. Thus, monitoring such FID emissions would give the characteristic decay time of the system's dipole, T_2 , rather than T_1 . The sequences 1-5 in figure 2.14 shows the basic logic behind delayed nutation experiments. A coherent pulse can be used to invert the system. After a delay time in which the system has relaxed to some extent, the coherent radiation is turned on again. The \vec{M} vector will process in the \hat{v} - \hat{w} plane, producing a maximum polarization component (and, thus, signal) in \hat{v} proportional to the magnitude of \vec{M} . By repeating this experiment for different delays, we will know how \vec{M} , which here is just W , relaxes to thermal equilibrium (i.e. we measure

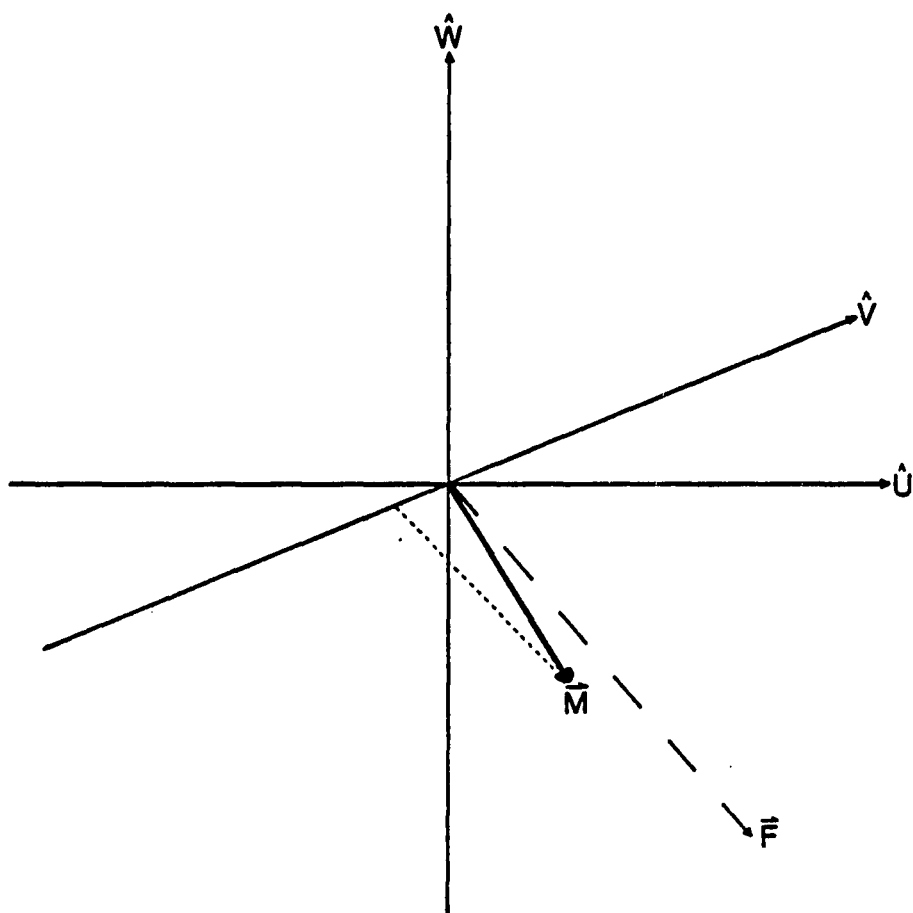


Figure 2.7. Description of the non-resonant steady-state excitation of a two-level system with steady-state absorption included using the vector representation.

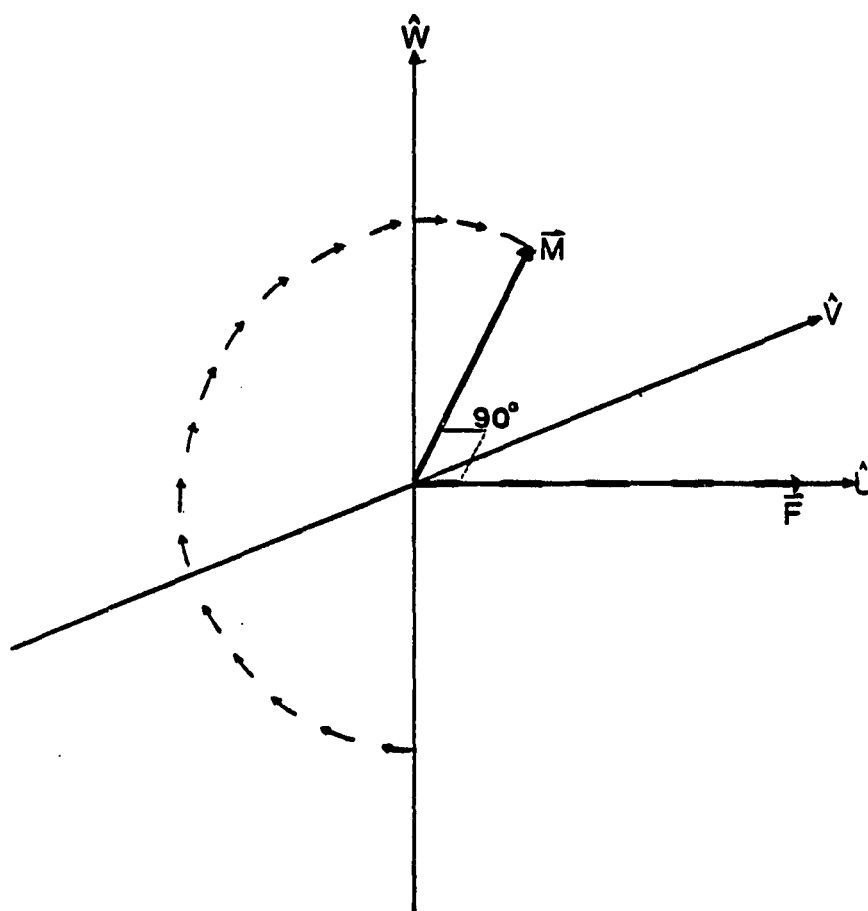


Figure 2.8. The vector representation of the two-level system under resonant Rabi flopping.

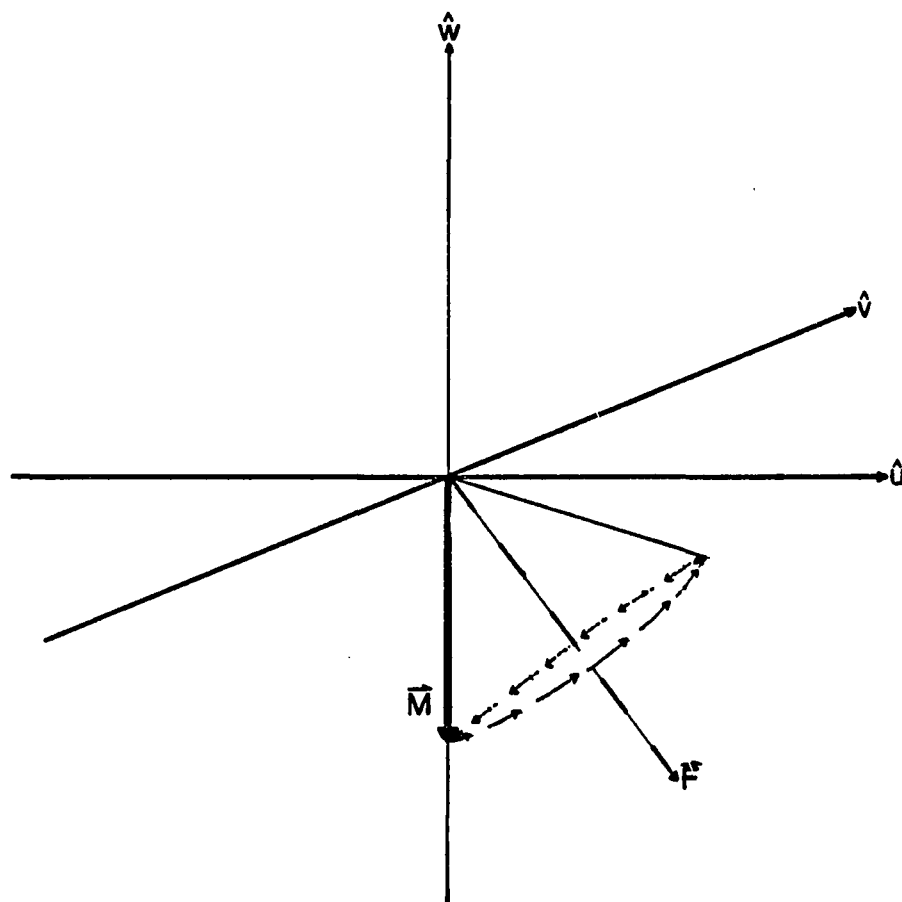


Figure 2.9. The vector representation of the two-level system under non-resonant Rabi flopping.

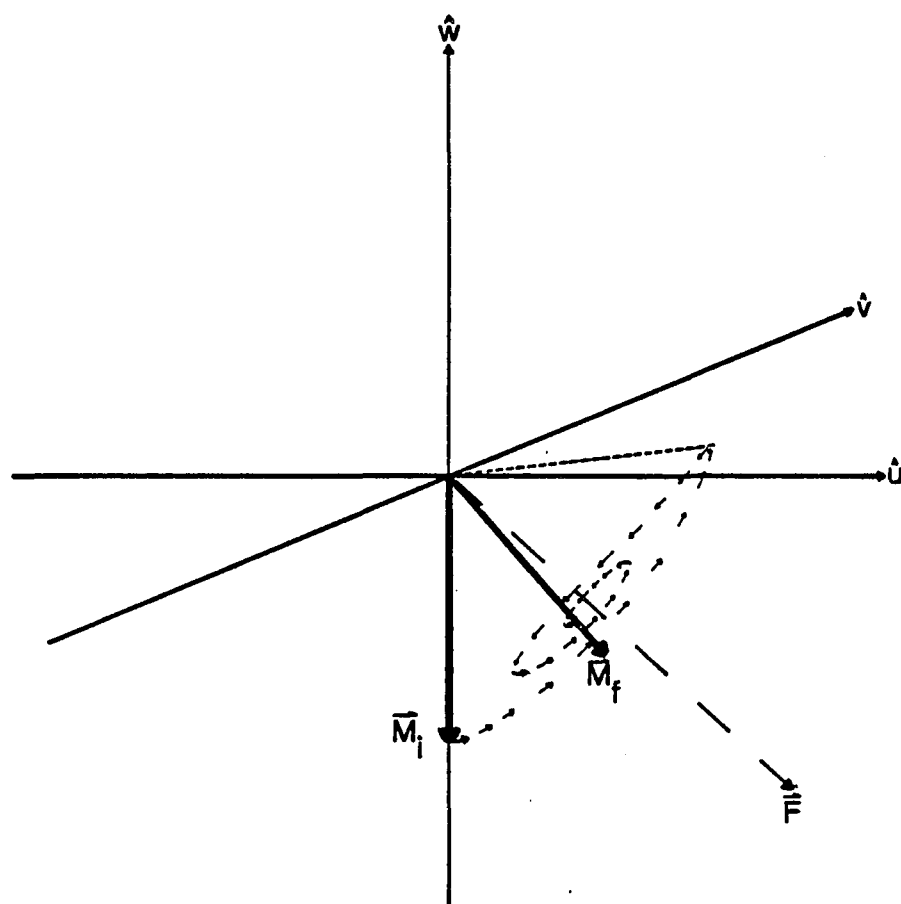


Figure 2.10. The vector representation of the two-level system under non-resonant Rabi flopping with population decay added.

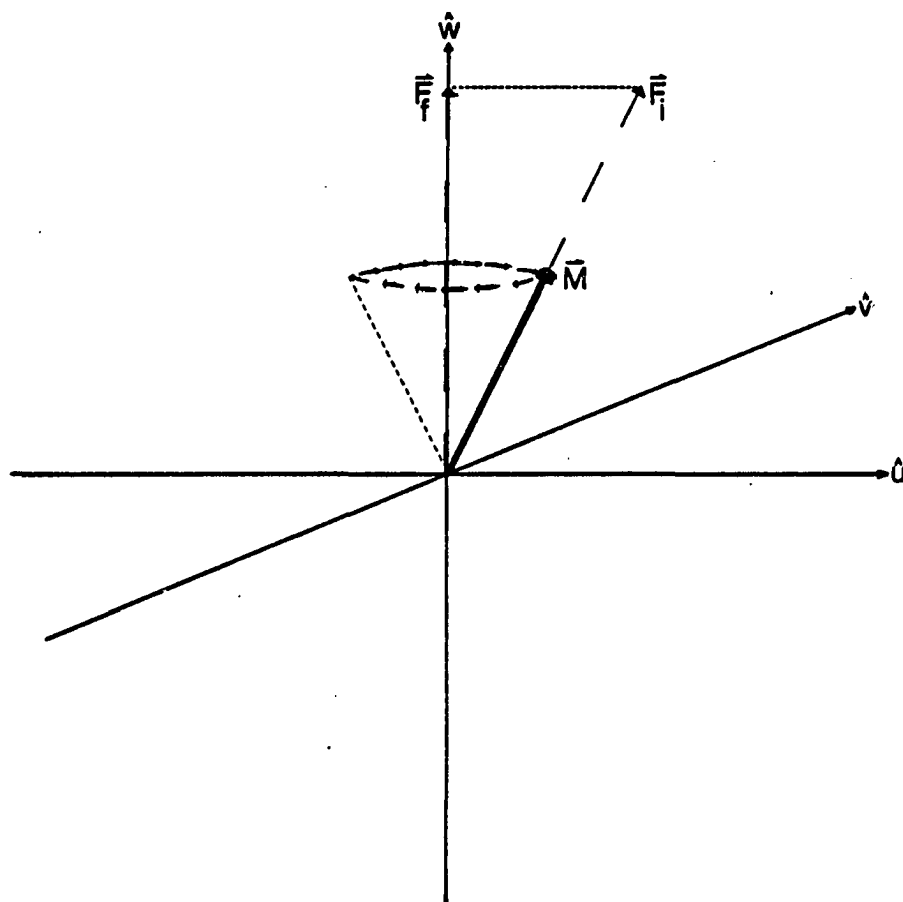


Figure 2.11. The vector representation of the two-level system commencing FID.

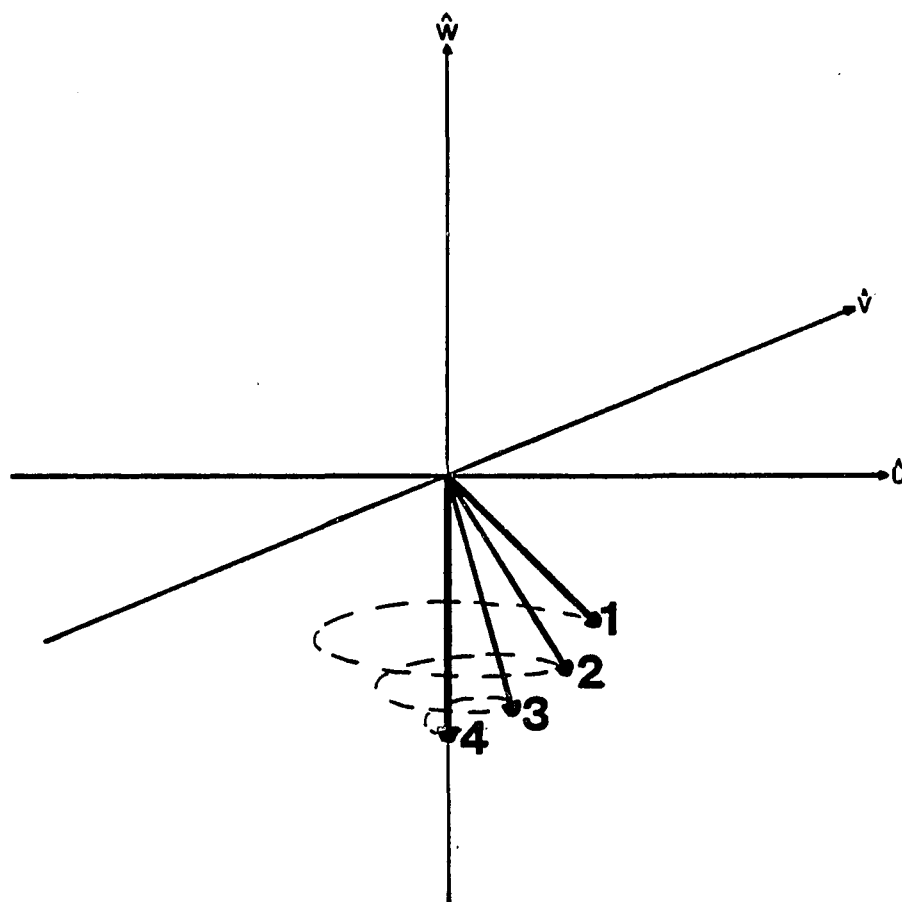


Figure 2.12. The vector representation of the two-level system undergoing FID with population decay.

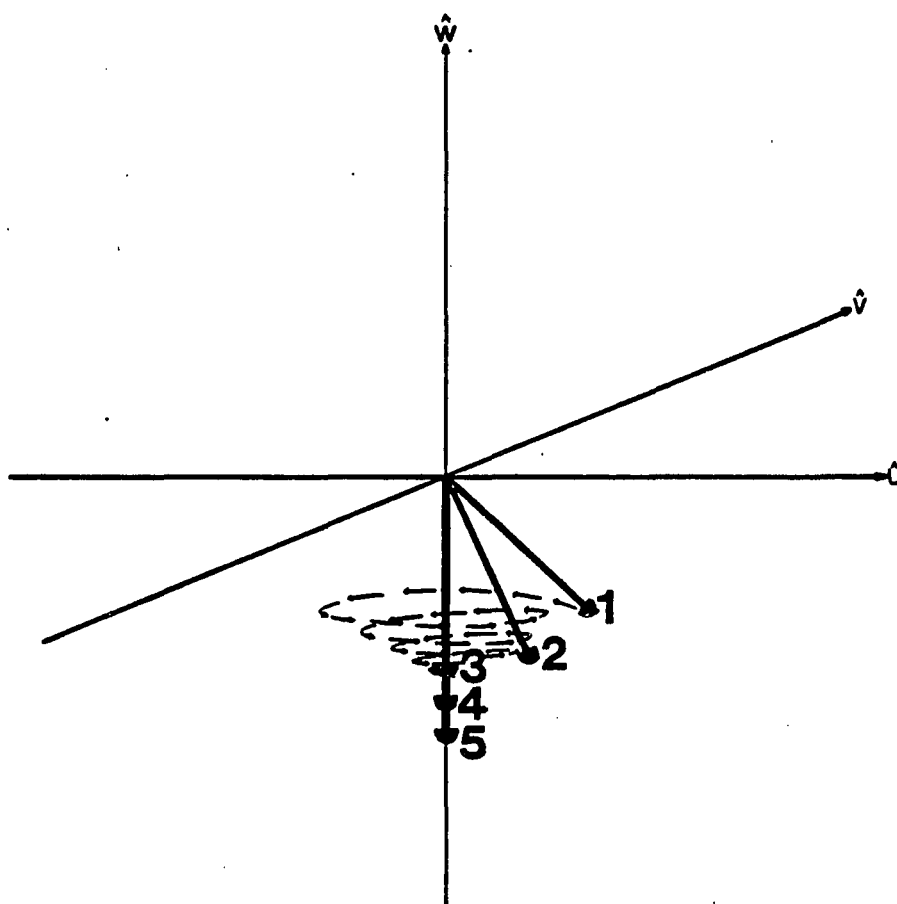


Figure 2.13. The vector representation of the two-level system undergoing FID where $\gamma_{ab} > \gamma_a, \gamma_b$.

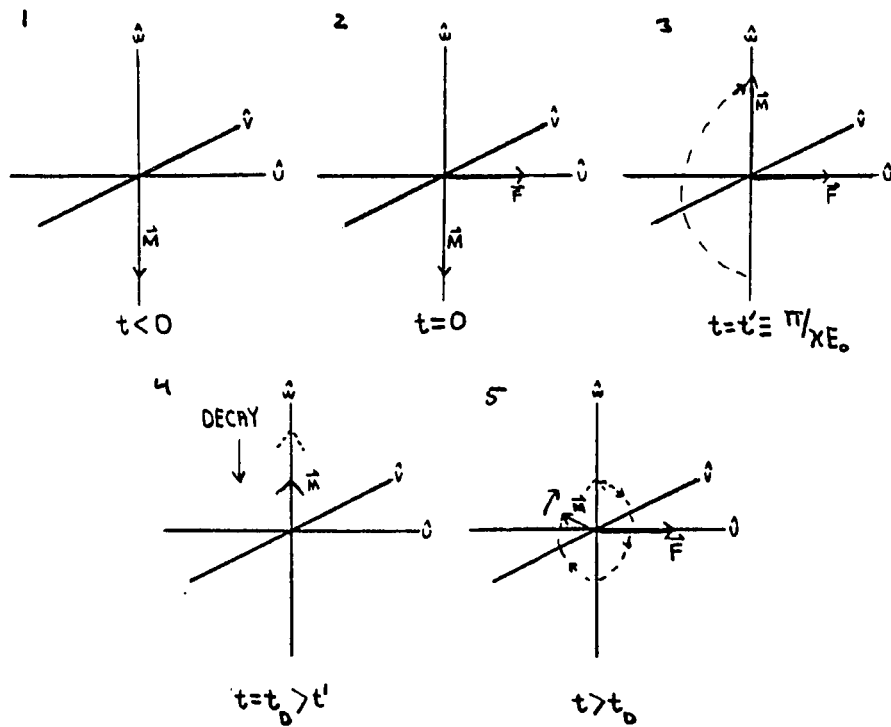


Figure 2.14. The delayed notation experiment illustrated with the vector representation for a two-level system.

1) the system relaxed to thermal equilibrium 2) pulse-one turns on 3) pulse-one turns off 4) system relaxing during delay 5) pulse-two turns on.

So far we have only considered one velocity group or equivalently one frequency detuned group at a time. The transient experiments were done on Doppler broadened media. We must consider the response of many velocity groups. Now in an interaction many \vec{F} vectors must be considered to take into account the different velocity groups (see figure 2.15). The steady state representation shown in figure 2.6 now becomes more complicated. If for simplicity, we assumed very small steady-state absorption, we would get a figure close to that in figure 2.16. If we suddenly turn off the radiation, each \vec{M} will precess about \hat{w} at its own detuned frequency. A FID signal will be produced with the alignment of the \vec{M} during the early part of the precession (see figure 2.17). As precession continues, the vectors, thus the dipoles, would eventually "diffuse" enough to completely average to zero. This is fundamentally why FID is not used to measure T_2 in infrared molecular transitions. You would essentially only measure the frequency band width of excited molecules.

The velocity dephasing effects can be avoided by using the photon echo effect. A laser pulse, pulse-one, is applied to the gas just long enough to drive the resonant velocity group to the \hat{v} axis (a $\pi/2$ pulse). Just at the trailing edge of the pulse, if we looked down on the \hat{v} - \hat{u} phasor plane, we would see basically figure 2.18. In time the net dipole of the system would decay to zero as in the earlier case. Note that the phasors grouped near the resonant \vec{M} would determine the final end of the net dipole of the gas system by their diffusion. All other \vec{M} would dephase to zero much more rapidly due to their larger detuning. Since this final packet of \vec{M} are spread narrowly in

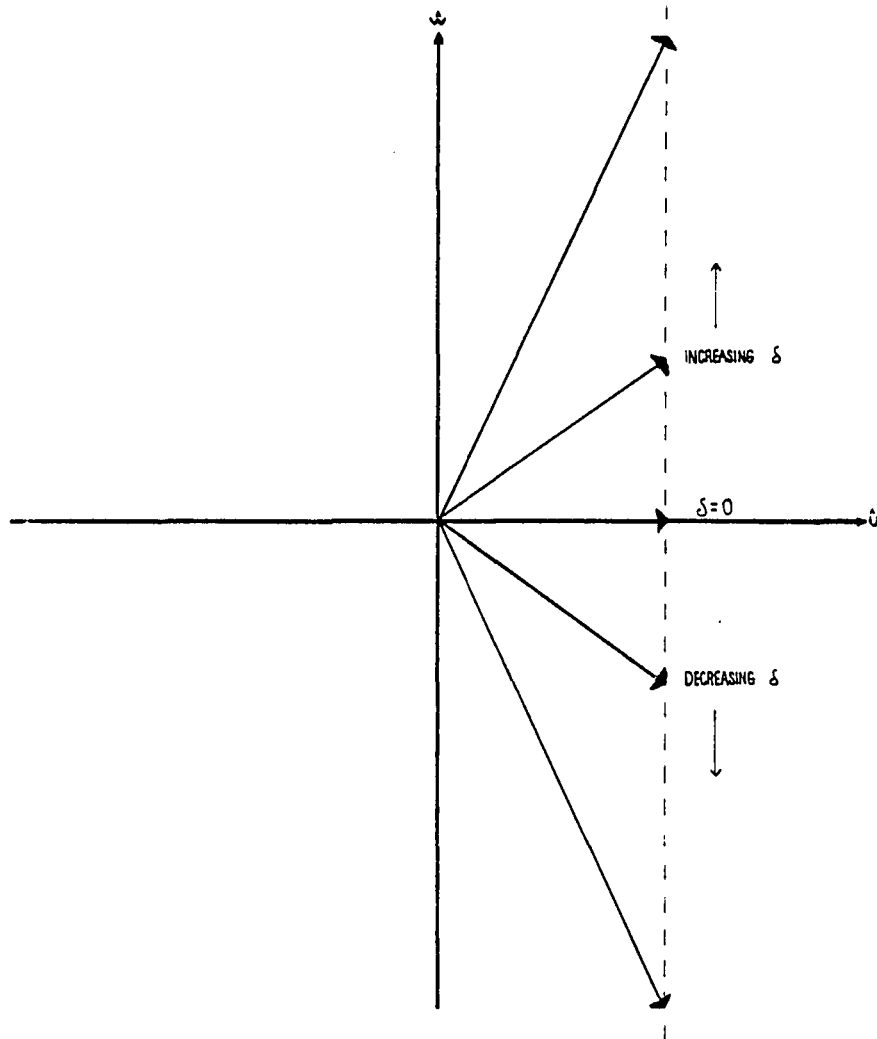


Figure 2.15. The spread in \vec{F} vectors that must be considered due to the spread in contributing velocity groups.

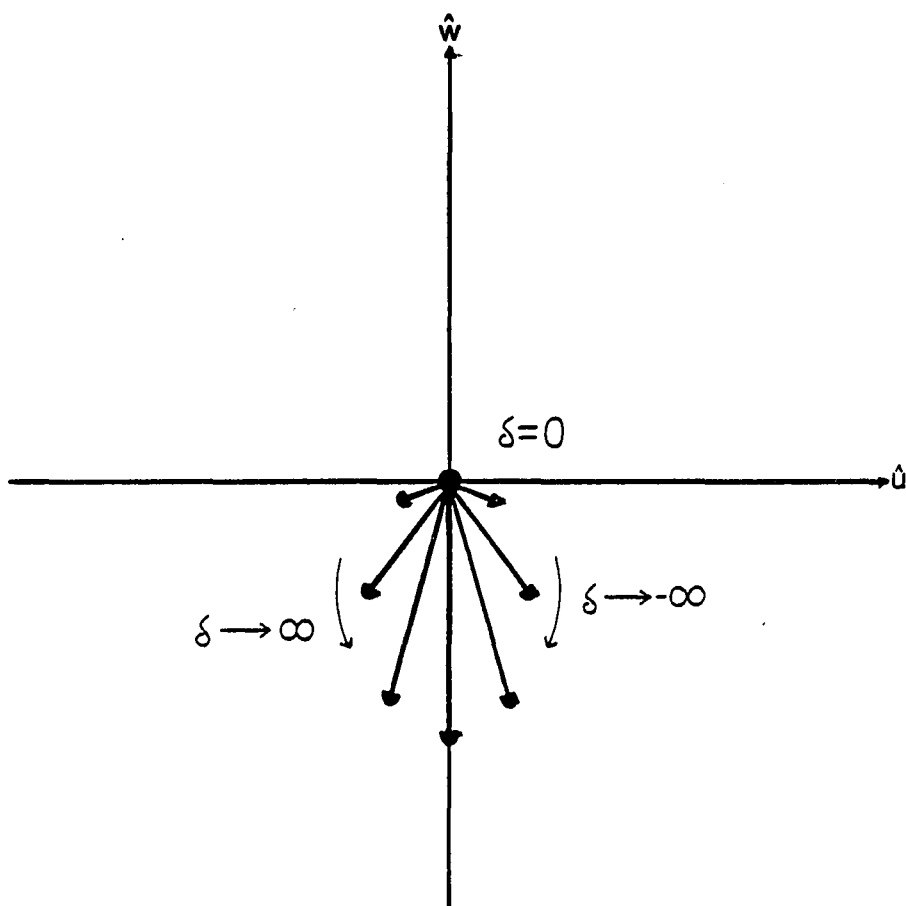


Figure 2.16. The vector representation of Doppler-distributed two-level systems under steady-state excitation (allowing small steady-state absorption).

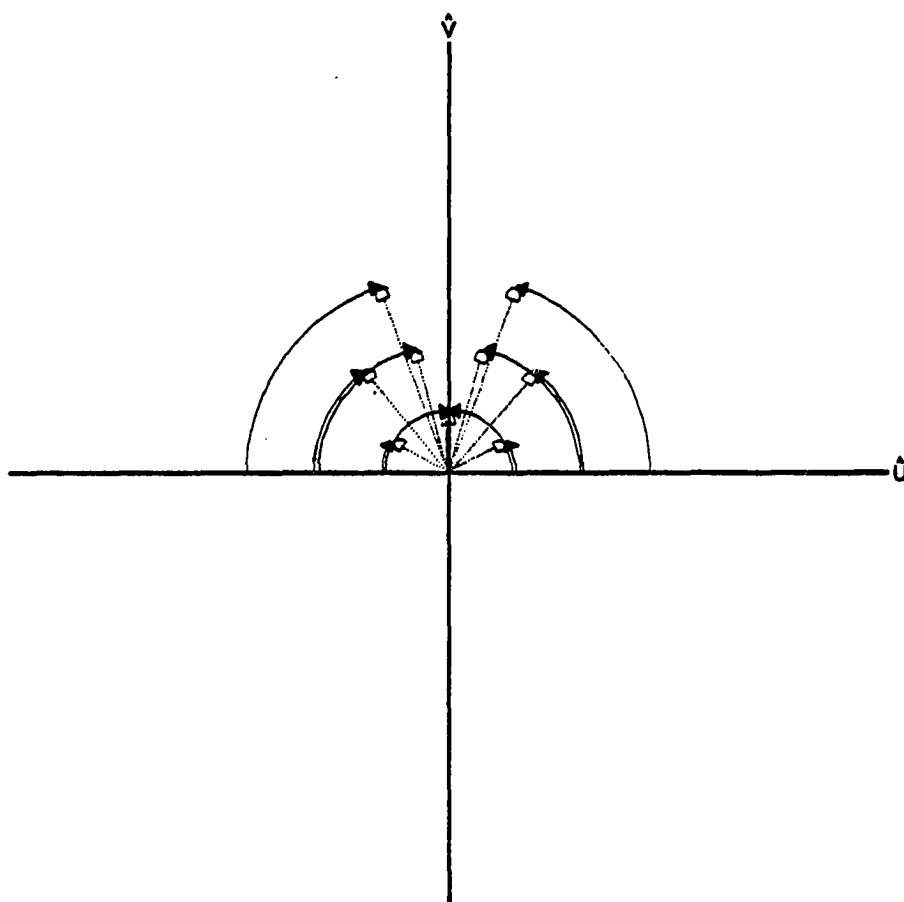


Figure 2.17. The vector representation of Doppler-distributed two-level systems undergoing FID after steady-state excitation.

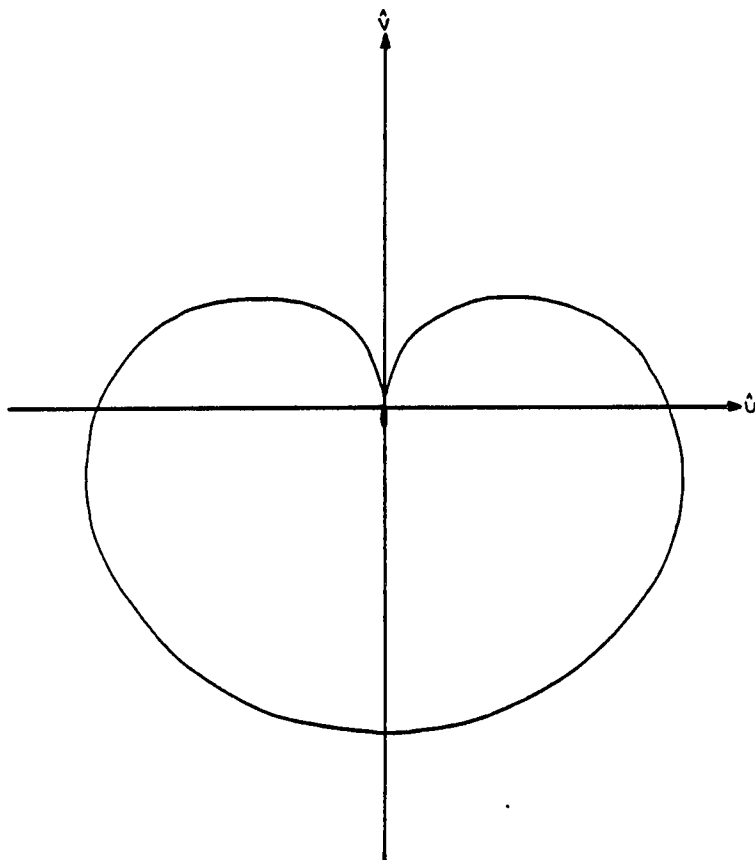


Figure 2.18. The locus of points of the induced dipoles' phasors of a Doppler-distributed two-level gas after a $\pi/2$ pulse.

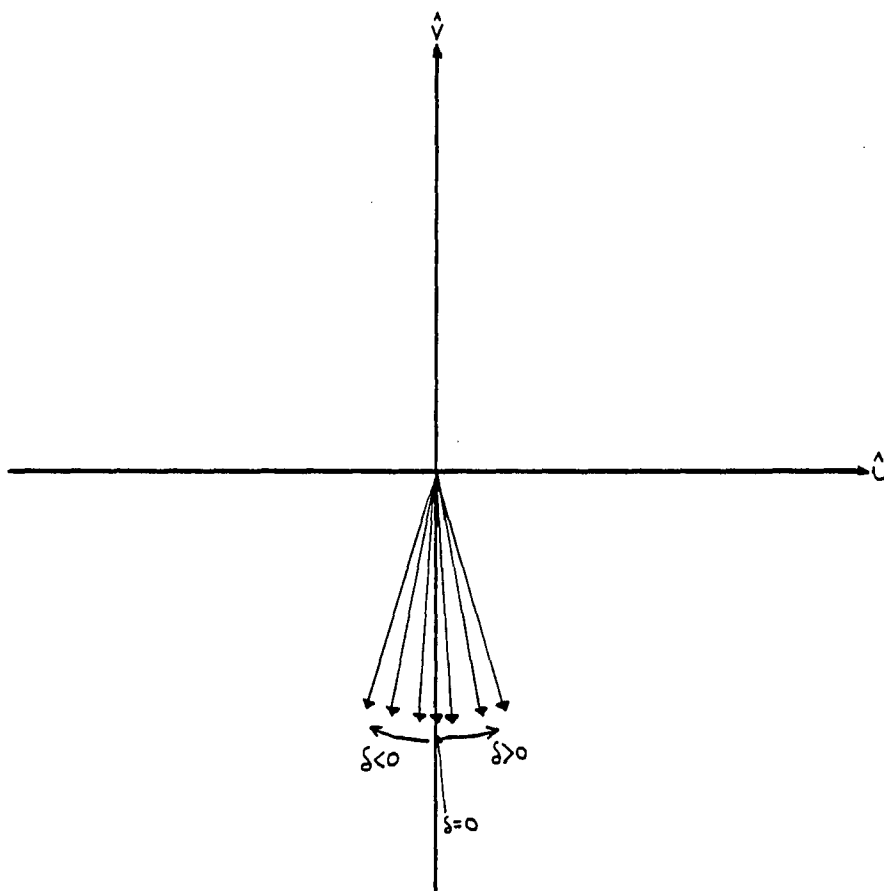


Figure 2.19. The dephasors of the macroscopic induced dipole of a two-level system via the resonant frequency spread.

detuning, we can use the same procession vector \vec{F} in dealing with further interactions. The dephasing of this final packet is shown in figure 2.19. At $t=t'$ assume a π pulse, pulse-two (duration of pulse two = two times the duration of pulse-one and intensities are equal), is applied. Figure 2.20 shows this driven effect. Clearly, in a time t' after the pulse-two, the phasors will once again realign to form a net dipole for the system, and the system will spontaneously emit a burst of coherent light. Any process that would destroy the coherence of a molecule with respect to the other molecules, aside from velocity dephasing, would attenuate this burst. Thus, by doing echo experiments over a range of pulse delays, we can extract the T_2 information denied us in FID signals.

Delayed nutation experiments are not affected by velocity dephasing directly. Such experiments deal with the \hat{w} component of \vec{M}, W . A velocity spread in the media does lessen the net inversion of the absorbers. Except for the exactly resonant velocity group, each velocity group contributing to the nutation will start with a W less than peak inversion. Each of these contributions would decay in the same manner, however. Thus, T_1 could still be extracted from the experiment, while the extent of signal modulation across pulse delay times would be reduced.

An alternative form of initial excitation can be used. Instead of a pulse, a strong but highly detuned laser frequency could be applied and slowly swept (with respect to the flopping frequency) through and well past the medium's resonance. Figure 2.21 shows the sequence in terms of \vec{M} . If this sweep is done in a time short compared

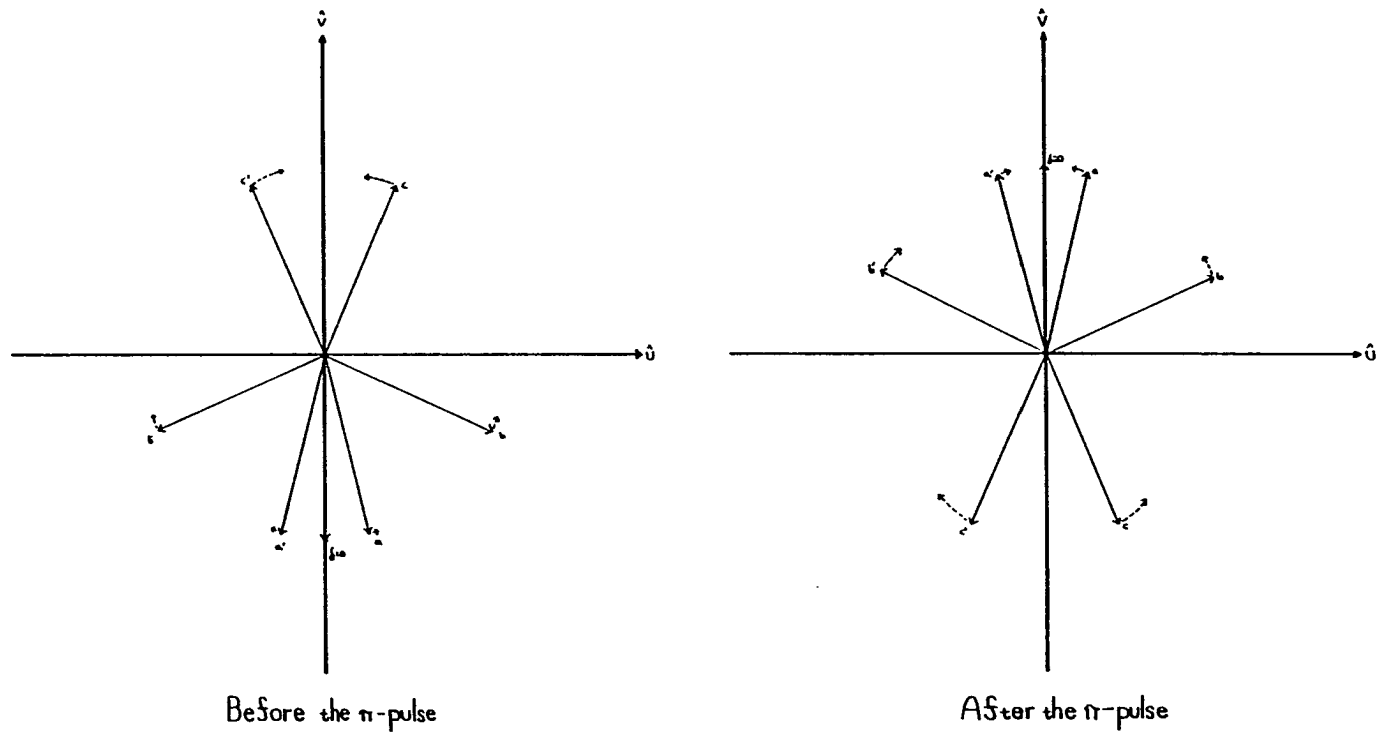


Figure 2.20. The effect of a π pulse on a Doppler-distributed two-level gas originally excited by a $\pi/2$ pulse in the vector representation.

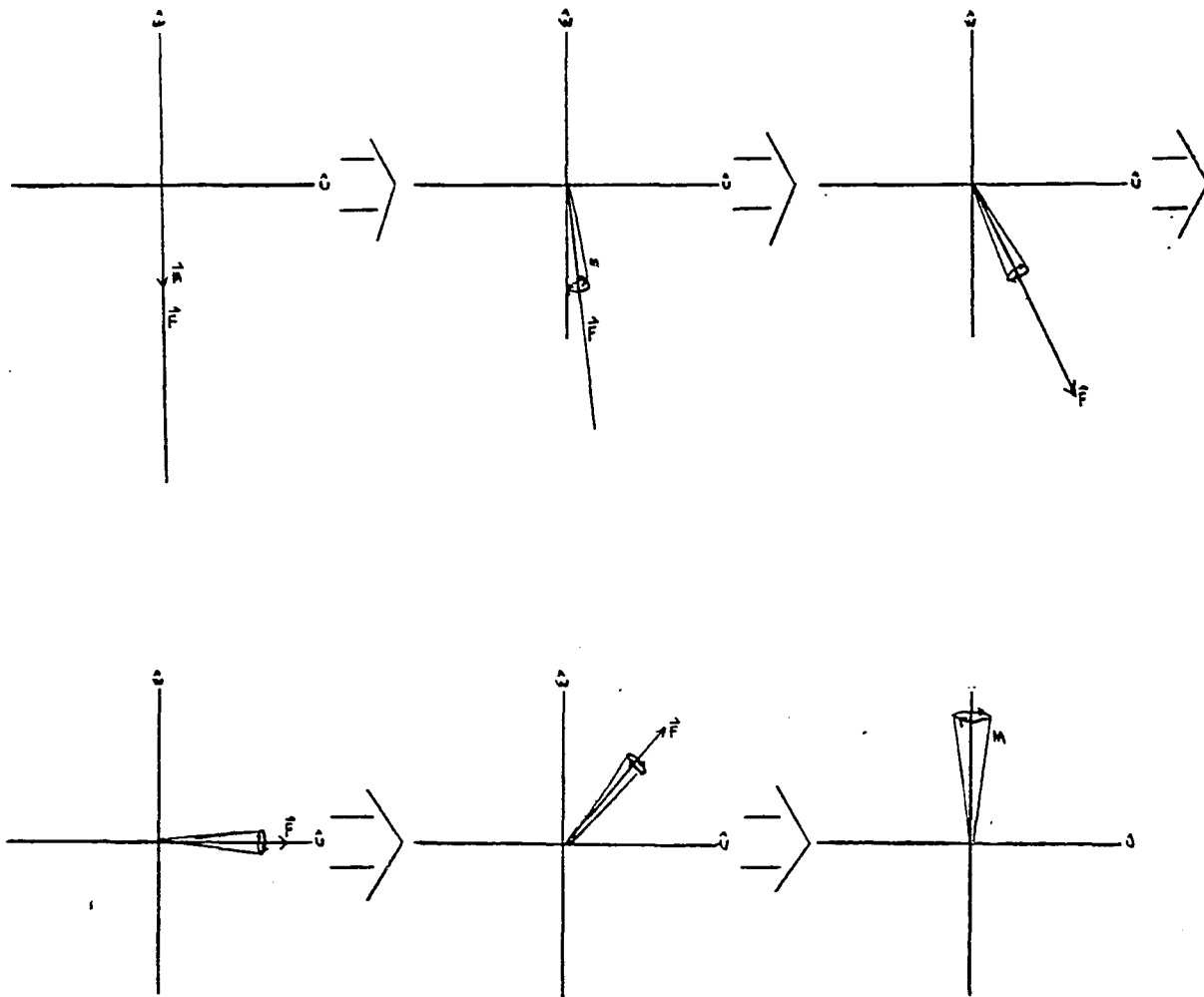


Figure 2.21. An ARP population inversion sweep in the vector representation.

to T_1 , then each velocity group would be inverted. This technique is called adiabatic rapid passage, (ARP).

Extension of Theory of ARP

Now let us leave the vector model and return to the equations of motion. First, we shall apply and extend the above theory to Stark-based ARP excitation. It should be noted that the theoretical development presented so far is applicable to pulsed radiation, Stark tuning of the resonance, and frequency switched experiments. This is so since all the experiments involve interacting and noninteracting phases for the velocity groups of interest. This can be accomplished by turning on or off the radiation, tuning in or out of frequency the velocity group, or tuning in or out of frequency the laser radiation. Further, the dynamical equations are dependent only on the frequency difference of the light and the gas resonance, making the latter two techniques very equivalent.

In the ARP experiments described here, the frequency sweep is linear. Thus, we can apply equations (2.19) to the present ARP case if we assume that δ is a function of time of form

$$\delta \equiv R \cdot t - \delta_0 \quad (2.22)$$

where R and δ_0 are both positive or both negative constants.

Note that regardless of the form of $\delta(t)$, for times short compared to T_1 and T_2 , equations (2.19) tell us that the magnitude of the pseudo-vector \vec{M} is invariant, i.e.

$$\begin{aligned} \frac{d}{dt} |\vec{M}|^2 &\propto \dot{U}U + \dot{V}V + \dot{W}W = U \cdot \delta \cdot V + V(-\delta \cdot U + \tilde{\kappa}E_0W) \\ &+ W(-\tilde{\kappa}E_0 \cdot V) = 0 \end{aligned} \quad (2.23)$$

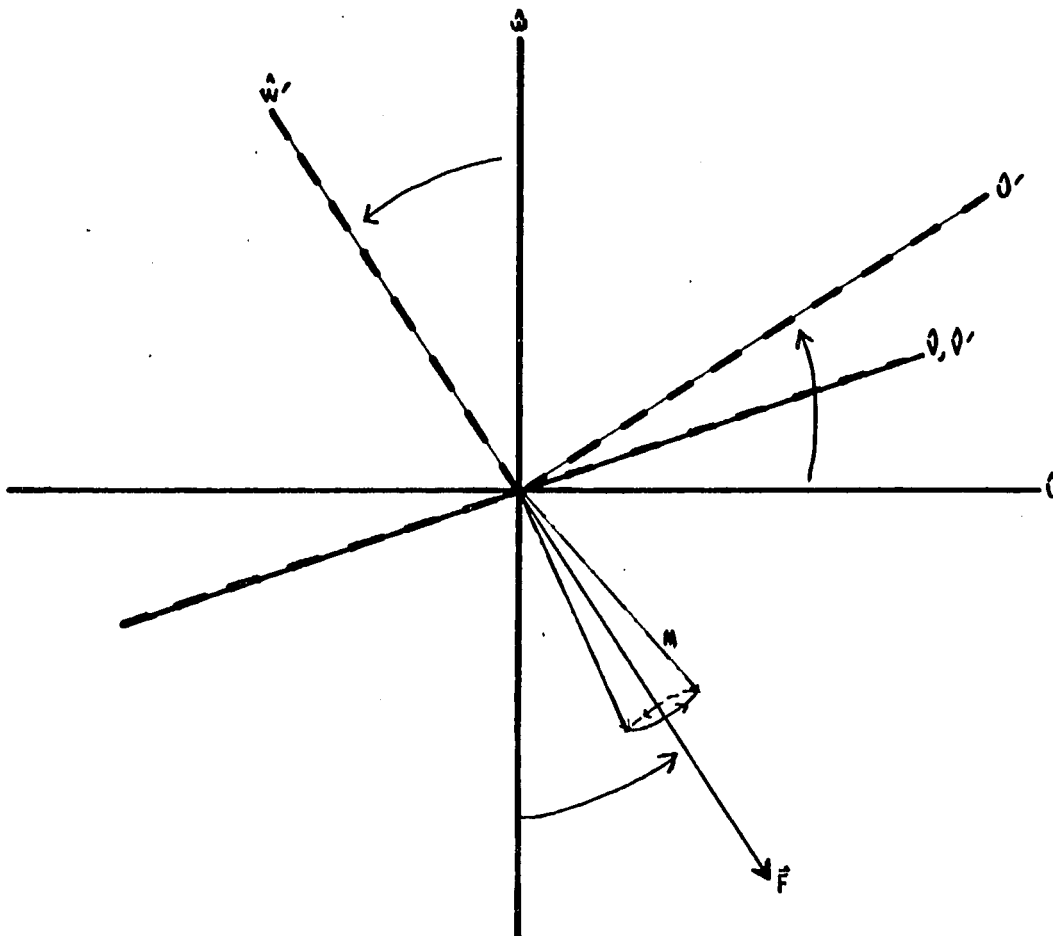


Figure 2.22. The doubly rotating co-ordinate frame ($\hat{U}'\hat{V}'\hat{W}'$) of equation 2.24 with respect to the singly rotating frame ($\hat{U}\hat{V}\hat{W}$) of equation 2.19.

By the simple vector arguments above, we would expect the pseudo-vector \vec{M} to follow the pseudo-precession vector \vec{F} . Thus, it is convenient to perform a transformation from the present rotating co-ordinate frame to one in which the driving precession vector is along \hat{w}' axis (Shoemaker, 1978; Abraham, 1961). The transformation is

$$\begin{pmatrix} U' \\ V' \\ W' \end{pmatrix} = \begin{pmatrix} \cos\theta & 0 & \sin\theta \\ 0 & 1 & 0 \\ -\sin\theta & 0 & \cos\theta \end{pmatrix} \begin{pmatrix} U \\ V \\ W \end{pmatrix}$$

where $\theta \equiv \tan^{-1} \delta(t) / \kappa E_0$. See figure 2.22.

Using equations (2.19), (2.22) and (2.24) we find that

$$\dot{\vec{M}}' \equiv \frac{d}{dt} \begin{pmatrix} U' \\ V' \\ W' \end{pmatrix} = \begin{pmatrix} U' \\ V' \\ W' \end{pmatrix} \times \begin{pmatrix} 0 \\ -R \\ -g(t) \end{pmatrix} = \vec{M}' \times \vec{F}' \quad (2.25)$$

Equation (2.25) also has the form of an equation of motion of a processing top. If we consider velocity groups at the center of the frequency sweep range of the experiment, at the start of the experiment, they would be non-interacting and unexcited. That is, both \vec{M}' and \vec{F}' would be along \hat{w}' . As the laser tunes close to resonance, the \vec{F}' vector would move out of alignment with \hat{w}' allowing \vec{M}' to now precess about \vec{F}' . Assuming that the ARP sweep goes well beyond resonance, such that \vec{F}' finally stops, once again collinear with \hat{w}' , we can find using equation (2.25), a lower limit to the extent of inversion and a necessary condition for inversion. This is illustrated in figure 2.23 which shows the worst case where throughout the ARP sweep, the \vec{M}' vector precesses at the maximum possible angle. This is the minimum inversion case by equation (2.25). Noting that

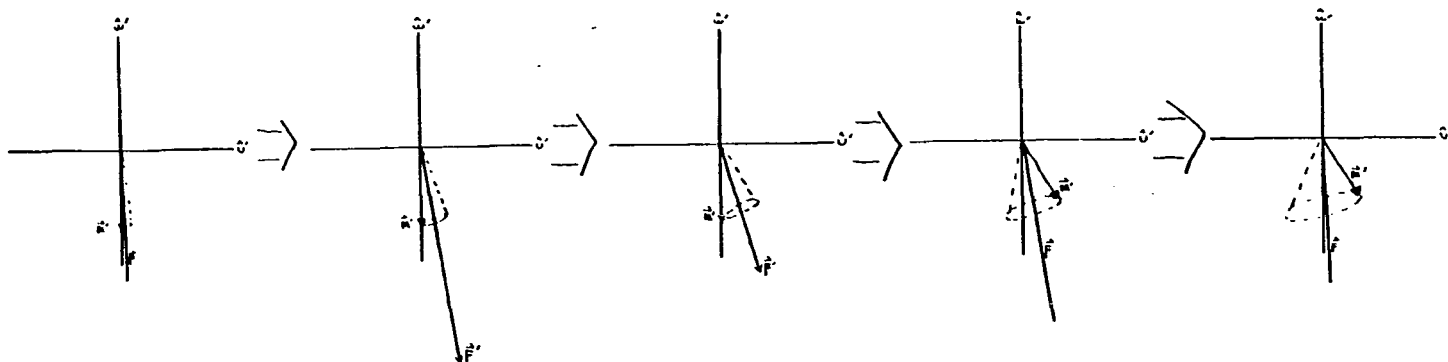


Figure 2.23. An ARP population inversion sweep in the doubly rotating frame vector representation and assuming the \vec{M}' to \vec{F}' angle to be always maximized (worst case).

$$\theta = R\tilde{\kappa}E_0 / ((\tilde{\kappa}E_0)^2 + \delta^2) \quad (2.26)$$

we find that

$$\alpha \leq \tan^{-1} R / (\tilde{\kappa}E_0)^2 \quad (2.27)$$

where α is the angle between \vec{M}' and \hat{w}' at the end of the sweep. To have an inversion we require α to be small. This gives us a major requirement for ARP inversion:

$$R \ll (\tilde{\kappa}E_0)^2 \quad (2.28)$$

The asymptotic behavior for the \hat{w} component of \vec{M} under a linear sweep for a two-level system with no decay has been solved using the probability amplitude formalism (Horwitz, 1975). It was found, assuming that the system started in an unexcited state, that

$$W \equiv \vec{M} \cdot \hat{w} = -|\vec{M}| [2\exp(\frac{-\pi}{4}(\tilde{\kappa}E_0)^2/R) - 1] \quad (2.29)$$

So far, decay effects during the ARP sweep have been ignored. In the ARP experiments the duration of the laser frequency within $5\kappa E_0$ of the velocity groups of interest can become significant, though still well less than the decay times and the applied delay times. It is only within this frequency interval that interaction between the radiation and the velocity groups of interest can occur. Theoretical work has been done on ARP excitation using the two-level atom and assuming the upper and lower level populations decay at the same rate (Lehmberg, 1975). Though we can not assume this, we are not interested in the details and can still take their work as a guide to the limits of ARP theory when decay is present. It was found that the ARP processes still were in

effect as long as the diagonal and off-diagonal molecular decay rates were much less than the Rabi flopping frequency, $g(t)$. In Lehberg's work it was found that if the above condition was met that the \vec{M} vector would point in the same direction as the decayless case but would have a magnitude less than the decayless case. Very roughly, the decay of the magnitude would go as the decay of an excited state \vec{M} in the absence of the fields.

This decay condition is easily met in the present ARP experiments. Hence, the above decayless considerations are still in affect. The extent of the inversion will be somewhat less than that expected in equation (2.29) but for the decay and delay times that we are working with, the decay during excitation will not dominate the process.

It is this avoidance of decay effects during the sweep which adds the term "rapid" to the title of ARP. The condition for ideal ARP is

$$R \gg 10\kappa E_0 \gamma; \quad \gamma = \gamma_a, \gamma_b, \gamma_{ab} \quad (2.30)$$

Two-Pulsed Delayed Nutation

Let us now consider more carefully the two-pulse delayed nutation experiment, using equations (2.20) and (2.17). We assume that initially the system is in the state $\vec{M} = (0, 0, n_a - n_b)$. We apply a π -pulse (duration of $\pi/\kappa E_0$) via equation (2.20), allow the system to relax for a time t' via equation (2.17), and then reapply the laser radiation, using equation (2.20) again. Considering the system's behavior for a short time we find

$$\begin{aligned}
V(t) = & (n_a - n_b) \left\{ -\frac{\delta}{g} \sin(g(t-t')) \left[\frac{\delta \tilde{\kappa} E_0}{g^2} (1 - \cos(g \frac{\pi}{\tilde{\kappa} E_0})) \sin(\delta t') \right. \right. \\
& + \frac{\tilde{\kappa} E_0}{g} \sin(g \frac{\pi}{\tilde{\kappa} E_0}) \cos(\delta t') \left. \right] e^{-\gamma_{ab} t'} \\
& + \cos(g(t-t')) \left[\frac{\delta \tilde{\kappa} E_0}{g^2} (1 - \cos(g \frac{\pi}{\tilde{\kappa} E_0})) \cos(\delta t') - \frac{\tilde{\kappa} E_0}{g} \sin(g \frac{\pi}{\tilde{\kappa} E_0}) \sin(\delta t') \right] e^{-\gamma_{ab} t'} \\
& + \frac{\kappa E_0}{g} \sin(g(t-t')) \left[1 - \left(\frac{\tilde{\kappa} E_0}{g} \right)^2 (1 - \cos(g \frac{\pi}{\tilde{\kappa} E_0})) \left(\frac{e^{-\gamma_a t'} + e^{-\gamma_b t'}}{2} \right) \right] \left. \right\}. \quad (2.31)
\end{aligned}$$

The U and W solutions need not be considered. The in-phase dipole, U, radiates an out-of-pulse field while the out-of-phase dipole, V, radiates the in-phase field with respect to the driving field. Since the medium is assumed optically thin, and the intensity (E^2) sensitive detector sees both the transient signal and the laser beam, the detected signal goes as

$$\begin{aligned}
\langle ((E_0 + \xi_1 \cdot V_S) \cos(\Omega t) + \xi_2 U_S \sin(\Omega t))^2 \rangle &= \frac{E_0^2}{2} + \frac{(\xi_1 V_S^2 + \xi_2 U_S^2)}{2} \\
&\sim \frac{E_0^2}{2} + \xi_1 V_S E_0 \quad (2.32)
\end{aligned}$$

where ξ_1 and $\xi_2 \ll E_0$. Because we used an AC-coupled detector, the signal detected would be directly proportional to V.

The V_S used in equation (2.32) would not be the expression in equation (2.31) but rather the sum of equation (2.31) over all possible δ . Since the detuning is due to the velocity distribution of the gas, we can write using the Maxwell-Boltzman distribution of velocity

$$(n_a - n_b) = \frac{(N_a - N_b)}{\bar{\delta} \sqrt{\pi}} e^{-(\delta/\bar{\delta})^2} d\delta; \quad \bar{\delta} \equiv \frac{\bar{V}}{c} \quad (2.33)$$

where \bar{v} is the most probable speed of the molecule. Thus, the detector signal, S_d , is of the form

$$S_d \propto \int_{-\infty}^{\infty} e^{-\frac{(\delta-\delta_0)^2}{\delta}} V(t) d\delta \quad (2.34)$$

where $V(t)$ is given by equation (2.31) and δ_0 is the frequency mismatch of the laser from the $v_z = 0$ velocity group. Except for very short times ($t < 1/\delta \approx 10$ ns), the width of the Maxwell distribution is much wider than V in frequency space. This allows us to remove the Gaussian from the integral. Note that all terms in (2.31) which decay as γ_{ab} are odd functions of δ . For times greater than 10 ns these terms would contribute nothing to the integral. Thus, we can write

$$\begin{aligned} S_d &\propto \int_{-\infty}^{\infty} \left(\frac{\sin(g(t-t'))}{g} - \frac{(\tilde{\kappa}E_0)^2}{g^3} (1 - \cos(g\pi/\tilde{\kappa}E_0)) \left(\frac{e^{-\gamma_a t'} + e^{-\gamma_b t'}}{2} \right) \right) d\delta \\ &\propto J_0(\tilde{\kappa}E_0(t-t')) - f(\tilde{\kappa}E_0(t-t')) (e^{-\gamma_a t'} + e^{-\gamma_b t'}) \end{aligned} \quad (2.35)$$

where the first term is the zeroth order Bessel function and the second term is a function which is zero at $t-t'=0$ and peaked at approximately $t-t'=\pi/(2\tilde{\kappa}E_0)$. For typical experimental $\tilde{\kappa}E_0$ values, this second function peaks in a time shorter than the width of the detector's impulse response. Clearly the first function does so also as it peaks even faster than the second. Hence, the first peak in the nutation signal is determined by the detector response. Over the period of the first peak the signal out of the detector, S_0 , can be written as

$$S_0 = (\text{Detector impulse response}) * S \approx F(t) (A + B(e^{-\gamma_a t'} + e^{-\gamma_b t'})) \quad (2.36)$$

where $F(t)$ is a peaked function in the interval and both A and B are constants. If we note the amplitude of the first peak in the nutation for different delays, we will obtain a measurement of the term $(e^{-\gamma_a t'} + e^{-\gamma_b t'})$. Thus, delayed nutation is a measurement of the decay in the non-thermal population difference of the molecules.

Over the period of the first nutation peak, the Bessel function in equation (2.35) will contribute larger values of the convolution than the second term, (see figure 2.24). This shows why we do not see two-pulse nutation signals which are emissive.

Delayed Nutation Using ARP System Preparation

Let us now consider the delayed nutation signal obtained from an initial preparation via ARP. Assume that a portion of the gas's velocity distribution is inverted by a frequency-swept radiation pulse. At a later time a fixed frequency pulse is applied in the manner of the second pulse in two-pulse delayed nutation. If the ARP sweep is wide enough and we probe the velocity groups at the center of the frequency region swept, the system preparation from all the velocity groups contributing to the nutation signal can be described by $\vec{M} = (0, 0, n_b - n_a)$. If we now apply equation (2.17) for a delay time t_s and then apply equation (2.20) for the fixed frequency driving pulse, we obtain

$$V(t) = \left(\frac{\tilde{\kappa} E_0}{g}\right) \sin(g(t-t_s)) (n_a - n_b) (1 - (e^{-\gamma_a t_s} + e^{-\gamma_b t_s})) \quad (2.37)$$

for each velocity group contribution. If we sum all the contributions, we obtain

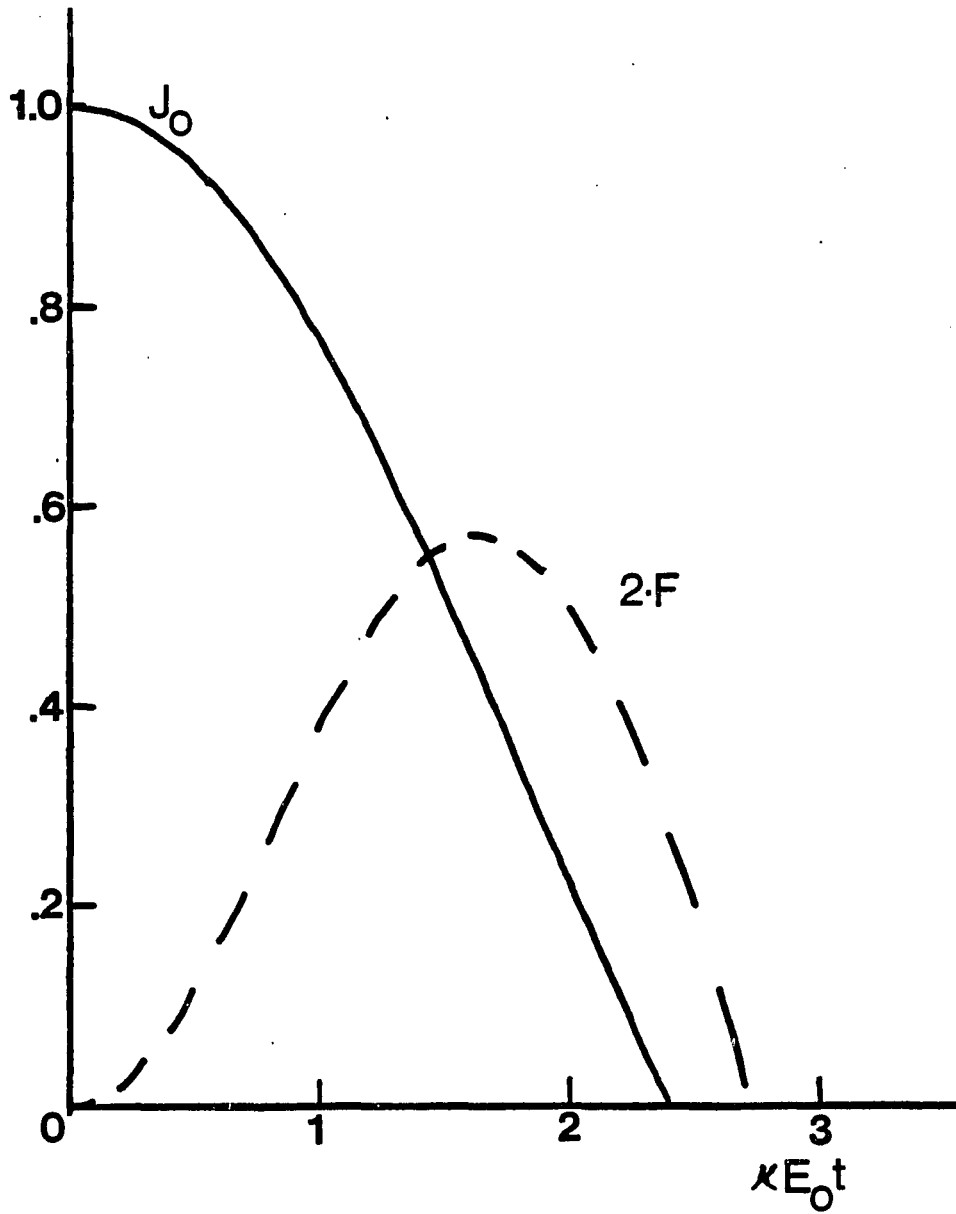


Figure 2.24. The two functional terms S_0 and $2F$ versus $\kappa E_0 t$ from Eq. 2.35.

$$S_d \propto J_0(\kappa E_0(t-t_s)) [1 - (e^{-\gamma_a t_s} + e^{-\gamma_b t_s})] \quad (2.38)$$

Comparing this result to equation (2.35), we see that with ARP excitation, we obtain a signal variation of about twice that possible with pulsed excitation. A net emissive signal is possible. Also there is a certain simplicity in understanding the final signal since the detector band width does not enter so critically into the result.

The Beam Profile Effects on Nutation

It should be pointed out that the actual signal in all experiments is also an average over κE_0 values. This is due to the finite detector size and the fact that the laser beam has a Gaussian profile. In the pulsed excitation case this means pulse-one will not be a π -pulse for all contributing molecules. This will further reduce the modulation of the signal in the two-pulse experiment. In the ARP excitation case, this need not be the case as long as the intercepted beam intensities are all above a certain value determined by the adiabatic conditions. If not, then even in ARP excitation there will be some loss of signal modulation range.

FID Effects in Nutation Studies

In both frequency-switched and the Stark based delayed nutation experiments, there is another possible contribution to the detector signal. In all such experiments done in our laboratory, we never detune entirely out of the molecules' Doppler distribution. During the second pulse, while we are monitoring the nutation from one set of velocity groups, another set of velocity groups are emitting

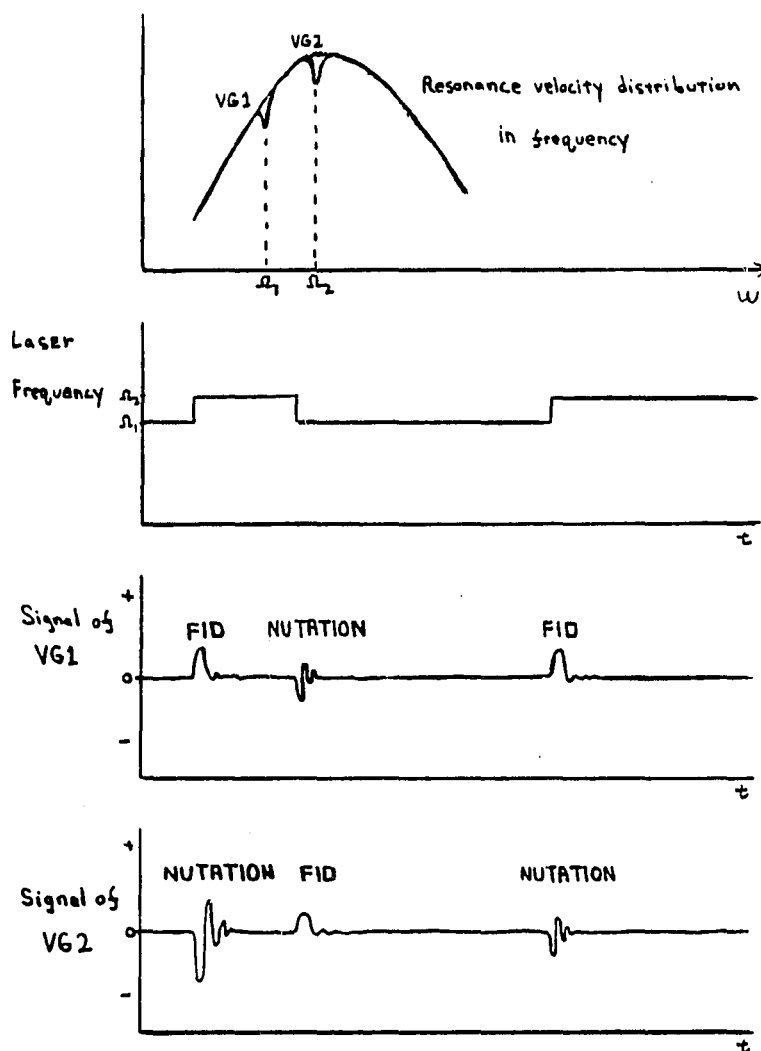


Figure 2.25. The two-pulse delayed nutation sequence experiment via frequency-switching or Stark-switching.

The upper diagram indicates the interacting velocity groups (V.G.1 and V.G.2) with respect to the velocity distribution. The next diagram indicates the applied pulse sequence which can be due to Stark tuning the resonance or frequency-switching. The last two drawings indicate the contribution to the detector signal from each of the velocity groups.

FID signals (see figure 2.25). In the Stark based ARP experiments, the optical frequency difference between the FID signal and the laser are greater than the bandwidth of the detector. With no heterodyne detection, FID could not contribute any significant signal. In the frequency-switched experiments, the frequency differences were about 5 MHz. This is well within the detector bandwidth. It should be noted that FID would contribute a fast oscillatory term to the signal due to its heterodyne detection. This oscillation, and hence the FID contribution, would be filtered out in the fitting of the data to the much more slowly varying equation (2.36). In the frequency-switched experiments done here, this oscillatory contribution was not noticeable in the raw data plots, implying a negligible contribution.

Photon Echo

Finally, let us consider the analysis of photon echoes. For a system in thermal equilibrium, $\vec{M} = (0, 0, n_a - n_b)$. To this system we apply a $\pi/2$ pulse (a pulse of duration $t = \pi / (2\tilde{\kappa}E_0)$). The end result would be obtained by equation (2.20). We then let the system relax for a time t' , the result is given by using equation (2.17). At this point we can apply a π -pulse using equation (2.20) again. We then can write with equation (2.17) the state of the system for any arbitrary time t , after the last pulse. The resulting expressions for U and V contain many terms. Only some of the terms are important, however. We can throw out any terms which are odd functions of δ in the sum of such terms over all possible δ will be zero. We also throw out terms that

obviously can't contribute to the echo mathematically. For example, the term $\sin(\delta t')\sin(\delta t)(1-\cos(g\pi/\kappa E_0))$ would be retained as it can be rewritten to contain the term $1/2\cos(\delta(t-t'))(1\cos(\pi/2E_0))$ which is clearly resonant in t at t' over integration in δ . The term $\sin(\delta t)(1-\cos(\pi/\kappa E_0))(1-\cos(\pi/2\kappa E_0))$ would be dropped as it clearly could not give similar resonant terms. Doing all this we find that

$$\begin{aligned}
U = e^{\gamma_{ab}(t+t')} & \left[\frac{\delta}{g} \sin\left(\frac{g\pi}{\kappa E_0}\right) \left(\frac{\delta\kappa E_0}{g^2}\right) (1-\cos\left(\frac{g\pi}{2\kappa E_0}\right)) \sin(\delta t)\sin(\delta t') \right. \\
& + \frac{\delta}{g} \sin\left(\frac{g\pi}{\kappa E_0}\right) \left(\frac{\kappa E_0}{g}\right) \sin\left(\frac{g\pi}{2\kappa E_0}\right) \sin(\delta t)\cos(\delta t') \\
& + \left(\cos\left(\frac{g\pi}{\kappa E_0}\right)\right) \left(\frac{\delta\kappa E_0}{g^2}\right) (1-\cos\left(\frac{g\pi}{2\kappa E_0}\right)) \cos(\delta t)\sin(\delta t') \\
& \left. + \cos\left(\frac{g\pi}{\kappa E_0}\right) \left(\frac{\kappa E_0}{g}\right) \sin\left(\frac{g\pi}{2\kappa E_0}\right) \cos(\delta t)\cos(\delta t') \right] \quad (2.39)
\end{aligned}$$

$$\begin{aligned}
V = e^{-\gamma_{ab}(t+t')} & \left[\left(1 - \frac{\delta^2}{g^2}\right) (1-\cos\left(\frac{g\pi}{\kappa E_0}\right)) \left(\frac{\delta\kappa E_0}{g^2}\right) (1-\cos\left(\frac{g\pi}{2\kappa E_0}\right)) \sin(\delta t)\cos(\delta t) \right. \\
& + \left(1 - \frac{\delta^2}{g^2}\right) (1-\cos\left(\frac{g\pi}{\kappa E_0}\right)) \left(\frac{\kappa E_0}{g}\right) \sin\left(\frac{g\pi}{2\kappa E_0}\right) \cos(\delta t)\cos(\delta t') \\
& + \frac{\delta}{g} \sin\left(\frac{g\pi}{\kappa E_0}\right) \left(\frac{\delta\kappa E_0}{g^2}\right) (1-\cos\left(\frac{g\pi}{2\kappa E_0}\right)) \sin(\delta t)\sin(\delta t') \\
& \left. + \frac{\delta}{g} \sin\left(\frac{g\pi}{\kappa E_0}\right) \left(\frac{\kappa E_0}{g}\right) \sin\left(\frac{g\pi}{2\kappa E_0}\right) \sin(\delta t)\cos(\delta t') \right].
\end{aligned}$$

We need go no further as the critical properties of the photon echo are evident. In the sum over all possible detunings these expressions will be highly resonant around $t=t'$. By equation (2.39) and the fact that signal detection will be accomplished by heterodyne beating with the laser beam (giving signals proportional to U and V) the echo decay with total delay $t+t'$ will go with a rate γ_{ab} .

CHAPTER 3

THE FREQUENCY--SWITCHED LASER

The Layout of the Laser

The frequency-switched experiments are based on a cw CO₂ grating controlled stable laser of the Freed design (Freed, 1968). This laser produces a .1 to .5 watt TEM₀₀ mode. The cavity layout is shown in Figure 3.1. The laser cavity length is approximately 1.45 meters, giving a longitudinal mode separation of greater than 100 MHz. This separation eliminates longitudinal mode competition through most of the gain bandwidth of laser transitions while still giving a long gain path and reduced sensitivity to frequency drifts arising from cavity length fluctuations. This results from the laser mix (60% He, 17% CO₂, 17% N₂, 4% Xe, 2% H₂) being set at about 13 torr, producing a homogeneous full linewidth of 100 MHz. Since the Doppler linewidth (FWHM) at room temperature is 60 MHz, we can consider the laser media to be primarily homogeneously broadened. This is particularly true with respect to the frequency switch which is of order only 6 MHz. We therefore do not need to be concerned by coherent optical transients induced in the laser media itself.

Frequency switching is accomplished via a 50 mm x 5 mm x 5 mm CdTe intercavity crystal placed less than 10 cm from the tuning grating. The crystal is cut for optimum modulation with the 111 planes parallel to the vertical sides of the crystal.

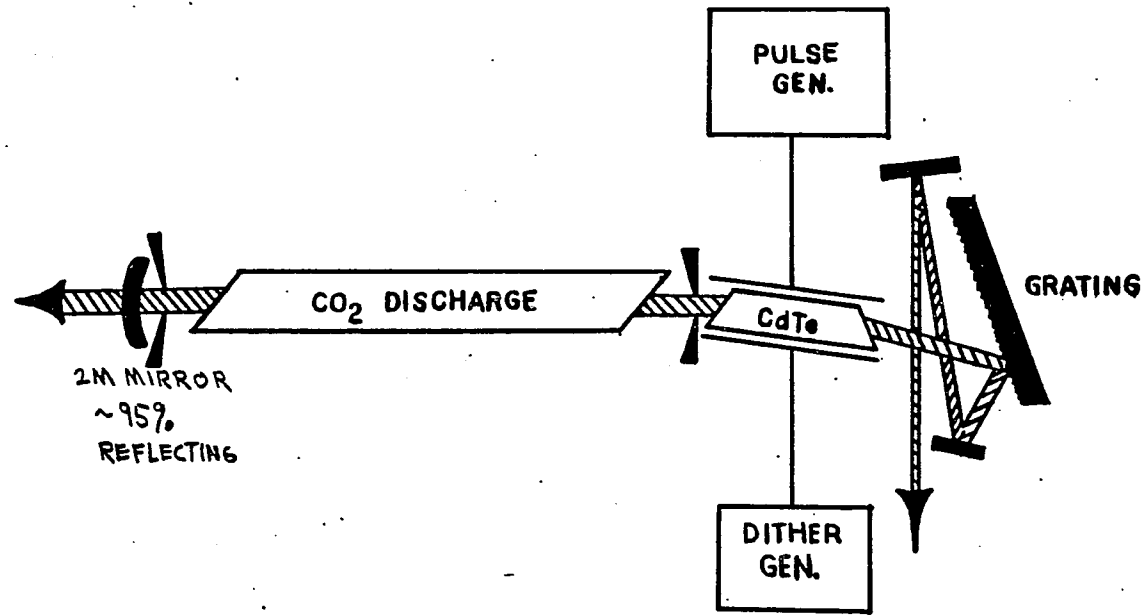


Figure 3.1. The frequency-switched laser.

The CO₂ discharge tube is a separately sealed-off dual anode center-cathode design with salt windows set at the 10.6 μ m Brewster's angles. The discharge region is 90 cm long and water cooled. The primary output coupler for the laser is a 95% reflecting ZnSe 2 meter mirror. The mirror is mounted on a hollow core pzt stack to provide for cavity length corrections during active laser stabilization. At the other end of the laser cavity and crystal is a 18 mm x 18 mm gold-on-brass substrate master ruled grating. The grating has 80 grooves/mm and is blazed at 23°30' for maximum efficiency to the first order at 10.6 μ m. On lasing, nearly 95% of the incident radiation is reflected back on itself by the first-order reflection. Close to 5% of the radiation is reflected into the 0th mode which exits the laser cavity via a special output window for use in our stabilization schemes. The grating's rotation is controlled by a micrometer drive. This allows the selection of nearly 50 lines in the P and R branches of the 9.6 and 10.6 μ m transitions without the crystal inserted; and about half that number with the crystal inserted.

The mirror-grating configuration represents a semi-confocal cavity, giving a Gaussian beam spot size of 2.2 mm near the crystal. A 4.5 mm diameter stop is mounted before the crystal on the discharge side to promote a clean TEM₀₀ transverse mode. A sampling of the expanded laser output is illustrated in Figure 3.2.

Against the crystal's vertical sides are applied kovar field plates. The uniform E field produced by these plates is perpendicular to the 111 planes. CdTe, being a $\sqrt{3}$ m crystal, has induced in it an electro-optical index of refraction ellipsoid. In this configuration

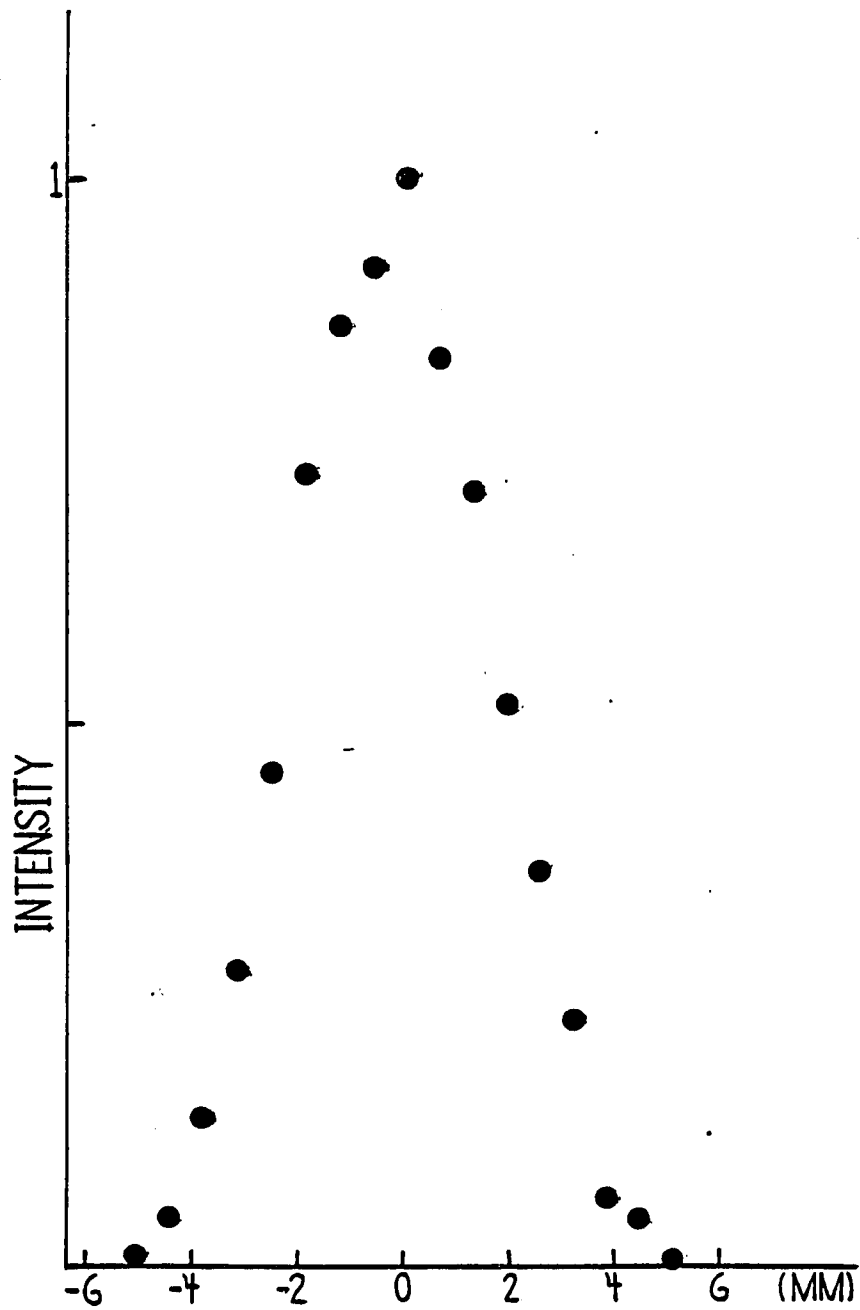


Figure 3.2. A typical cross-section scan of the frequency-switched laser's beam before the absorption cell.

the ellipsoid is rotationally symmetric about its short axis which is normal to the 111 planes. The degenerate long axis is given by $n_0 + \frac{1}{2\sqrt{3}} n_0^3 r_{41} |E|$ while the short axis is given by $(n_0 - \frac{1}{\sqrt{3}} n_0^3 r_{41} |E|)$, (Namba, 1961). The laser cavity mode is polarized along the short axis. The end faces of the crystal are cut at close to 4 milliradians from the normal to the crystal sides. These angles are to avoid instabilities from competing resonator cavities. To align the laser mode along the crystal axis, the crystal must be orientated with its length set at (using Snell's law and $n_0 = 2.64$) 10.7 milliradians to the unmodified laser cavity axis. As the crystal is essentially a fat prism, an axial ray emerging from the crystal on the other side would be displaced and bent in the horizontal plane when compared to the unmodified laser cavity axis. The net displacement of the ray by the time it reaches the tuning grating is about 2 mm. The grating dimensions are much greater than this displacement and its axis of rotation is vertical. Thus, this translation and deviation poses no problem aside from locating where to center an aperture stop if it is needed on this side of the crystal. It has been found that such an aperture is not needed. The crystal and plates are sandwiched by a two-piece Beryllium Oxide yoke with a thin layer of Apiezon-T grease to act as a damper on induced piezoelectric modes in the crystal and to provide better thermal contact. The yoke is water cooled with a temperature stabilized supply system. The crystal assembly is shown in Figure 3.3.

Since the internal laser mode is linearly polarized horizontally, a voltage applied to the crystal plates induces a small change in the

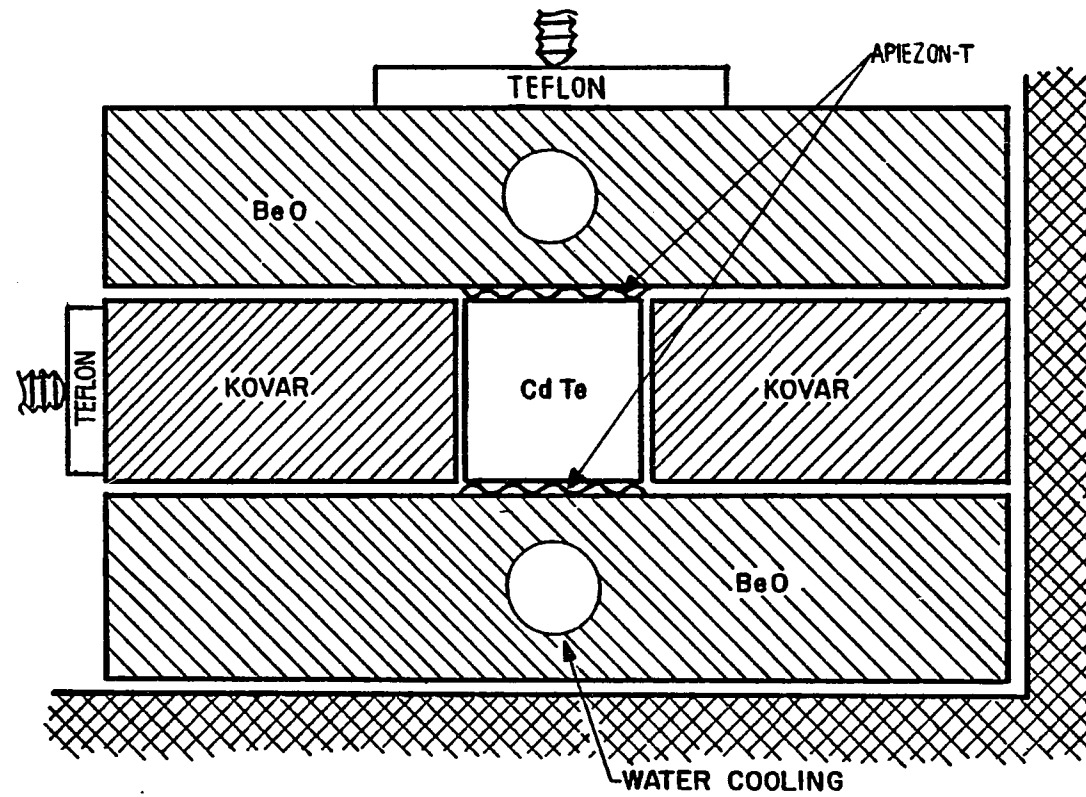


Figure 3.3. The cross-section of the CdTe modulation mount.

optical path length of the laser cavity as seen by this mode. A frequency shift results. This shift, $\Delta\nu$, is given by:

$$|\Delta\nu| = \nu_0 \frac{n_0^3 r_{41}}{\sqrt{3}} \left(\frac{V}{d}\right) \frac{L_c}{L} \quad (3.1)$$

Table 3.1 Laser Parameters

Gas Mix:	60:17:17:4:2 of He:N ₂ :CO ₂ :Xe:H ₂
Gas Pressure:	approximately 13 Torr
T ₁ :	3.7 x 10 ⁻⁴ sec. (Taylor and Bitterman, 1969)
T _{cavity} :	approximately 25 ns.
r (the pumping ratio):	approximately 2 (Yariv et al., 1973)

Table 3.2 Crystal Data Table (II-IV Inc., 1975)

Bulk Absorptivity, a:	.0012 cm ⁻¹ @ 10.6μm
Thermal Conductivity, 6:	.06 Watt/cm-°C
Temperature Change of Refractive Index, ∂n/∂T:	107 x 10 ⁻⁶ /°C
Refractive Index, n:	2.67 @ 10.6μm
Electro Optic Figure of Merit, n ³ r ₄₁ :	10 x 10 ⁻¹¹ m/volt @ 10.6μm

where ν_0 is the laser mode frequency, V is the voltage of the square voltage pulse applied, d is the field plate separation which equals crystal width, L_c is the crystal Length, and L is the full optical path length of the laser cavity. For 10.6μm radiation and the above listed laser and crystal parameters, $\Delta\nu$ should be approximately .01MH_z/volt. This figure compares with the averaged measured value of

.088 MHz/volt. This figure was obtained through beating the frequency switched laser's output with another stable laser's output for various voltage pulse amplitudes (see Figure. 3.4). The large change in beat amplitude seen in Figure 3.4 is completely consistent with the measured frequency response of the detector used. It is not representative of a laser power change during switching.

Laser Power Stability

The power stability of the laser is quite critical. The working theories for coherent transients assume no change in the amplitude of the driving fields. A power variation of order 5% would cast doubt on the applicability of these theories. Coherent transients in the laser media itself could be ruled out as explained earlier. Another possible source of power fluctuations can be ruled out since the rise and fall times of the voltage pulses to the crystal are greater or equal to 50 ns. This means that the cavity radiation passes through the crystal at least 10 times during the transition. To the light, the cavity appears to be changing length adiabatically. The original radiation mode in the cavity is then shifted to the new value. Hence, there is no sizable transients from a new tuned mode growing from the noise and an old mode dying away. Large switching transients can, however, be induced in the laser output. This is shown in Figure 3.5. Figure 3.6 shows that this transient can be largely eliminated by tuning of the laser line. This phenomenon appears because in steady-state the gain of the laser media at the lasing frequency must be clamped at the threshold value. In switching there must be a net transfer of energy

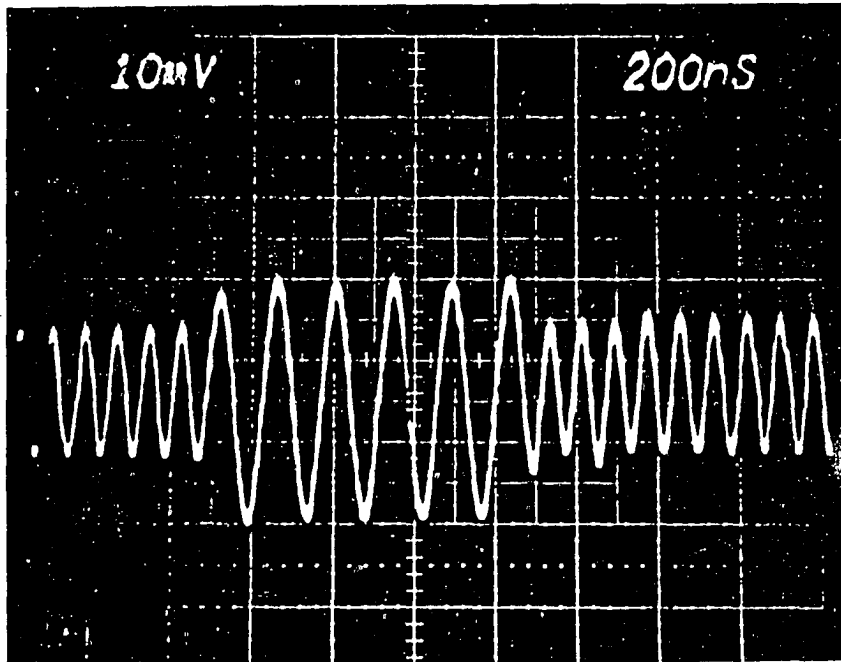


Figure 3.4. The beat signal of a frequency-switched pulse with the output of another stable cw CO₂ laser.

The apparent change in amplitude is due to the frequency response of the detector.

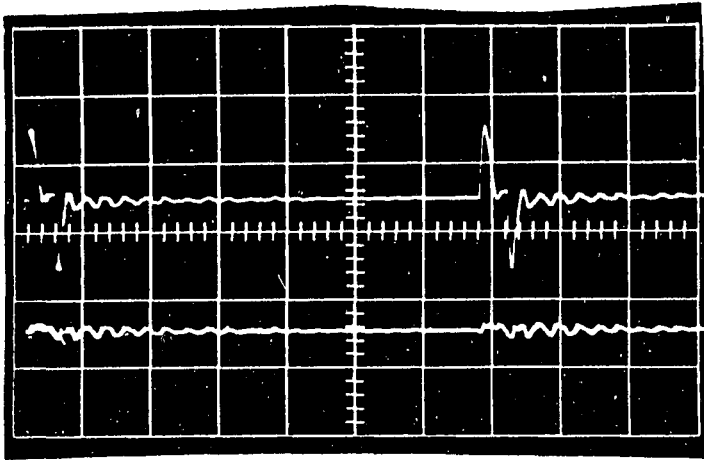


Figure 3.5. An oscilloscope photograph ($20\mu\text{s}/\text{cm}$) of the frequency-switched laser's output for two slightly different cavity tunings of the same line indicating a change in polarity of the large switching transient.

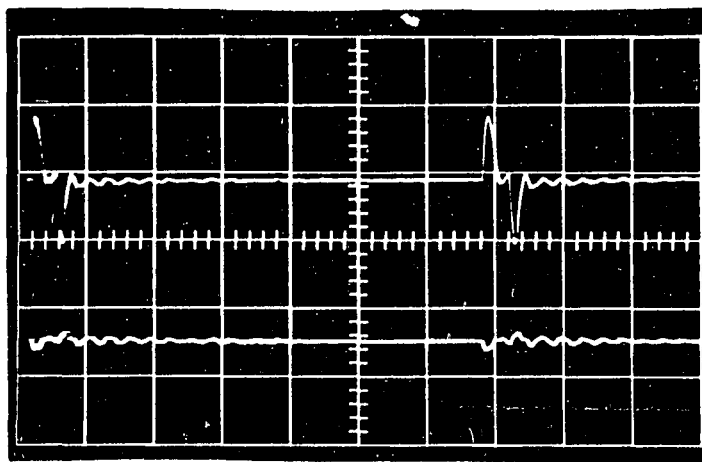


Figure 3.6. An oscilloscope photograph ($20\mu\text{s}/\text{cm}$) of the frequency-switched laser's output for two slightly different cavity tunings of the same line indicating that the large switching transient can be reduced to zero by proper tuning.

Note that there exists a smaller oscillation in the output that is independent of tuning.

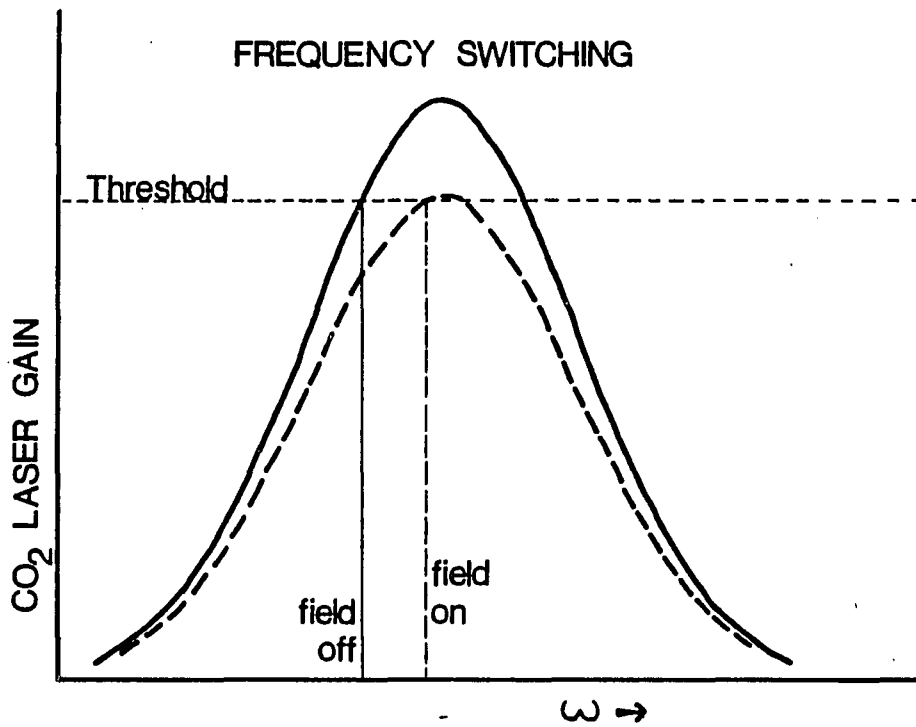


Figure 3.7. A large transient producing frequency-switch as viewed with the laser gain frequency distribution.

into or out of the gain media (see Figure 3.7). This energy transfer implies a laser power transient while it is occurring. It is clear from Figure 3.8 that a judicious choice of operating points in the gain profile should eliminate any power transfers. We need only switch about the peak in the gain curve so that at the initial and final lasing frequencies we have the same value of gain. A simple derivation can be used to understand this effect (Shoemaker et al., 1982). Consider the rate equations for an ideal homogenously broadened laser media. We can develop these equations along the lines of the relaxation oscillation calculations in Yariv's text (Yariv, 1975). We set the population difference equal to the population of the upper laser level, N ; we define W as the induced transition rate/atom, R as the pumping rate/unit volume, Q as the photon density inside the laser cavity, T_c as the cavity photon decay time, T_1 as the non-stimulated decay time of the population in the upper level, T_s as the natural decay time of the population difference, and $g(\nu)$ as the normalized pressure broadened line shape function. The rate equations for the laser are:

$$\begin{aligned}\frac{dN}{dt} &= R - WN - \frac{N}{T_1} \\ \frac{dQ}{dt} &= WN - Q/T_c\end{aligned}\tag{3.2}$$

From Yariv we know that $W = \frac{\lambda^2 c}{16\pi T_s}$ which can be written as $W=BQ$.

In frequency switching the driving term comes from the change in $g(\nu)$, thus the change in B . Denoting steady state terms with "0" subscripts, we write B as $B_0 + \Delta B$ where B is a constant, N as $N_0 + N'$, and Q as $Q_0 + Q'$. We assume that the deviation are small compared to the steady state values and find:

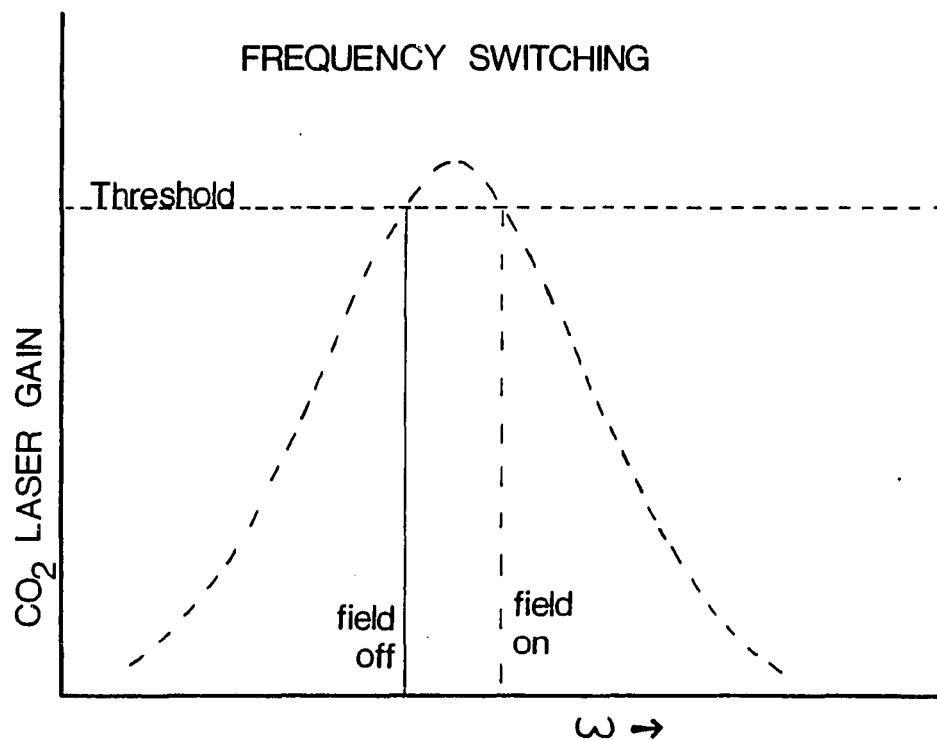


Figure 3.8. Frequency-switch without large transients as viewed with the laser gain frequency distribution.

$$\begin{aligned}\frac{dN'}{dt} &= -\left(\frac{1}{T_1} + B_0 Q_0\right)N' - N_0 B_0 Q' - Q_0 N_0 \Delta B \\ \frac{dQ'}{dt} &= B_0 Q_0 N' + Q_0 N_0 \Delta B\end{aligned}\quad (3.3)$$

We define r as R/R_t where R_t is the threshold pumping rate ($Q_0=0$). We use the relation amongst steady state terms, write ΔB in terms of the percentage change in B ($\Delta B = a \cdot B_0$), and use equation (3.3) to get:

$$\frac{d^2}{dt^2} Q' + \frac{r}{T_1} \frac{d}{dt} Q' + \left(\frac{r-1}{T_1 T_c}\right) Q' = \frac{Q_0}{T_1 T_c} a \quad (3.4)$$

Assuming that the switch occurred at $t=0$, the solution to equation (3.4) for the boundaries at $t=0$ is:

$$\begin{aligned}Q' &= Q_0^a e^{-(r/2T_1)t} \left\{ \frac{1}{w_m} \left[\frac{1}{t_c} - \frac{r}{2T_1(r-1)} \right] \sin(w_m t) - \frac{1}{r-1} \cos(w_m t) \right\} + \frac{Q_0^a}{r-1} \\ &\approx \frac{Q_0^a}{w_m t_c} e^{-(\frac{rt}{2T_1})} \sin(w_m t) + \frac{Q_0^a}{r-1}\end{aligned}\quad (3.5)$$

where

$$w_m = \sqrt{\frac{1}{t_c T_1} (r-1) - \left(\frac{r}{2T_1}\right)^2}$$

From Table 3.1 of laser parameter estimates, we see that the damped sine term dominates. Equation 3.5 has the amplitude varying directly with the size of the switching perturbation a and the sign of Q' depending on the sign of the switch. This is the observed behavior of the transient. The model is, however, very crude as CO_2 is very far from a two-level system due to the interaction of many vibrational and rotational manifolds. It has been found in gain saturation work (Christensen et al, 1969) that CO_2 calculations can be made in the two-level formulism if the manifold contributions are taken as a factor 50

enhancement to $1/T_1$. Doing this, in Figure 3.9 and Figure 3.10 we see that the predicted transient varies with roughly the same time scale as the observed but appears to have too low a damping. This is, in part, due to inaccuracies in some of the laser parameter estimates and due to the model's crudeness. Another source of error is due to the photon density variations both transversely and longitudinally in the laser cavity, each contributing its own w_m . We should then have to add all the contributions. This tends to wash out the oscillations beyond the first half cycle. Such a result is displayed in Figure 3.11 and is clearly closer to reality.

Figure 3.6 also indicates some sort of oscillating background even when the cavity mode-laser media interaction is tuned away. The oscillation is not another cavity mode interaction. This background can be observed in a CO_2 laser beam passing through the driven crystal external to the laser. It appears to be an electro-mechanically induced crystal twisting of the optical axis. The addition of the grease to the crystal mount did appear to dampen the background power oscillation. Figure 3.12 shows this background oscillation compared to 100% beam modulation. The oscillation appears to be of order 5% of full modulation. The chopper was run, however, at 180 Hz while the oscillation was more like 0.5 MHz . Since the preamplifier gain at the higher frequency is more than ten times the gain at the lower frequency, the crystal ringing amplitude is well below the level that would make it a problem as a power fluctuation.

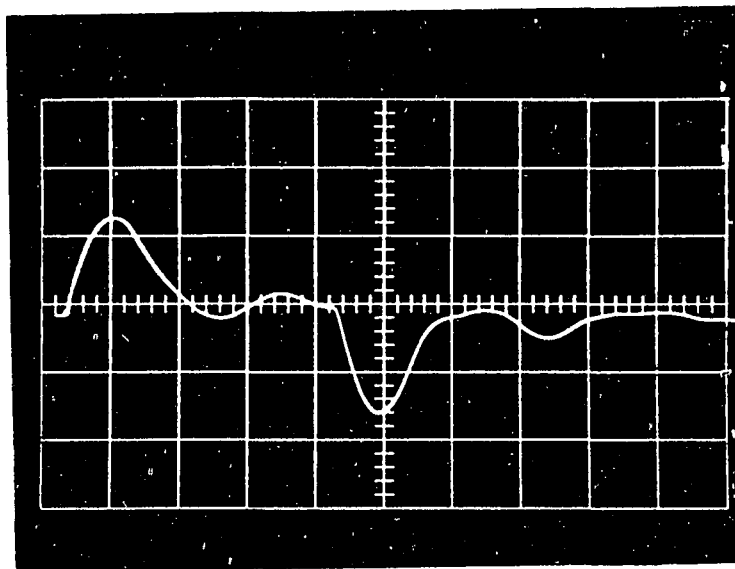


Figure 3.9. An oscilloscope photograph of the large transient produced by a 500 volt $8\mu\text{s}$ pulse on the crystal ($2\mu\text{s}/\text{cm}$).



PH= 8 MICS
 TI= 7.4E-06 SEC
 T-C= 2.5E-08 SEC
 RL= 1.5

POINT SPACING IS 200 NS

Figure 3.10. A computer simulation of figure 3.9 using eq. 3.5 ($200\mu\text{s}/\text{point}$).



PH= 8 MICS
 TI= 7.4E-06 SEC
 T-C= 2.5E-08 SEC

RL= 1.05
 RM= 1.4
 N PLS= 10

POINT SPACING IS 200 NS

Figure 3.11. A computer simulation of figure 3.9 using eq. 3.5 and allowing a 40% spread in light intensity through activity region viewed.

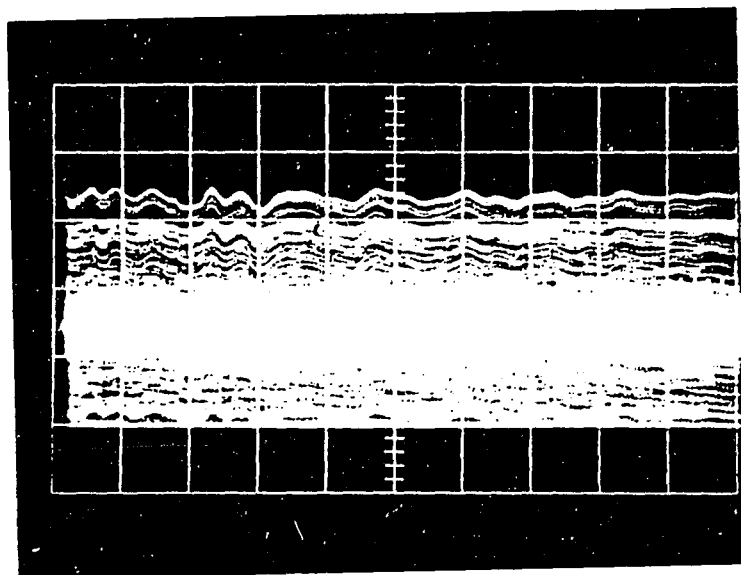


Figure 3.12. An oscilloscope photograph of the chopped laser output with the large transient tuned to zero.

Laser Frequency Stability

In converting the CO₂ laser to the frequency switching configuration, a major concern is the effect on the frequency stability of the laser. The separately mounted discharge tube and crystal assembly make the laser frequency more subject to vibration. Air turbulence in the optical path has been found to drive the laser off of its operating line. Isolating the eight ton laser table from the floor with inner tubes and sealing the laser cavity in a plexiglas case reduces these perturbations to a level controllable by our active stabilization scheme.

Running with the crystal introduces one other very serious source of frequency instability. The crystal parameters in Table 3.2, indicate that the crystals optical path length varies by 5.35×10^{-3} m/°C. This implies a lasing frequency variation of 100 MHz/°C. The full correction possible via the pzt is of this order also. Thus, for reliable active stabilization, the crystal thermal stability should be held to of order .1°C. To maintain thermal stability, the crystal is coupled to a 10 gallon actively stabilized water reservoir by flowing water through the BeO yoke.

During the development of the frequently switched laser one further question was raised as to laser stability in power and frequency. Given the crystal's low thermal conductivity, sizable index variation on temperature, it seems possible that our mode calculations can be thrown off by laser power dependent optical power in the crystal. Simple

considerations show that this effect is negligible. Consider the CdTe crystal to be a cylinder of length 50 mm and diameter 5 mm. Assume the two way power flow in the cavity to be 20 watts, corresponding to 1/2 watt output. Let the beam waist spot size at the crystal be 2.2 mm. Let a be the crystal's bulk absorptivity and σ its thermal conductivity. In steady-state, the power absorbed/unit length inside a circle of radius r about the center of the crystal must be equal to the power flow via conduction through the boundary define by the circle

$$\int_0^r aI(r')2\pi r' dr' = -\sigma 2\pi r \frac{dT}{dr} \quad (3.6)$$

where for a Gaussian intensity profile,

$$I(r') = \frac{2P}{\pi\omega_0^2} e^{-2r'^2/\omega_0^2}$$

and P is the total power.

Integrating the above and noting that $\frac{dn}{dr} = \frac{dn}{dT} \frac{dT}{dr}$

we find:

$$\frac{dn}{dT} = \frac{aP\omega_0^2}{4\pi\sigma r} \left(\frac{dn}{dr} \right) (e^{-2r^2/\omega_0^2} - 1) \quad (3.7)$$

We can replace the term, $(e^{-2r^2/\omega_0^2} - 1)$, with $\frac{2r^2}{\omega_0^2}$ in equation (3.7)

except for r near the crystal edge. For most of the interior of the crystal we can write:

$$\begin{aligned} n(r) & \frac{aP}{4\pi\sigma} \frac{dn}{dT} r^2 + n_c : n_c \text{ a constant} \\ & \approx 3.4 \times 10^{-6} r^2 + n_c \end{aligned} \quad (3.8)$$

If we use the paraxial ray matrix expressions found in Yariv's text, page 101, for a media with a quadratic index profile and use the small angle approximations we find that the matrix is of the form:

$$\begin{bmatrix} 1 - \left(\frac{Rd}{2}\right)^2 & d \\ -R^2d & 1 - \frac{(Rd)^2}{2} \end{bmatrix} \approx \begin{bmatrix} 1 & d \\ -R^2d & 1 \end{bmatrix} \quad (3.9)$$

where $R = 3.4 \times 10^{-6} \text{ cm}^{-2}$ and $d=5 \text{ cm}$.

Noting that a thick, weak lens in this formulation would be of the form:

$$\begin{bmatrix} 1 - d & d \\ -1/f & 1-d \end{bmatrix} \approx \begin{bmatrix} 1 & d \\ -1/f & 1 \end{bmatrix} \quad (3.10)$$

we see that the crystals optical power is, in comparison to typical fabrication tolerances, zero ($f_{\text{crystal}} = 320\text{m}$).

Typical experimental runs on this system last from four to ten hours. Free running, the laser drifts significantly, as evidenced by growth of the switching transient, in a matter of 20 seconds to a few minutes, depending on environmental noise. Active stabilization is thus an absolute necessity. Two schemes have been tried successfully. The first method, used during the critical echo experiments, is a frequency dither/lock-in technique (Thomason et al., 1975). In this case a 1 kHz trapezoidal voltage wave form is applied to one of the crystal plates. The amplitude of this signal is set at about 50 volts, producing to a frequency dither in the laser output of 500 kHz. The rise and fall times of the dither voltage are set greater than $40\mu\text{s}$. At 1kHz, any faster rise and fall times induce large laser power oscillations via crystal vibration. The transient experiments are timed to occur during the top

or bottom flat region of the dither waveform. The dither signal in the grating output (essentially from the inhomogeneous solution in (3.5)) is detected on a molelectron P4-73 pyro-electric detector with a twin-tee feedback preamp set at 1kHz. This signal is then sent to an Evans phase sensitive detector board (model 4110 lock-in) and an Evans phase control unit (model 4114) driven by the original crystal driving signal. The lock-in output is sent to an integrator with a hold time of around 30 seconds. The integrator output drives a voltage-controlled power supply with a maximum output of 500 volts. This voltage moves the laser output mirror by way of a pzt stack. See Figure 3.13. If the dither is about the peak in the power curve (Figure 3.14), then there is no fundamental frequency component in the signal at the detector. In this case the output of the integrator does not change, thus the pzt does not move. Drifting to higher or lower frequency induces a fundamental frequency component in the output producing a positive or negative voltage from the lock-in depending on the direction of the drift. This causes a shift in the integrator output, resulting in the power supply adjusting the mirror position in the proper direction. Frequency stabilizing about the gain peak allows for minimizing the switching transient as well. A dc output voltage offset on the lock-in allows for fine tuning of this transient.

The alternate line locking method uses the switching transient directly (Scotti, 1982). The transient is monitored on a Au:Ge ℓN_2 -cooled detector whose output goes to a gated integrator (PAR 164). The output of the gated integrator drives a voltage controlled power supply and pzt in the same manner as above. The integrator is triggered from

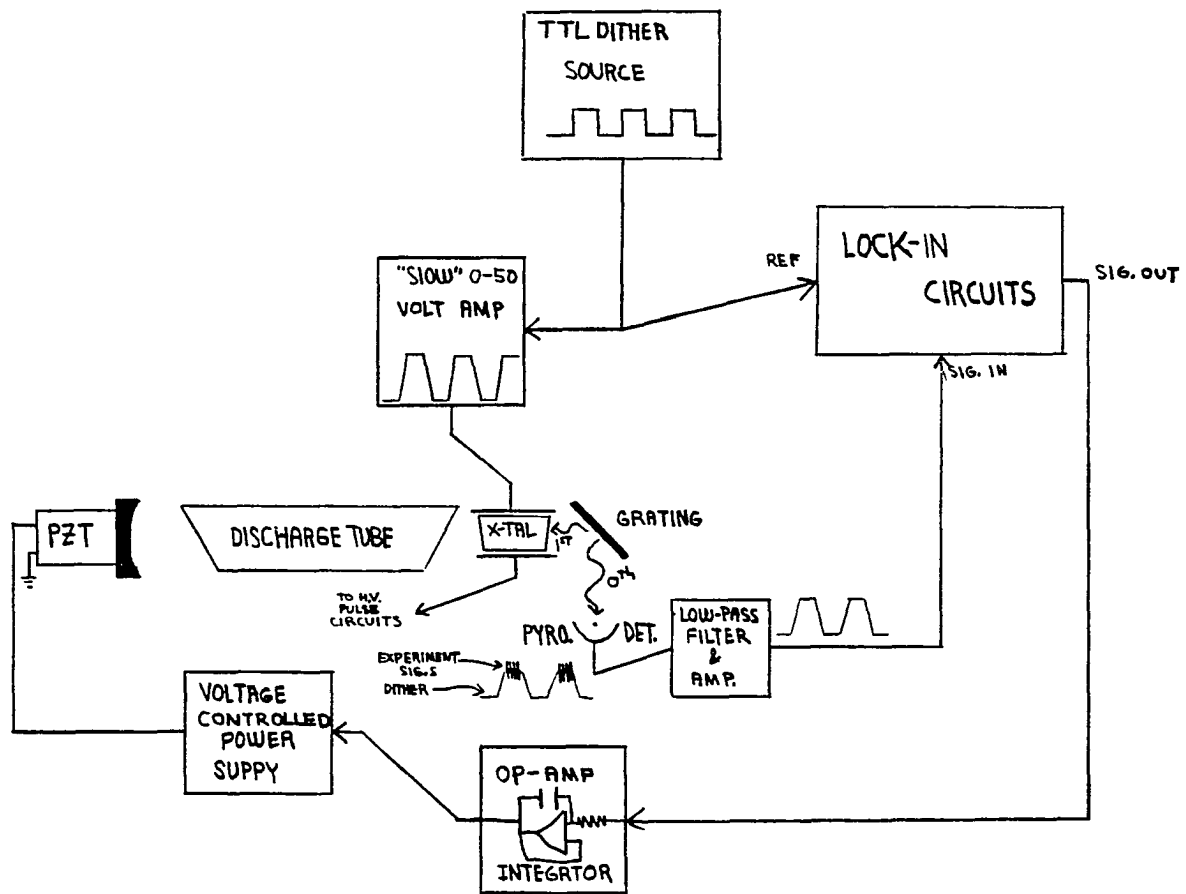


Figure 3.13. The frequency stabilization scheme for the frequency-switched laser

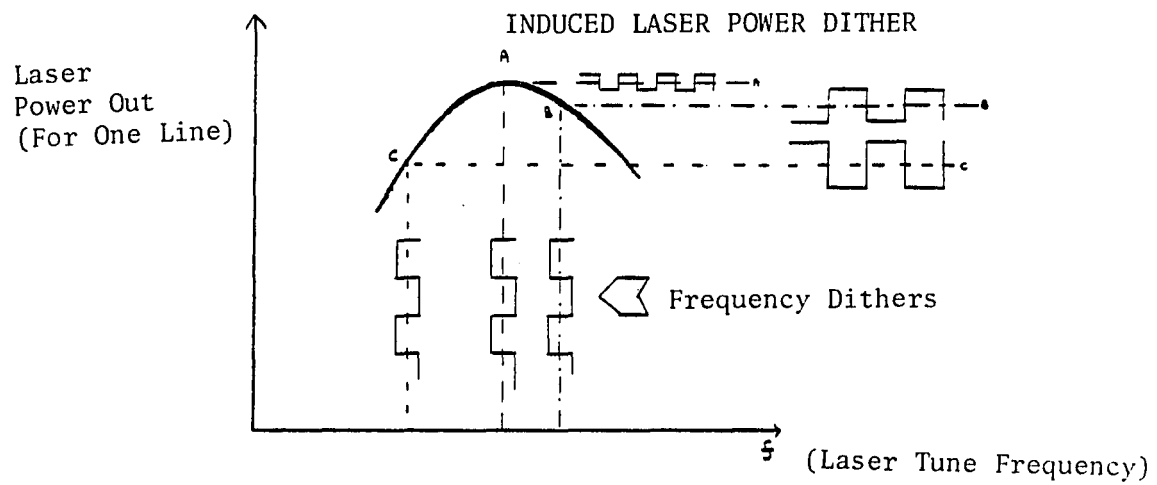


Figure 3.14. How the laser stabilizer error signal varies with various detunes.

the experiment's synchronization pulses. Its window is manually adjusted to the point where a switching transient peak occurs. The locking behavior of the two methods are about the same. From beating experiments the long term (hr) frequency drift is estimated to be of order the frequency dither, .5 MHz. The lock's time response is faster than the drift times of the laser. The perturbation to the laser frequency that can be corrected with one second integration time, as determined by the size of the switching transient, is greater than five times the extent to which the laser drifts in one second running passively.

Thus we have developed, using careful passive and active stabilization measures on the crystal and laser cavity and by proper internal beam aperturing, a cw power, stable frequency switched laser with a good TEM₀₀ mode output.

CHAPTER 4

THE TRANSIENT SPECTROSCOPY LABORATORY SYSTEM

General Laboratory Layout

The transient spectroscopy experiments are built around a Z80A based micro-computer. This arrangement provides precise and repeatable control of the pulse timing delays, cumulative storage of the signal, enhanced signal-to-noise by subtraction out the background signal from the desired signal, and much of the data reduction needed in analysis.

Figure 4.1 and 4.2 show the basic laboratory layouts for the frequency switched and ARP experiments. The basic laboratory setup and data acquisition system used in the frequency-switched experiments is also used in the ARP runs. The main change is that an unmodified Freed designed CO₂ laser with a sealed-off gain cavity is used. This laser is stabilized similarly to the frequency-switched laser except that the dither signal is supplied to the mirror's pzt in the form of a 1 kHz sinusoid. Outputs of 3 watts with TEM₀₀ mode are possible with this laser.

In the frequency-switched layout, the laser output can be either diverted via a removable mirror through a 190 Hz chopper to a 1/4 meter monochromator and pyroelectric detector combination for operating line determination, or it can be passed through an approximately 2X power collimating telescope. Once collimated, the beam is sent through a

60 cm long, 3 cm i.d. pyrex tubular absorption cell sealed at the ends with salt windows. The cell is connected to a vacuum system consisting of a rotary mechanical pump and an oil diffusion pump operational to better than 10^{-6} torr. During the experiment, the test gas's pressure can be monitored by a Datametrics type 1014 A capacitance manometer. With this system, controlled pressures of the subject gas can be studied. The pressure range used in frequency switching experiments are from 0.5 to 20 mtorr.

For the ARP system, line designation is determined by the characteristic Stark fields required to tune the various coincidences of the molecules vibration-rotation transitions with the CO_2 line. An absorption cell containing the Stark plates replaces the simple cell used in the frequency-switched experiments. This cell is connected to the vacuum system in the same manner as the simpler cell and NaCl windows are used here also. Pressures are kept below 9 mtorr to avoid arcing in the Stark cell. The two Stark plates are 4 x 30 cm stainless steel plates separated by .4445 cm with six precision quartz spacers. The inner plate surfaces are polished optically flat to within .0003 cm. These plates are oriented such that the Stark field is parallel to the linear polarization of the laser's output. This is done to give $\Delta M=0$ selection rules. Two Germanium AR-coated meniscus lenses are used to form a collimating telescope for the beam before it enters the cell. The beam spot size is about 1.8 mm. This waist gives good beam quality between the plates by minimizing beam reflections on the plates. This beam width also gives the light intensities necessary for the ARP conditions.

Coherent transients in the forward direction are observed on a Honeywell HgCdTe photodiode. This detector gives a bandwidth of about 20 MHz in combination with its preamplifier. In the frequency-switched system, the detector signal is high pass filtered ($f_c = 1\text{MHz}$) to cut down on the slow background laser power oscillation. The signal is then processed through a PAR model 162 boxcar averager with a PAR 164 gated integrator. This unit has a resolution of 10 ns. The boxcar is triggered by a synchronization pulse from a TTL based timing box. The gated integrator's window is scanned under computer control via the voltage from a D to A converter. Through software control the window can be scanned at a rate such that it either just matches the pulse one to pulse two delay interval changes or at twice that rate (see Figure 4.3). The former case is used for nutation studies to observe the media's driven response during pulse two. The latter case is used in echo studies where the desired signal occurs at twice the pulse delay. The rate at which the pulse spacing jumps as well as the size of the pulse steps are software controlled. Thus, the integration time of the PAR and the size of the signal stored is software controlled. The initial pulse separation and the number of steps are also under computer control. These parameters do not define the system resolution since the time separations between consecutive stored sampled points are smaller than the detector resolution. For each step in the window delay, the computer reads the boxcar's output via an 8-bit A to D converter, sends an integrator clear signal, and stores the signal value in memory along with its delay time co-ordinate.

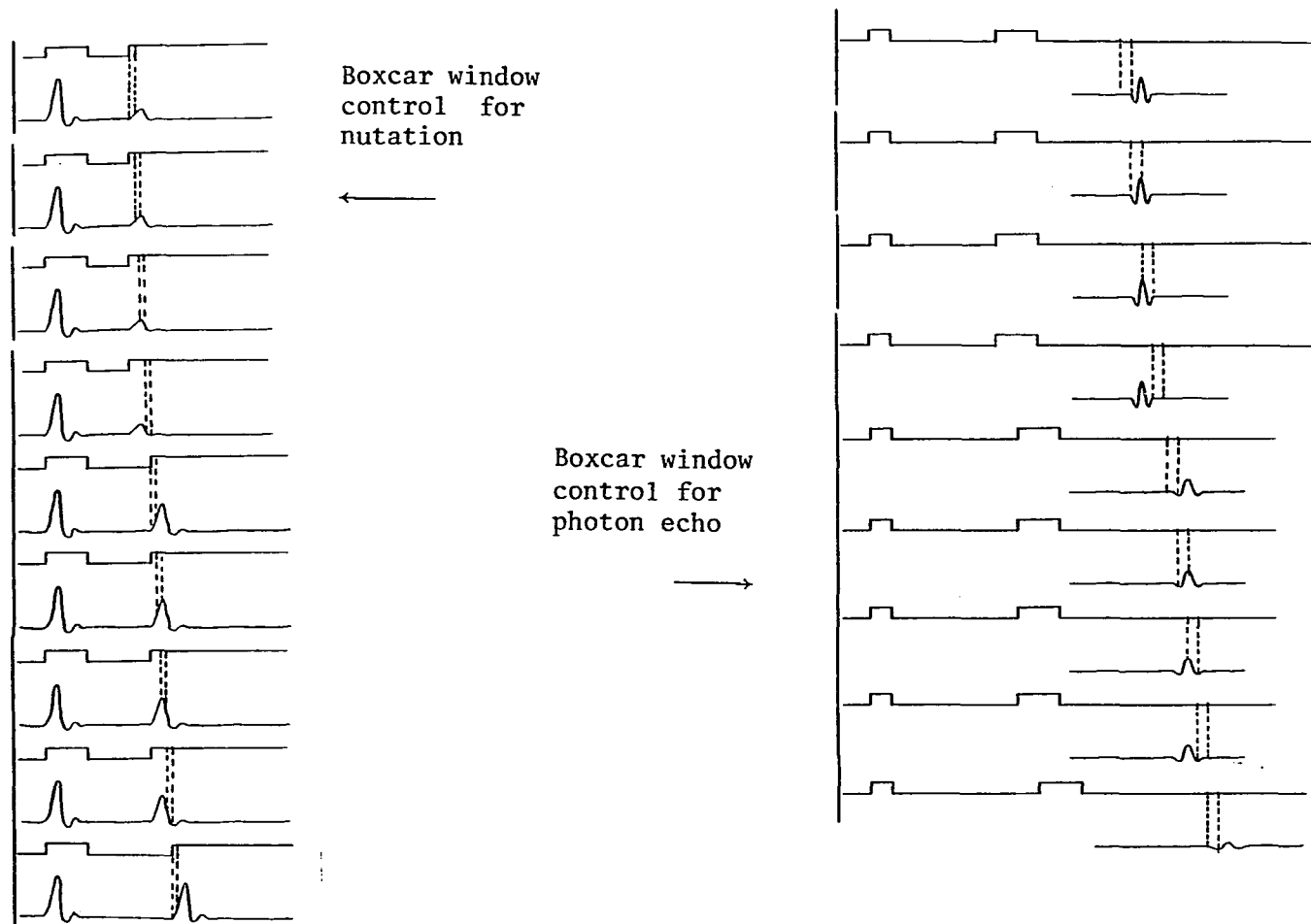


Figure 4.3. The Boxcar window control scheme for delayed-nutation and photo echo experiments.

Data Acquisition System's Linearity

The linearity of the data acquisition system is of prime importance. The boxcar integrator's specifications for linearity permit no more than $\pm .1$ volt signal inputs. Test on the boxcar computer system indicate a much lower limit. A bipolar linear voltage ramp was applied to the boxcar input. Its full peak to peak voltage was under the published input limits for the integrator. The system was run for various numbers of scans and integration times, all well past the point where data would "fold over" (in the ram memory the data is stored as a signed 16 bit number and thus, the next count over $7fff_H$ is $-7fff_H$ and the next under $-7fff_H$ is $7fff$). The distortion in the ramp signal in the "unfolded" region did not depend on integration time but did depend strongly and inversely on the number of scans, consistent with a voltage input limitation at the A to D. Each point's count divided by the number of scans is proportional to the input voltage. In this way a limit for the input voltage to maintain signal linearity in storage is obtained. This limit is less than half of the boxcar limit. From figures 4.4 and 4.5 a "safe" operational criterion can be chosen to maintain linearity. To be certain of maintaining voltage inputs below the distortion free limit, one need only avoid data fold over and maintain about 40 scans per run.

Data Taking Procedures

In the SF_6 echo experiments an 11 transient (11 delay interval changes) single scan is typically obtained in 8 seconds (about 700 data points and 700 time co-ordinates over $5\mu s$). Since 12k of memory

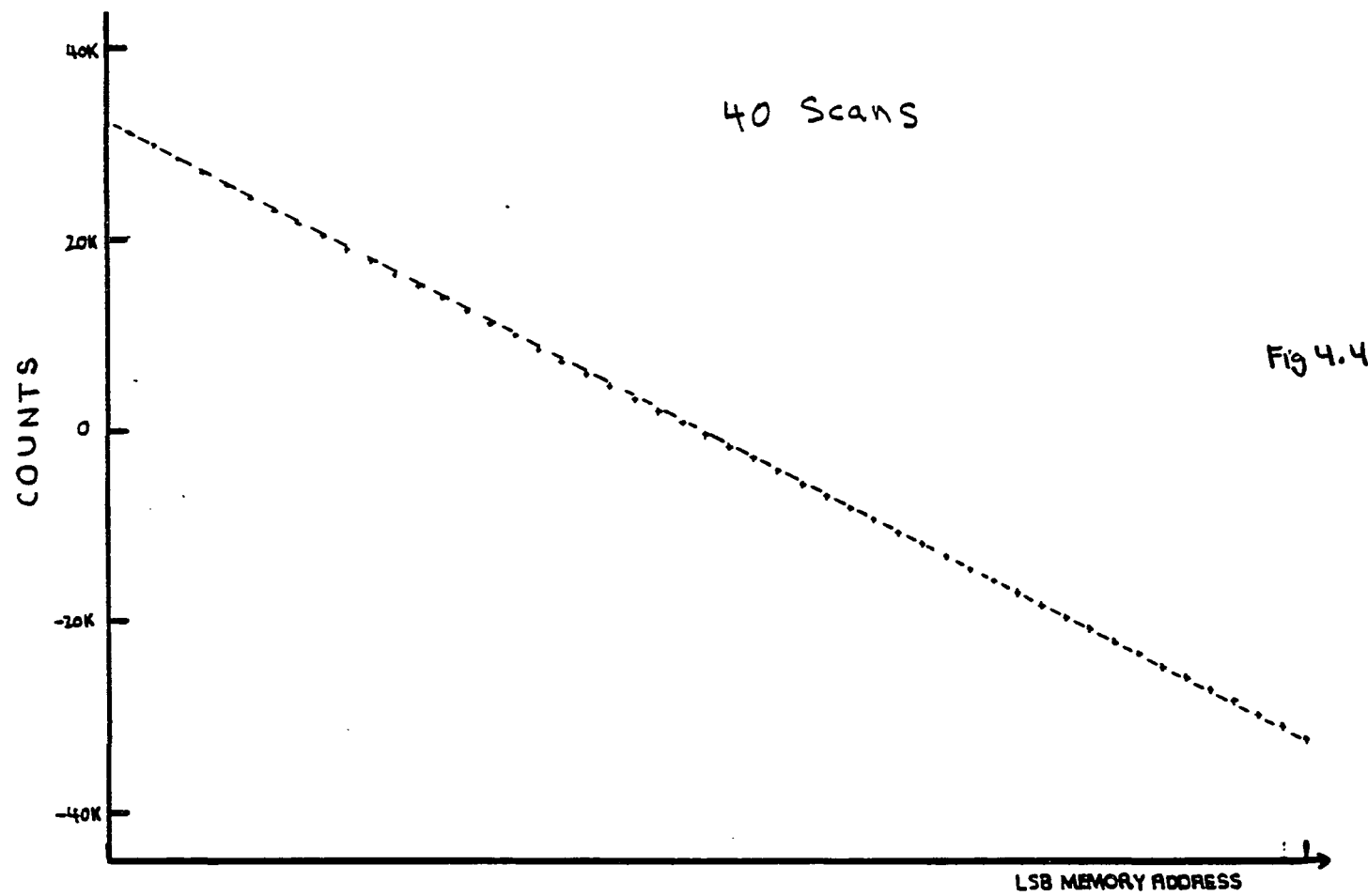


Fig 4.4

Figure 4.4. A demonstration of system linearity with typical running parameters using a linear voltage ramp into the boxcar.

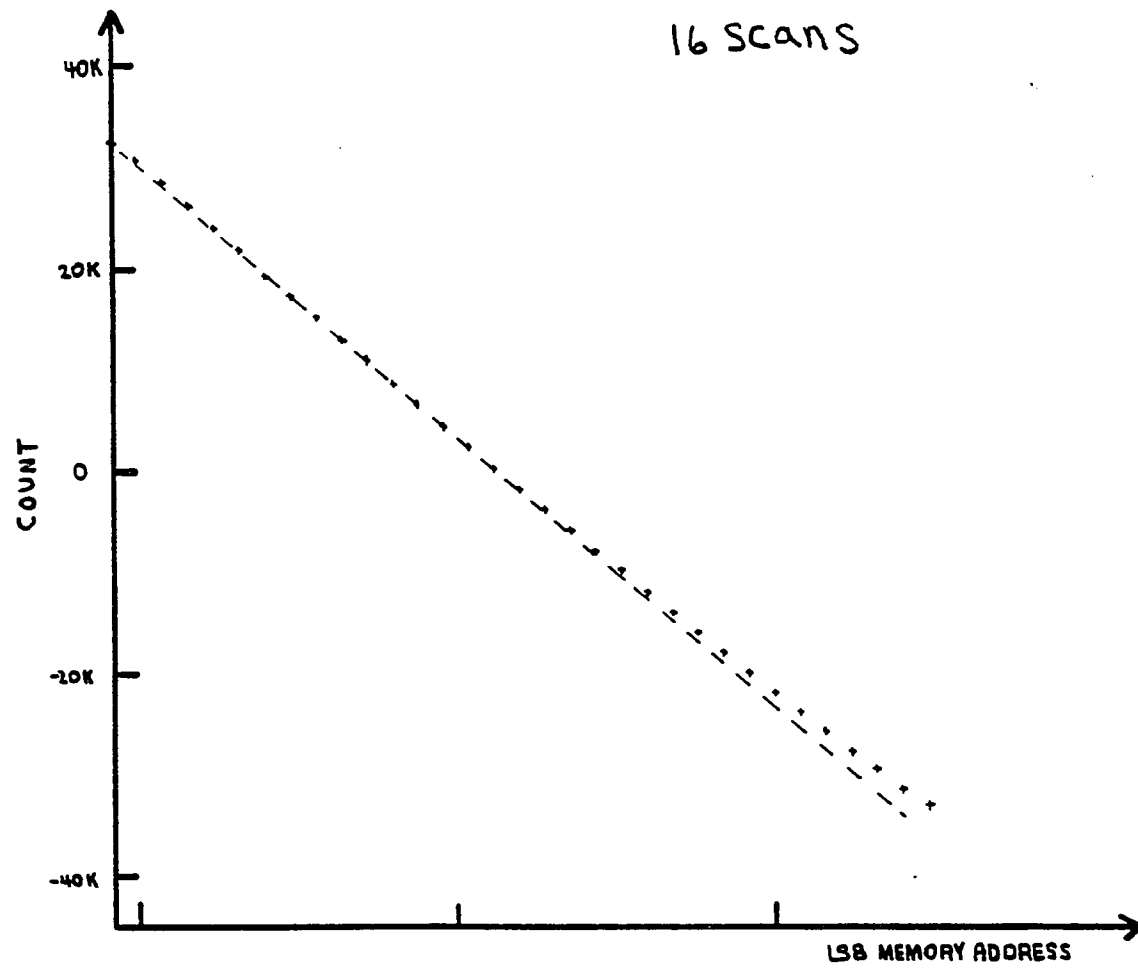


Figure 4.5. A demonstration of the breaking of system linearity with larger input signals than in figure 4.4.

storage is available, a higher density of echo amplitude measurements over the observation time can be made. The computer is programmed to do a sequence of different scans based on up to six fractionally different initial delays. Completing this sequence constitutes one scan. The computer then proceeds to repeat this procedure for typically 40 scans. The sample gas is then pumped out and the entire sequence repeated. In this way, the background crystal ringing can be stored for later subtraction from the data.

For a complete data or background run 15 minutes are required. Typically 20 different pressures are studied. Nutation based experiments, both by the frequency-switched laser and in the ARP experiment, demands less time as the transient observed can be more closely "packed" in a single scan, eliminating the need for multiple off-set scan sequences.

Unlike the amplitude, the detailed shape of the transient signals depend on many variables. No fit is attempted to the recorded signals directly. The amplitude is simply measured for each transient recorded. In the nutation experiments, each initial spike is delayed graphically on a crt and the peak count subtracted from the base line using a computer routine (see Figure 4.6). In the echo experiments, the heterodyne beat of the echo radiation with the unshifted laser output is detected. The switched frequency radiation has a fixed phase relationship with the unswitched radiation, determined by the switch rise time. As echo formation is essentially a time reversal of dipole phasors back to the state at the end of pulse one, the phase and

frequency of the echo beat will be the same for all delays. Thus, it is legitimate to monitor the same 3 most distinct adjacent maximums and minimums for all the echoes in a run. The echoes are displayed in the same manner as the nutations and the counts corresponding to these three points, a_1 , a_2 , a_3 , noted. The variation of the quantity $(a_1 + a_3 - 2a_2)/2$ over the delay times is taken as the variation of the echo amplitude (see Figure 4.7). In both echo and nutation experiments, the roughly 2000 data points per pressure and their time co-ordinates produce about 30 amplitude data points and their time co-ordinates. From this reduced data theoretical fits are applied.

Basic Electrical and Timing Layout

Figures 4.1 and 4.8 show the basic electrical layouts of the frequency switched experiments. The experimental timing is set by the TTL timing box. This box has its own independent 1 KHz and 20 MHz clocks. The 1 kHz clock is fed to a 50 volt pulse amplifier to dither the crystal in the stabilization scheme discussed in Chapter 2. It also sets the time for the start of the experiments repetition rate burst (set around 8 kHz). A delay in the burst with respect to the rising edge of the 1 kHz pulse train is wired in to avoid overlapping the experiments with the slow rise in the dither voltage pulse. The repetition rate pulses and 20 MHz clock produce one pulse on their first overlap via an edge-triggered flip-flop. The first edge of this pulse defines the experiment's synchronization pulse which triggers the boxcar and monitoring scopes. This pulse also enables a counting circuit used as a fixed delay circuit. On count down a flip-flop is triggered and

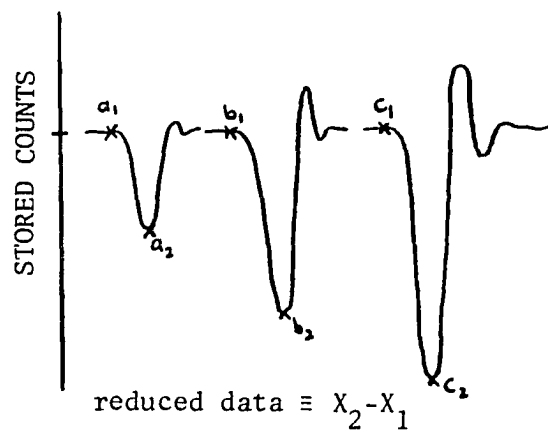


Figure 4.6. The scheme for the initial data extraction from raw data in delayed nutation.

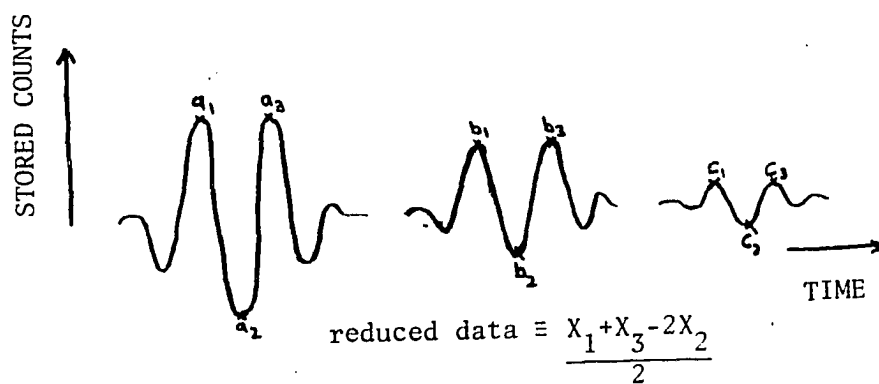


Figure 4.7. The scheme for the initial data extraction from raw data in photon echo experiment.

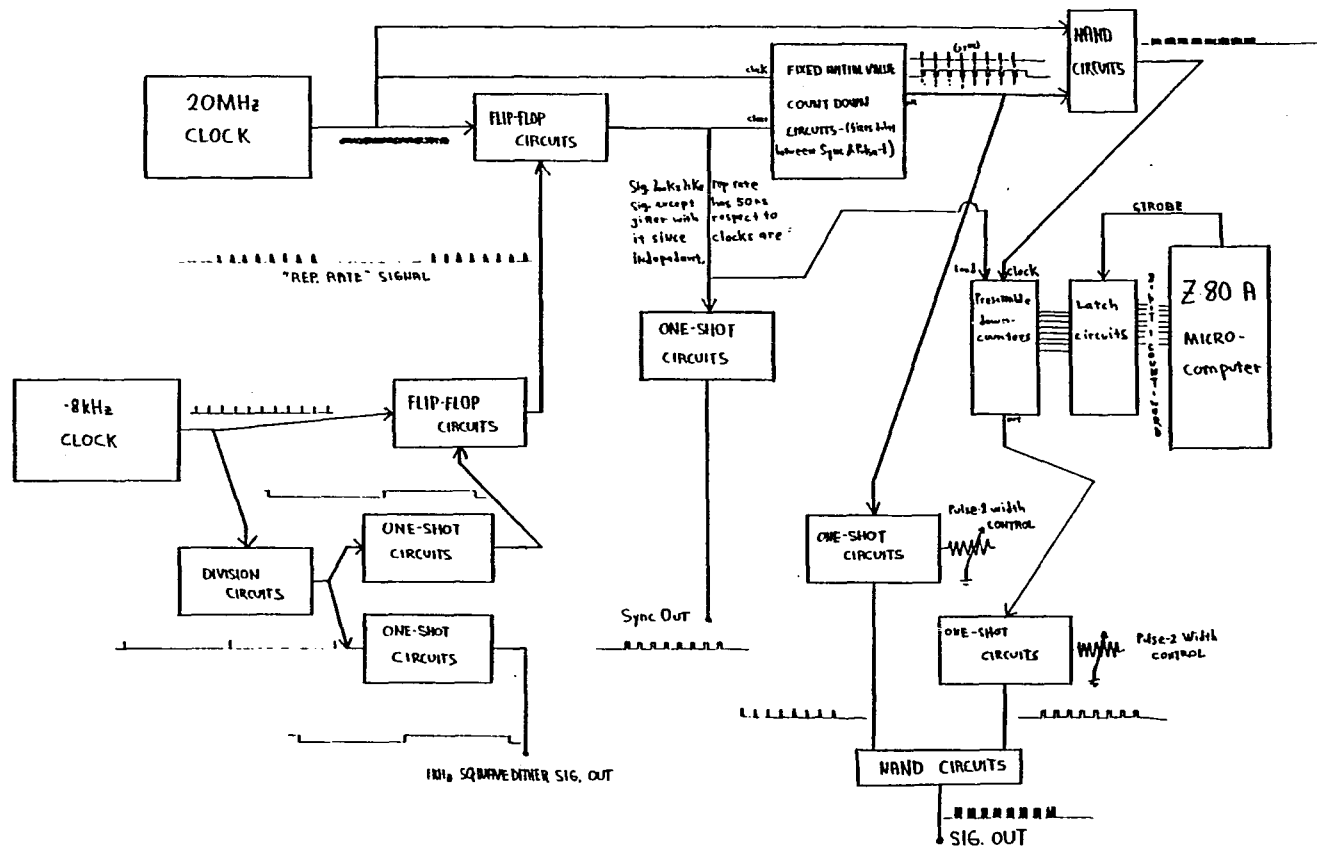


Figure 4.8. The timing schemes for the coherent transient experiments.

a presetable count down circuit is enabled. The flip-flop fires a one-shot which defines the first frequency shifted pulse, pulse-one. The presetable count-down circuit is set by command from the computer by way of an 8-bit parallel port connection and latch circuits. In turn, this count down circuit fires another flip-flop and one-shot combination which defines the second pulse, pulse-two. Both pulse-one and pulse-two are put on the same line using NAND gates. This signal is sent to a 50 volt pulse amplifier which in turn drives the high voltage pulser, either a Velonex or Cober unit. These units are both capable of up to 2000 volt pulses with 50 ns rise and fall times. Typically 500 to 600 volt pulses are used. The widths of pulses one and two are manually set by adjusting the one-shot time constant resistors. Since the computer counts pulse separations between the leading edges of the pulses, these widths must be noted for the proper correction of the pulse width separations. The high voltage output is coupled to one side of the crystal. This line is also connected to a 400 ohm load to ground via a non-shielded cable to control ringing and maintain the fast rise and fall times of the high voltage pulse. To the other crystal plate is applied either the dither voltage using the original stabilization scheme or ground under the later scheme discussed in Chapter .

The above TTL two-pulse timing box is also used as the time source for the ARP voltage ramp and the probe pulse. Pulse-one triggers a TTL 8 μ s probe which is amplified to drive the high voltage pulser. The rise time of the voltage output is slowed via a series resistance coupled to the capacitive load of the Stark plates. The peak voltage is limited

by a Zener diode so that the rate of rise of the voltage ramp could be controlled by varying the Cober output voltage without fear of gas breakdown. Pulse-two defines a separate pulse which is amplified and drives a fast switching transistor. This transistor shorts the voltage across the cell to another Zener diode, producing a well defined probe pulse for nutation. This arrangement allows the already existing delayed nutation control program to be used in this experiment. One can also simply convert back to the more traditional pulsed delayed nutation experiments by removing the series resistor and driving the Cober with the complete amplified output of the timing box. All the above connections to the Stark plates are to only one of the plates. The other plate is connected to a stable high voltage power supply. In this way the desired molecular transition can be tuned into resonance.

Finally, the TTL box's square wave dither signal is also used for stabilization in the ARP experiments. The signal is converted to a sinusoidal signal using a 0 to 10 volt, 1 kHz active notch-filter and amplifier. This signal supplies the dither signal to the laser mirror's pzt.

CHAPTER 5

THE SF EXPERIMENTS

The Choice of Molecule and Transition

The nonpolar molecule SF₆ was chosen as the initial subject of study for the frequency switched laser. It was chosen because of the large signals obtainable via the 10.6μm laser line overlaps and the sizeable literature dealing with previous pulsed studies of the system. The experiments were used as a test of the frequency switched system as well as an observation of decay processes in SF₆.

Both delayed nutation and photo echo experiments were done. The P(16) laser line was used primarily, since absorption studies at room and dry ice temperatures indicated that this line overlap is dominated by a ground state absorption even at room temperature (Lyman et al., 1978). This absorption is due to the Q(38) line of the $\nu_3 = 0 \rightarrow 1$ band (McDowell et al., 1977).

Previous Work in SF₆

As there exists no permanent dipole in SF₆, no Stark tuning experiments are possible. All previous experiments have been done with pulsed lasers. As a result little has been done quantitatively with the nutation effect outside of some estimates of the average transition dipole matrix element based on the nutation frequency (Hocker and Tang, 1969; Alimpiev and Karlov, 1974). There have been seven previous

photon echo studies of SF₆ (Patel and Slusher, 1968; Gordon et al., 1969; Alimpiev and Karlov, 1973; Meckley and Heer, 1973; Gutman and Herr, 1975, 1977; Heer and Nordstrom, 1975). In these experiments, two short CO₂ laser pulses separated by a variable delay time, t were applied to the dilute gas sample. The spontaneously emitted echo pulse was observed after a delay of t from the second laser pulse and its amplitude noted. The apparently exponential decay of this amplitude gave γ_{ab} . It was found that $\gamma_{ab}/P = .045\mu\text{s}^{-1} - \text{mtorr}^{-1}$, where P is the pressure. It should be noted that the signal to noise ratios in such experiments are limited due to pulse-to-pulse variations inherent in the pulsed CO₂ lasers.

Preliminary Work

Our first frequency switched experiments, which were run before the computer controls were operational, were photon echo sequences. These runs were done under manual control with the box car in standard mode with its output sent to an x-y plotter. No background subtraction was done. An example of the raw data is shown in Figure 5.1. Figure 5.2 shows a plot of Log(echo amplitude) versus time for one pressure. Figure 5.3 shows a plot of the measured decay rate versus pressure. Reduction of this data gives $\gamma_{ab}/P \approx .05\mu\text{s}^{-1} \text{ mtorr}^{-1}$, in reasonable agreement with the previous experiments.

In Figure 5.2 one sees that this noisy data seems to display a non-linear component, though hard to resolve in a quantitative manner.

With the lab system fully operational it was now clear that the echo decay is of a more complex nature (see Figures 5.4 and 5.5). The

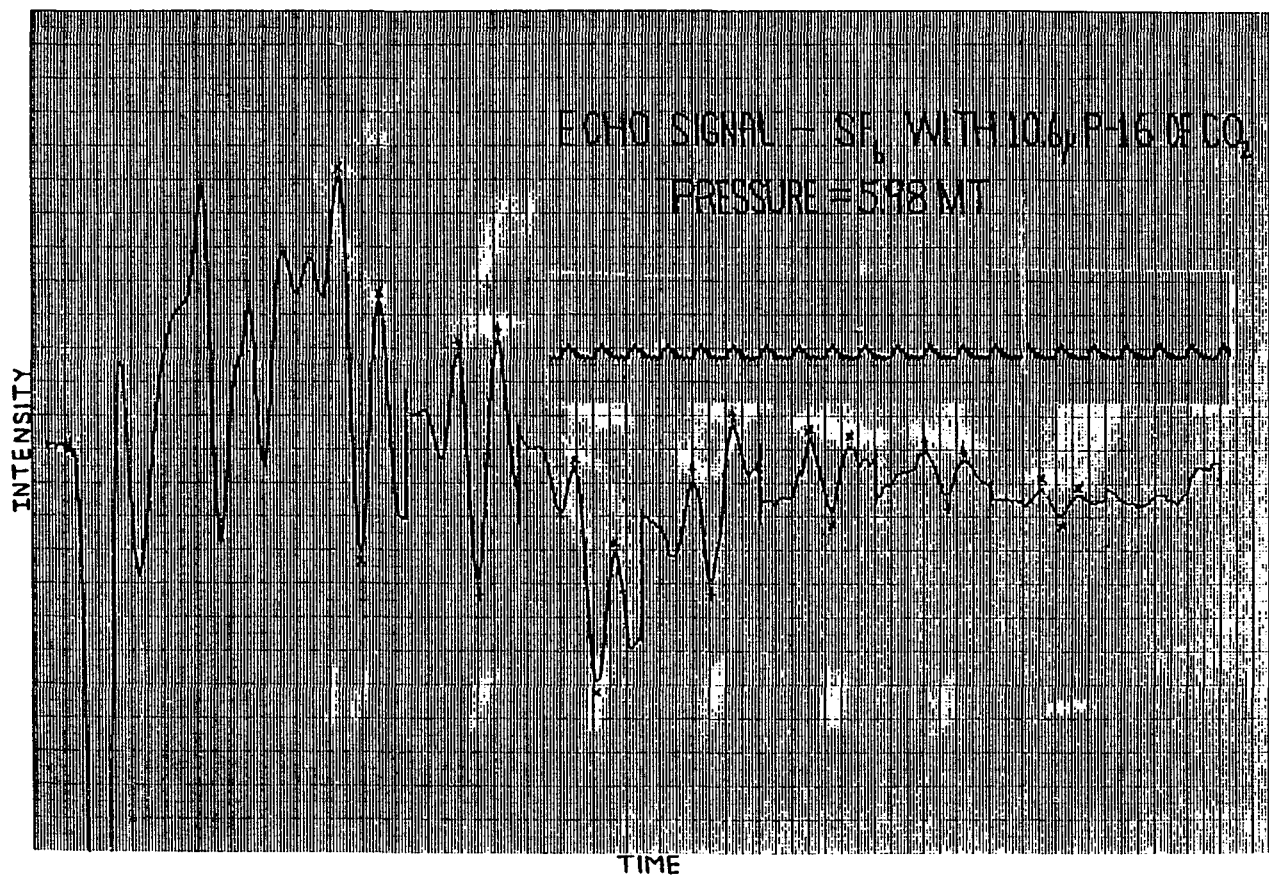


Figure 5.1. The x-y plotter output for one pressure of early raw data on photon echo experiments in SF₆.

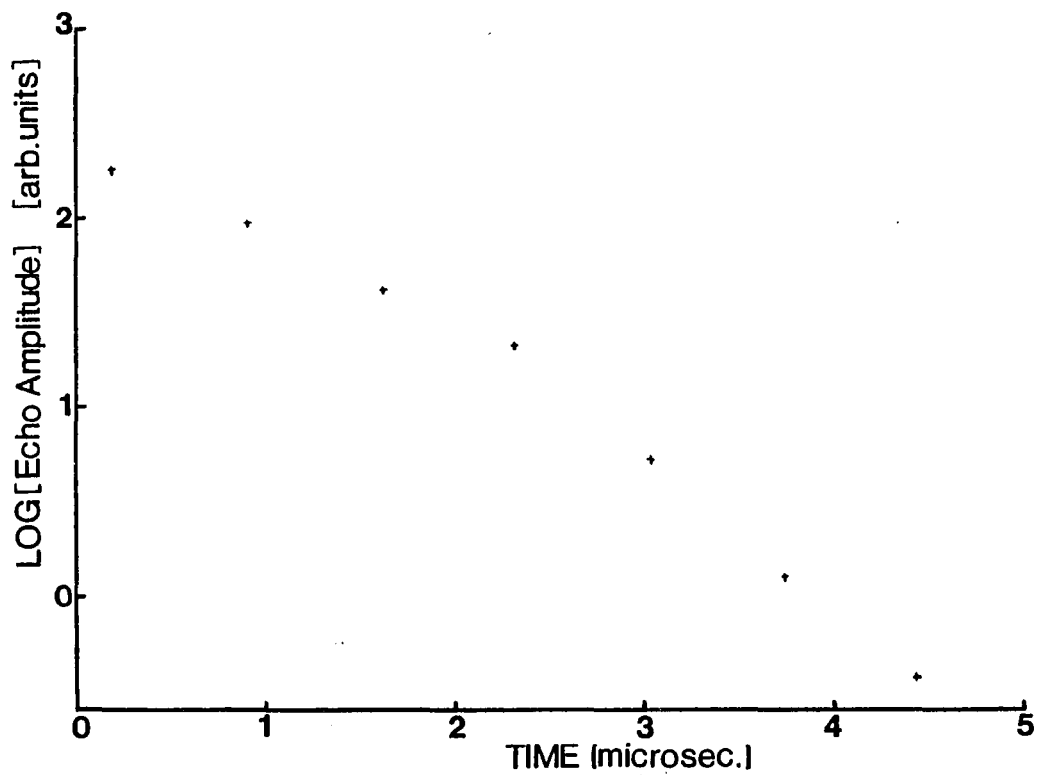


Figure 5.2. A plot for one pressure of early reduced data on photo echo experiments in SF_6 .

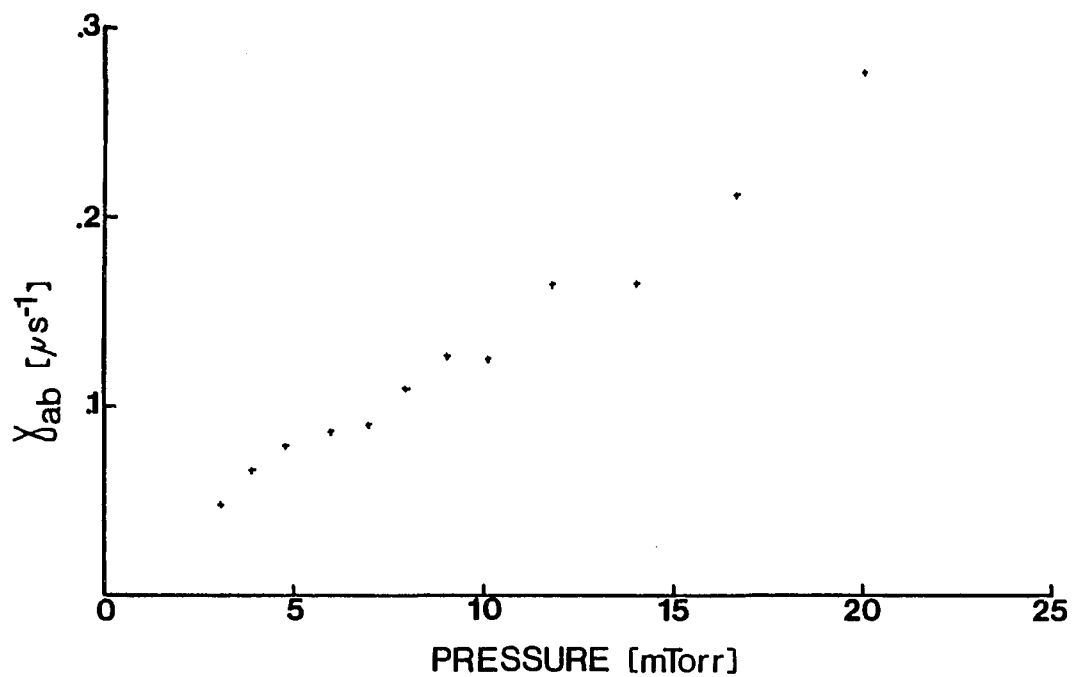


Figure 5.3. A plot of the slopes from linear least-squares best fits to the early data versus pressure.

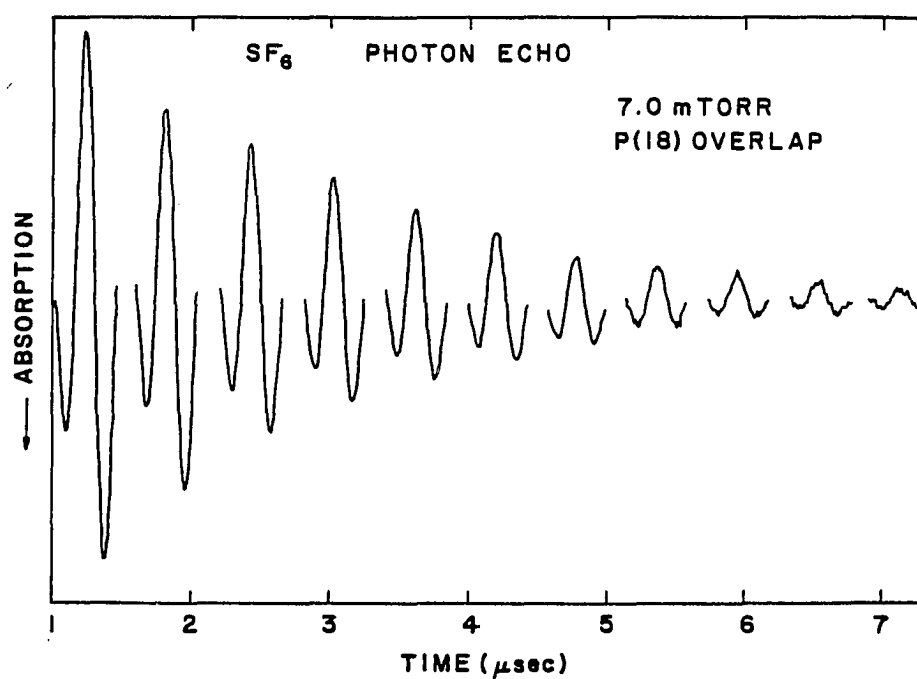


Figure 5.4. A photon echo train taken after the computer based data acquisition system was completed.

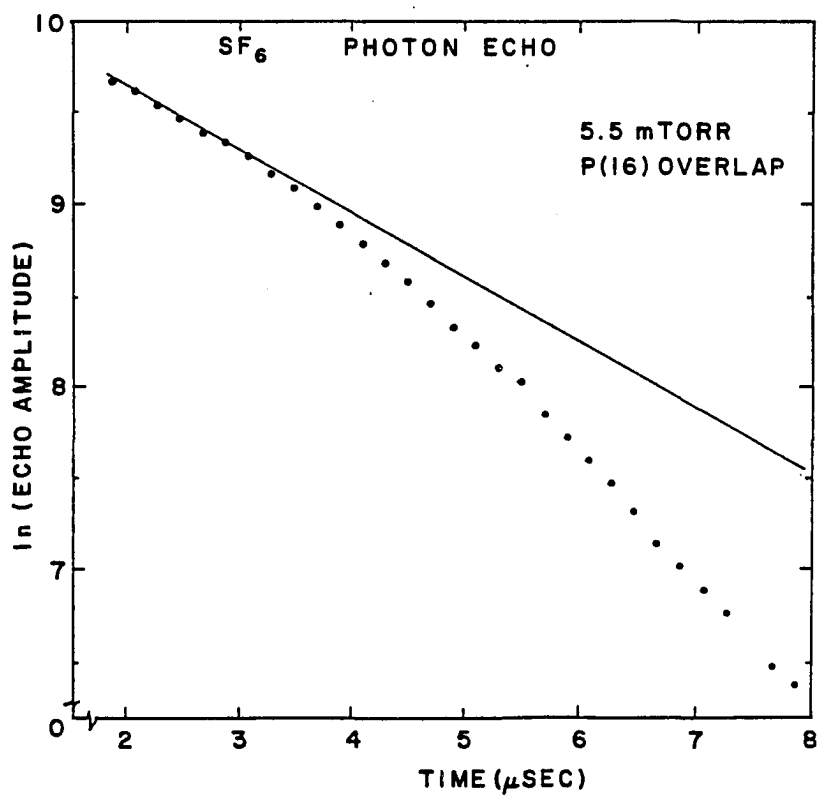


Figure 5.5. A plot of the reduced data for one pressure clearly indicating a non-exponential decay.

shape of the decay curves are very similar to the curves observed by Berman et al. (Berman et al., 1974) in their study of photon echoes in $C^{13}H_3F$. They have explained the shape of the decay curves in terms of a weak velocity changing collision model. In the laboratory frame, a velocity change appears to be a frequency change in the molecules' resonant frequency. With small enough velocity changes the coherence of the gas system is not affected initially but is destroyed non-ergotically in time via a dephasing from the frequency spread. For very large separations, each dephasing is complete so that VC collisions act like another molecule removal channel and contributes just a simple exponential decay factor to the decay. Intermediate times have a complicated dependence to connect the slow and fast decay limits.

The SF₆ Data Runs

In anticipation of fitting to the analytical expression derived by Berman et al., a sequence of echo experiments were taken over a pulse separation range of 1 to 4 μ s for a total of 33 echoes. To resolve the collision dependent (therefore pressure dependent) components to the decay, the sequence was repeated in 1/2 mtorr steps from .5 to 15 mtorr. The laser power was .195 watt and the collimated Gaussian beam spot size was 3.9 mm. A sequence of delayed nutation experiments were also performed as the T_1 information aids in the fitting of the echo data and indicates whether the VC model is applicable. The pulse-two delay was varied over a range of 7 μ s for a total of 16 nutation peaks. Again, the sequence was repeated over a pressure range similar to the echo

experiments (see Figure 5.6). The laser power was .39 watt and the beam size the same as before.

The Reduction of the Nutation Data

For each pressure, the nutation amplitude data was fit to equation (2.36) via a least squares routine. Over the time interval studied, the data indicates a simple exponential decay in the population difference $(\gamma_a - \gamma_b)$ for each pressure. Figure 5.7 shows this by plotting $\text{Log}(\text{calculated amplitude asymptote for large } t \text{ minus amplitude at } t') = \text{constant} + \log(\exp(-\gamma_a t') + \exp(-\gamma_b t'))$ versus t' . The time variation is seen to be linear. The slope of this line should be the total population decay rate at the indicated pressure. A plot of this signal against pressure is shown in Figure 5.8. The near zero intercept and the straight line nature of the data with pressure indicate that molecular transit time effects were negligible and that the population decay channels were totally dominated by collisions. The slope of this line gives the population decay rate $\gamma_a = \gamma_b = \Gamma_1 = (.032 \pm .003)P\mu\text{s}^{-1}$ where the pressure, P , is in mtorr.

The Theory of Weak Velocity-Changing Collisions

The fact that $\gamma_a = \gamma_b$ over the duration of the experiment suggests the sort of model that can be used in dealing with the echo decay behavior. The induced dipole can decay due to population decay effects (T_1), such as state changing collisions and molecular drift through the beam, and can decay through phase interrupting collisions and/or velocity changing collisions. A phase interrupting collision

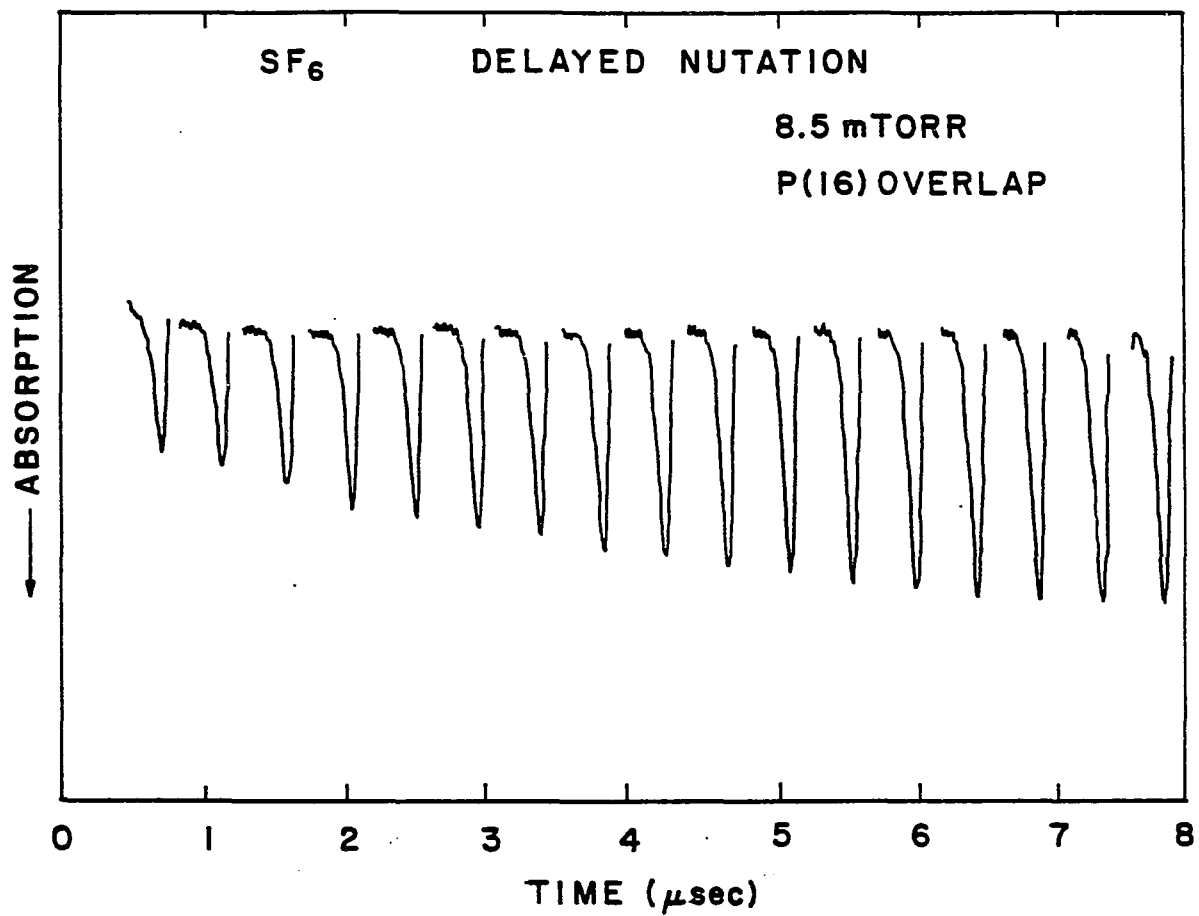


Figure 5.6. A typical set of delayed-nutations taken at one pressure for different delays.

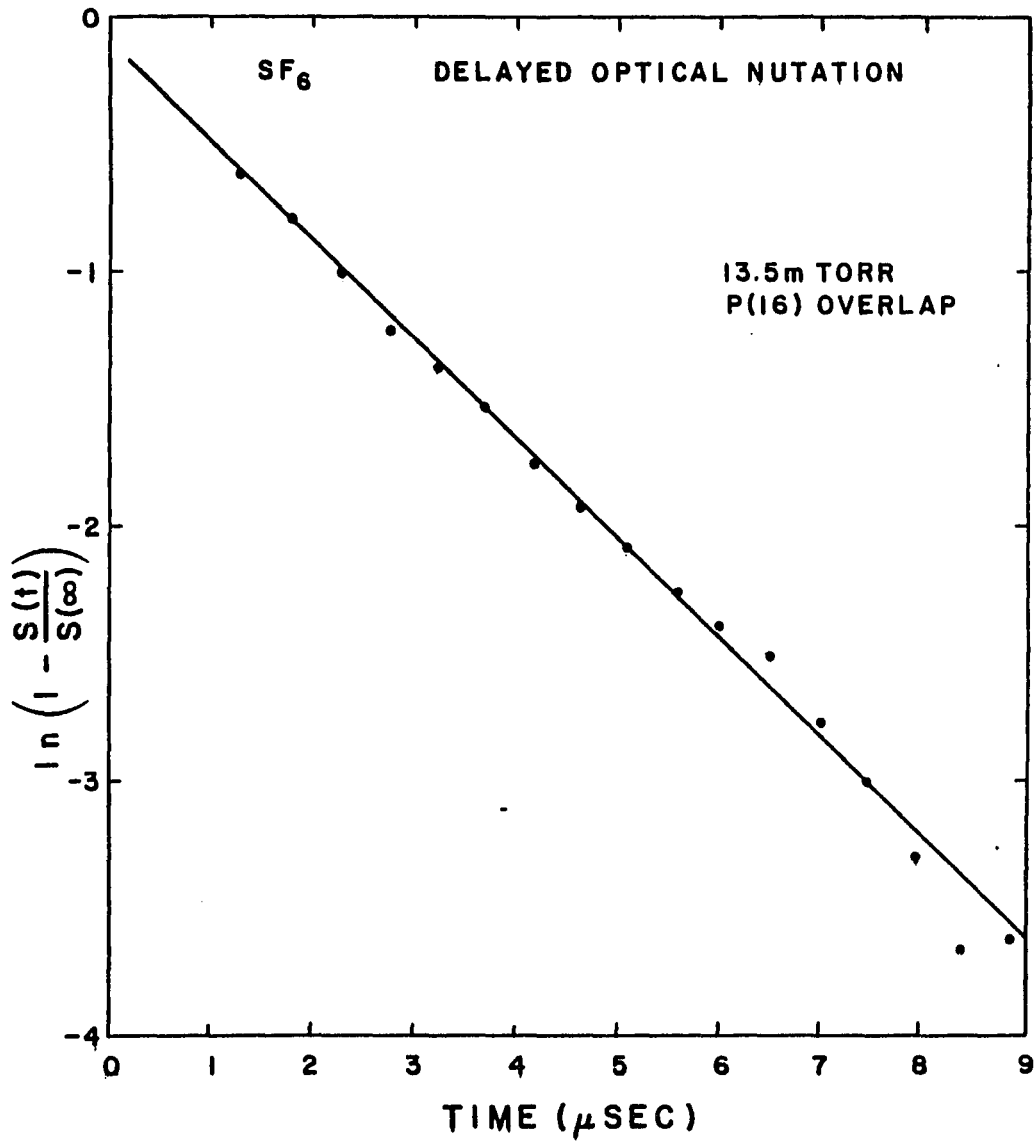


Figure 5.7. A typical plot for one pressure of reduced delayed nutation data indicating a simple exponential delay.

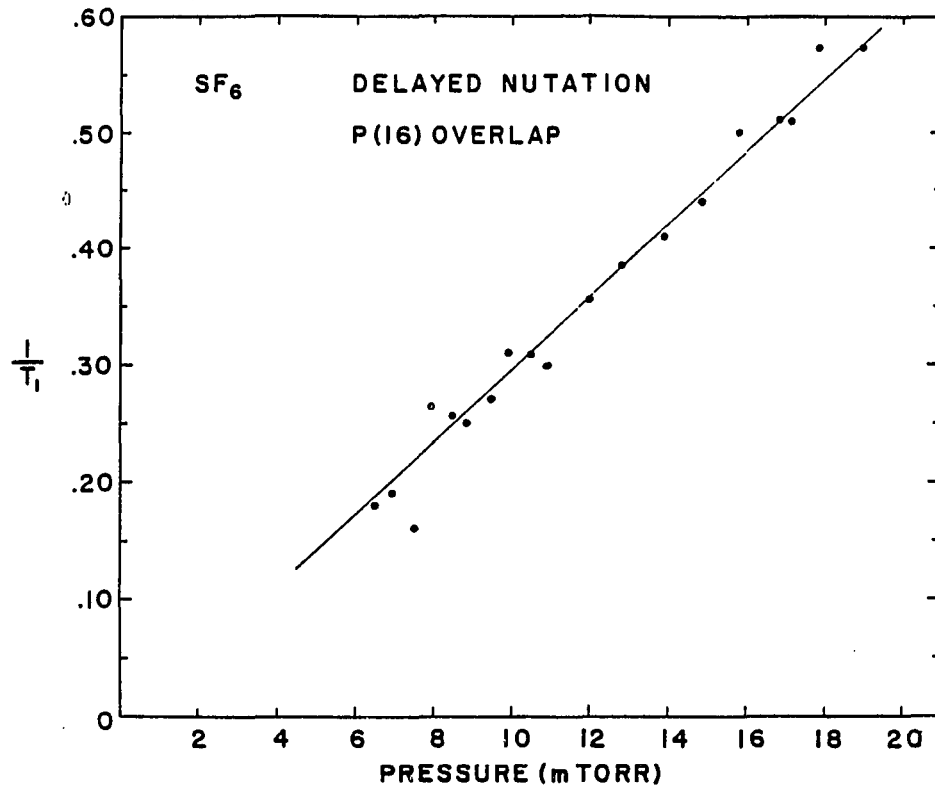


Figure 5.8. A plot of the simple exponential decay rate obtained for each pressure studied by delayed nutation versus pressure.

can be viewed as due to a frequency shift of the dipole over the duration of the collision due to the differential perturbation of the a and b energy levels by the collision interaction. The nutation results suggest that the a and b level interactions with nonabsorbers on collision are identical. One expects, then, that there would be no phase interrupting collisional effects in the echo experiment.

Furthermore, we should be able to model velocity changing collisions in a manner where molecular trajectories are treated classically. Generally this is not the case as a mixed state involved in a collision demands a quantum mechanical solution. Since here the collisional interactions appear to be the same for the two levels, this problem does not arise.

The VC collision decay theory of Berman et al. assumes classical trajectories and takes the velocity changes upon collision to be very small compared to thermal velocities. We note that the VC contribution to the population matrix is of the form

$$\left(\frac{\partial}{\partial t} \rho_{ij}(V_z)\right)_{vc} = \int_{-\infty}^{\infty} w(V'_z \rightarrow V_z) \rho_{ij}(z_1 V'_z, t) dv'_z - \Gamma_{vc} \rho_{ij}(V_z) \quad (5.1)$$

where

$$\Gamma_{vc} = \int_{-\infty}^{\infty} w(v_z \rightarrow v'_z) dv'_z \equiv \text{the total probability of a VC collision}$$

out of velocity group V_z , and where $w(c \rightarrow d)$ is the probability density of going from velocity component c to d. The above theory's assumptions above VC collision a consistency with the trajectory behavior of the molecules being described with a Brownian motion model. Berman et al. did this by using the Brownian motion kernel of Keilson and Stover (Keilson and Stover, 1952).

The Keilson-Stover kernel is based on the choice

$$w(v'_z \rightarrow v_z) = w(v_z - \alpha v'_z) \quad (5.2)$$

where α is close to but less than one. This choice assumes that W is independent of the initial velocity, that the molecule is more likely to be slowed down than speeded up, and that collisions are weak. With no further assumptions, a narrow Gaussian probability density function centered at $\alpha v'_z$, with the width equal to about the mean velocity change can be derived. Applying this result to the equations of motion (2.13) with (5.1) added, one finds (Berman et al., 1974)

$$S(\text{peak}) \propto \exp[-\gamma_{ab}(2t) - \Gamma_{vc}(2t)] + \frac{4\Gamma_{vc}}{K\Delta u} \int_0^{\frac{K\Delta u 2t}{4}} \frac{K\Delta u 2\tau}{4} e^{-n^2} dn \quad (5.3)$$

where t is the separation between pulse-one and pulse-two and Δu is $\sqrt{2}$ times the rms velocity change-collision. The kernel appears only in the integral so its details are not important. In this model Γ_{vc} is directly proportional to pressure, while for fixed temperatures, Δu is a constant. For suitably small Δv and Γ_{vc} , VC effect should not be evident in delayed nutation experiments. Physically this is due to the small size of the net frequency detuning produced by VC collisions over the time of the experiment, compared to the width of the hole burned in the velocity distribution by the transient pulse ($K\Delta u \Gamma_{vc} T \ll \tilde{\nu} E_0$, where $T \equiv$ experiment duration). In other words, the VC effects do not register in the nutation signal because they are too small to significantly fill the hole burned by the laser.

Echo Data and Results

In Berman et al.'s experiment and in the only other experiment to report VC effects, also a Stark experiment (Van Stryland, 1976), only the asymptotic behavior of equation 5.3 was used in analyzing the data:

$$\text{for } K\Delta v 2t \ll 1: \quad \text{Log } S(\text{peak}) \approx C1 - \gamma_{ab} 2t - \frac{1}{48} \Gamma_{vc} (K\Delta u)^2 (2t)^3 \quad (5.4)$$

$$\text{for } K\Delta v 2t \gg 1: \quad \text{Log } S(\text{peak}) \approx C2 - (\gamma_{ab} + \Gamma_{vc}) 2t \quad (5.5)$$

where C1 and C2 are time independent terms. Clearly, more information is needed to resolve all of the parameters. One might assume $\gamma_{ab} = \Gamma_1$, or under certain circumstances one might justify using Carr-Purcell experiments to measure γ_{ab} (Van Stryland, 1976; Berman et al., 1974; and Shoemaker, 1878). The method is still limited to the extent that only the asymptotic regions are probed. Previously the short time applicability of the data was justified by plotting the log of the short time data plus $\gamma_{ab} \cdot 2\tau$ (obtained by Carr-Purcell) versus $(2t)^3$. For short time it was observed that one obtained a nearly straight line dependence indicating the time region of equation (5.4) applied. The long time regime was found by plotting log (data) versus time and looking for a straight line at the longer times.

In the SF₆ data, it appears unlikely that we have enough data points in the long time regime. For short time (the first 10 points) and for each pressure, a least squares best fit of log(data) has been made to

$$A - B \cdot 2t - C \cdot (2\tau)^3: \quad A, B, C \text{ constants} \quad (5.6)$$

The results are plotted against pressure and shown in Figures 5.9 and 5.10. We find that $\gamma_{ab} = .039 \mu s^{-1} \cdot P$ and $\Gamma_{vc} k^2 \Delta u^2 = (.24 + .0074 \cdot P) \mu s^{-3}$ where P is in mtorr. This early delay time data has been plotted in the manner described above versus $(2t)^3$ and shows a seemingly reasonable straight line region (see Figure 5.11). Unfortunately it has been found that this test is suspect. Manufactured data using a t^2 dependence rather than t^3 also gives an apparently straight line region on the above plot. Fitting the actual data to the expression

$$A - B(2t) - C(2t)^2 \quad (5.7)$$

also gives results similar to Figure 5.11. Essentially, any gentle curve plotted on the stretched out $(2t)^3$ axis appears to give a straight line region for short t. Thus, it can not be said with any certainty that even the earliest data points obtained are in the short time regime of equation (5.3). The value of γ_{ab} obtained above may be due to more than the actual non-VC contributions. The value found must be taken as an upper limit to the real number. The nutation experiment gives the lower limit, $\gamma_{ab} = \Gamma_1$, since population decays always destroy the dipole. Thus, we have γ_{ab} bracketed between $.032P$ and $.039P \mu s^{-1}$.

To obtain values for Γ_{vc} and Δu and to resolve γ_{ab} better, a least squares fit has been done for $\log(\text{data} + \gamma_{ab} P_{2t})$ against

$$F \cdot 1 - G \cdot 2\tau + H \cdot \left(\int_0^{K\Delta u 2t/4} e^{-n^2} dn \right) \quad (5.8)$$

where F, G, and H were constants to be fit and where Δv is varied for each pressure run to give the best least-square error. The γ_{ab} term is varied over the above indicated range and the fit repeated.

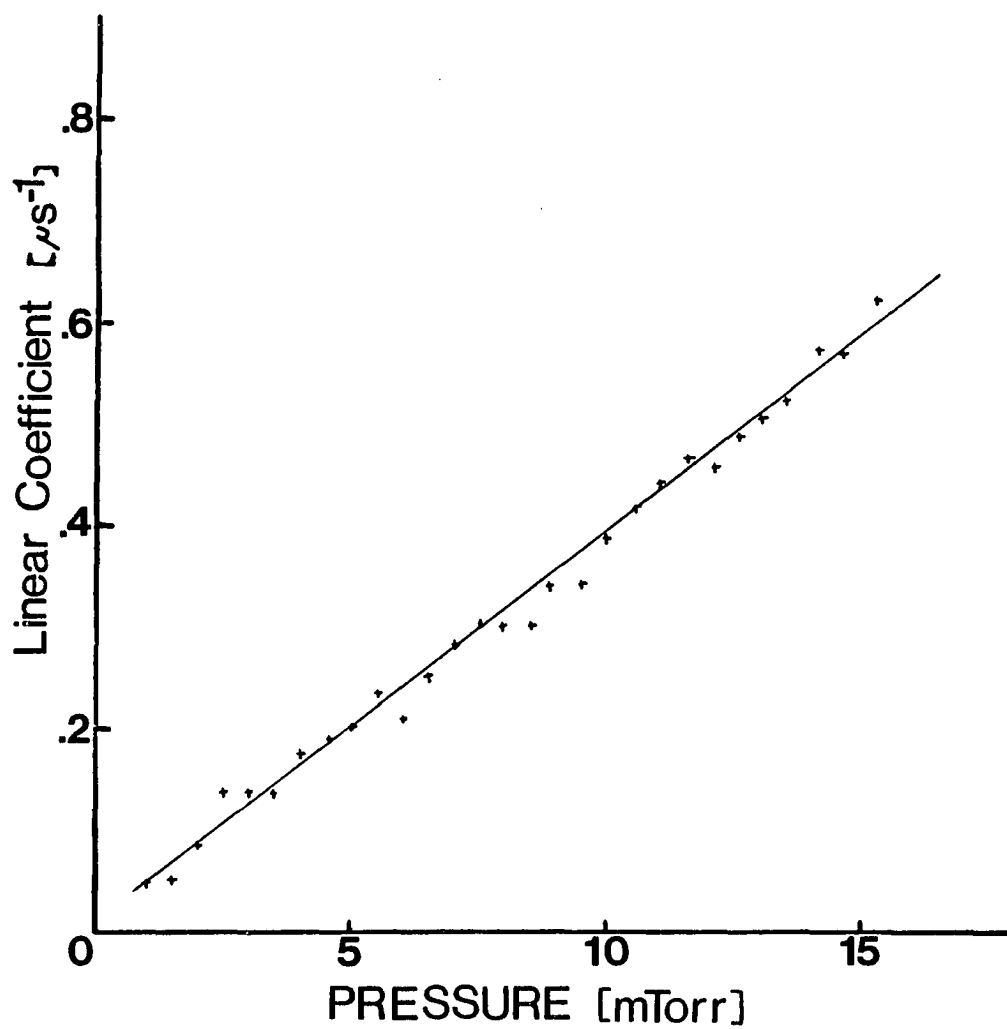


Figure 5.9. A plot of the linear coefficient from the best fit of eq. 5.4 to the first 10 points of each pressure run of the echo experiments versus pressure.

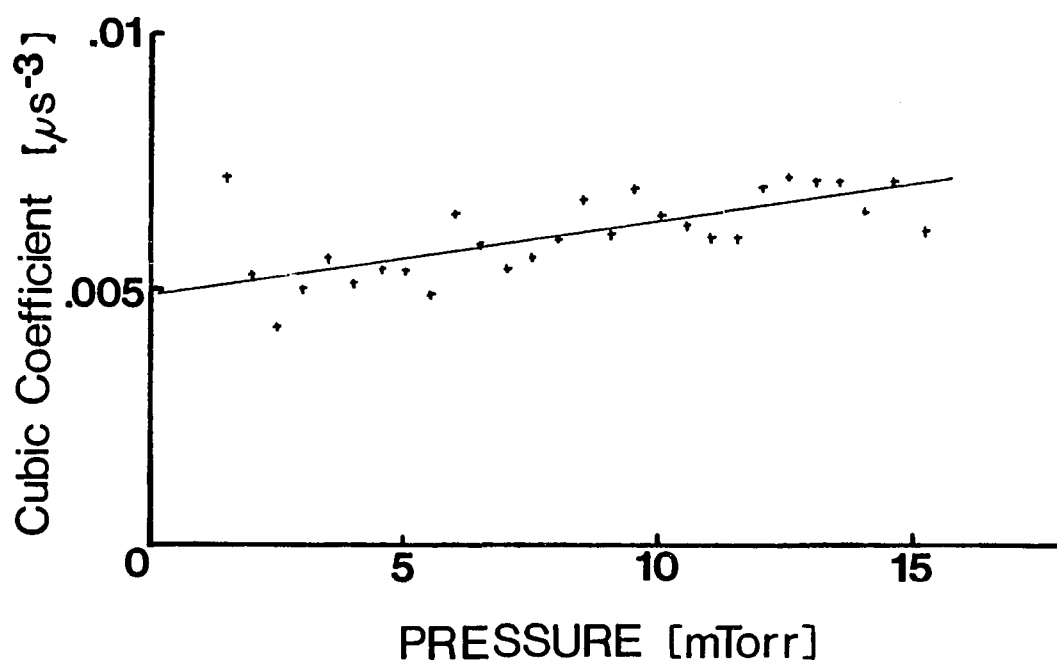


Figure 5.10. A plot of the cubic coefficient from the best fit of eq. 5.4 to the first 10 points of each pressure run of the echo experiments versus pressure.

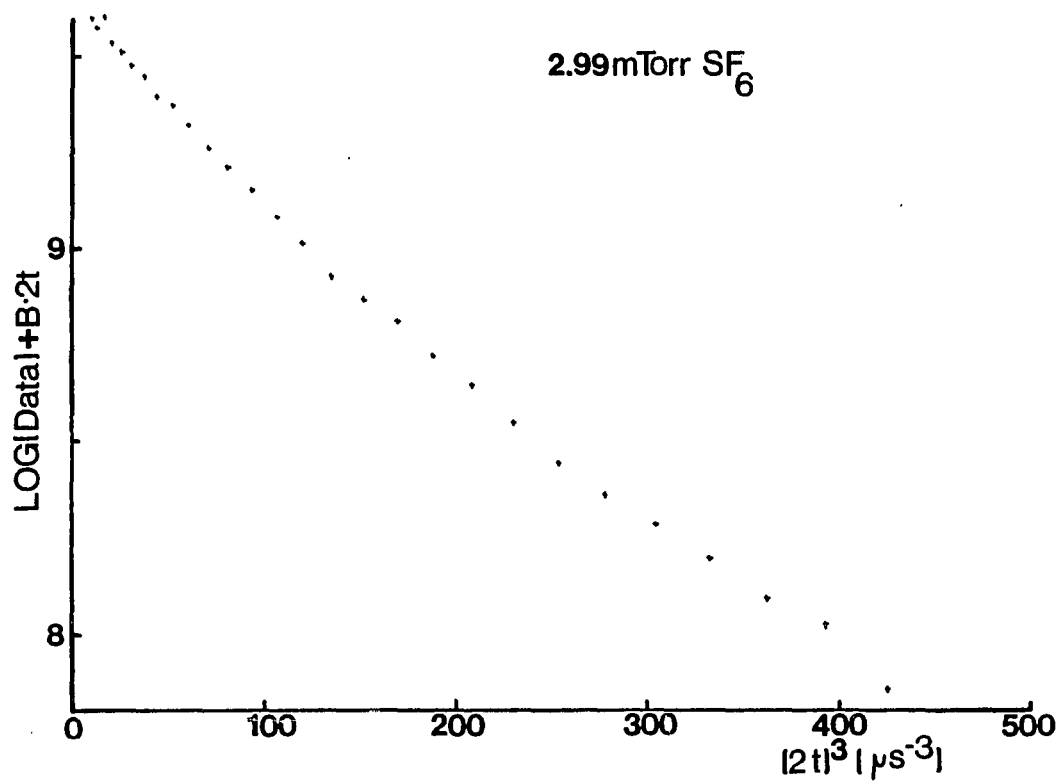


Figure 5.11. A representative plot of one pressure run of the echo experiment to show the apparent t^3 behavior for short delay times.

It has been found that the fit is not too sensitive to small changes in γ_{ab} . Nonetheless, by comparing the least square errors for all the pressures, the range in γ_{ab} has been reduced in between .032P and .034P μs^{-1} . An example of the fit is shown in Figure 5.12 for one pressure. Thus, to experimental accuracy, $\gamma_{ab} = \Gamma_1$, in agreement with our earlier intuitive expectations. Though Δu is allowed to vary for each pressure, the closest fits are localized over most of the observed pressure range. For the highest pressures the Δu scatter became significant but this is not surprising as the gentle VC curve is being hidden in the rapid decay slopes. The best fit Δu is $155 \pm$ cm/sec (see Figure 5.13). Γ_{vc} versus pressure fits a straight line giving $\Gamma_{vc} = (.46 \pm .01 + (.017 \pm .001)P)\mu\text{s}^{-1}$ (see Figure 5.14). The linear pressure dependence is as expected while the constant term does not fit the model. It is however, not a surprise to find this intercept as it has also been observed in all previous echo experiments. This constant term has been found to be a beam intensity dependent term. It approaches zero as the intensity is reduced while the pressure dependent terms remain unchanged (Berman et al., 1974). We can also note that the value of the parameters found justify the assumption that VC effects are not important in nutation experiments ($K\Delta\nu\Gamma_{vc}T \leq .2\text{MHz} \ll 10\text{MHz}$).

It is instructive to display our results in terms of collision cross sections and to compare them to the results of NH_3 and CH_3F . The cross section is defined using $\Gamma = Nv_r\sigma$ where Γ is the decay rate of interest, σ is the cross section, N is the number density, and $v_r = (8kT/\pi\mu)^{1/2}$ is the mean relative speed of the molecules. For a

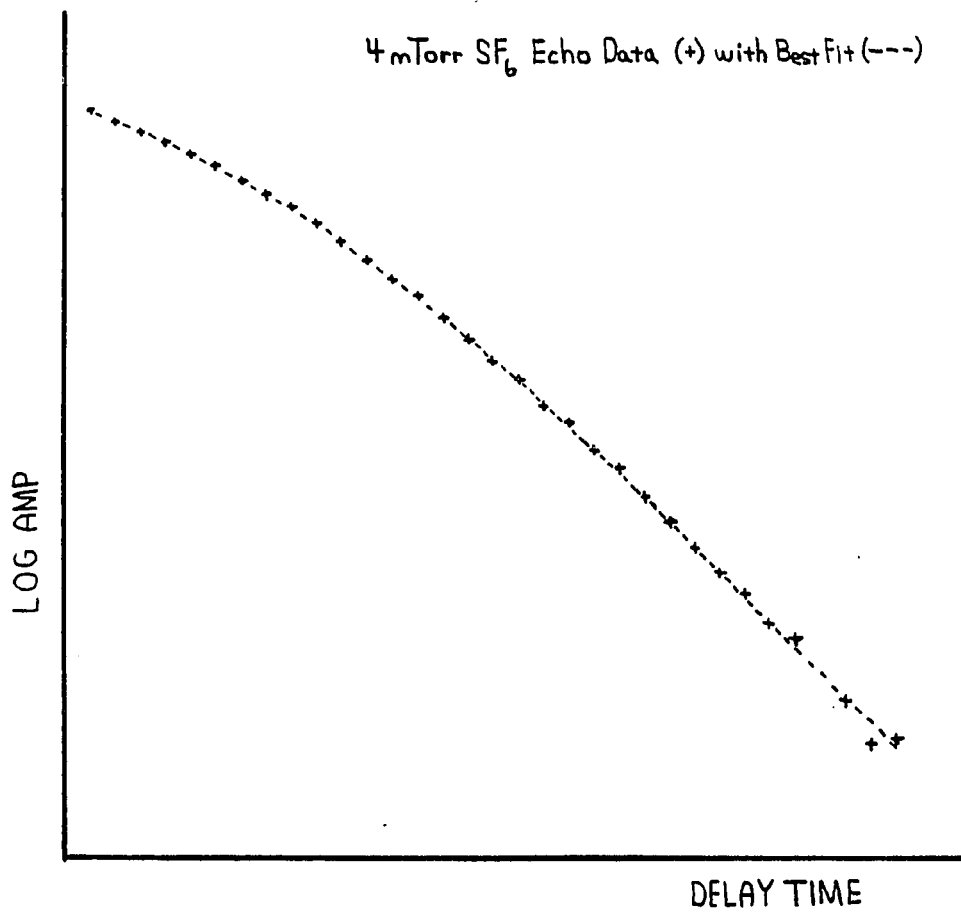


Figure 5.12. A plot of one pressure run of the echo experiment and the least-squares best fit of eq. 5.8 to it.

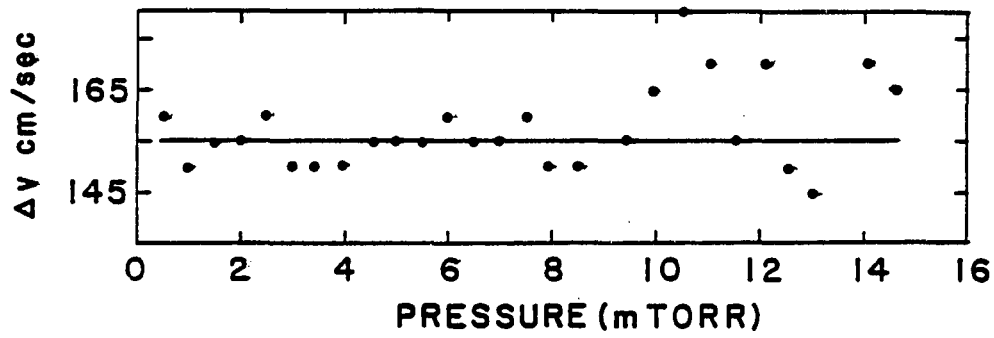


Figure 5.13. A plot of the Δv parameter obtained for each pressure by least-squares best fitting eq. 5.8 versus pressure.

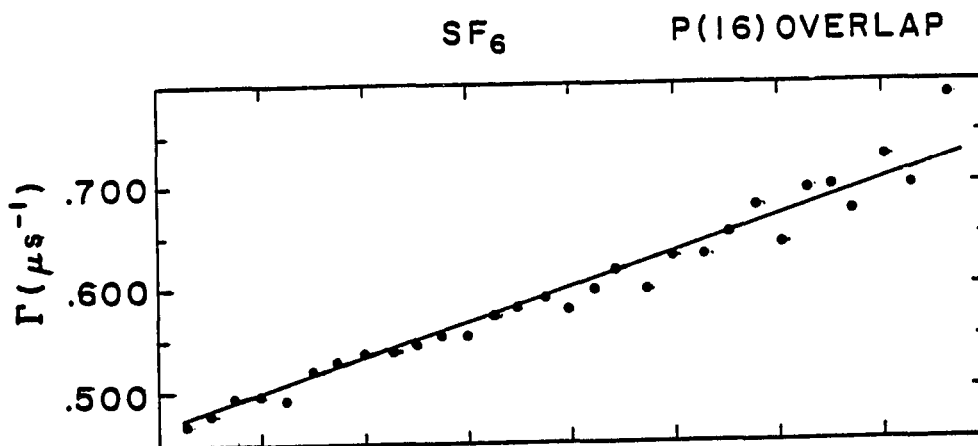


Figure 5.14. A plot of the Γ_{vc} parameter obtained for each pressure by least-squares best fitting eq. 5.8 versus pressure.

pure gas, the reduced mass μ is just the molecular mass divided by 2. The obtained results for our SF₆ line are listed in Table 5-1. Here \bar{u} is the most probable speed. The cross section for velocity changing collisions, σ_{vc} , is quite large, of the same order of magnitude as σ_{pop} , the cross section corresponding to the level decay rate. The average change in velocity is very small, however less than 1% of thermal. This justifies our use of a weak collision model. Table 5-1 also lists the obtained results for the polar molecules ¹³CH₃F (Berman et al., 1974) and ¹⁴NH₂D (Van Stryland, 1976).

Table 5-1 Comparison of measurements for ¹³CH₃F, ¹⁴NH₂D, and SF₆

¹³ CH ₃ F	¹⁴ NH ₂ D	SF ₆
$\delta_{vc} = 180 \text{ \AA}^2$	530 \AA^2	$= 180 \text{ \AA}^2$
$\sigma_{pop} = 440 \text{ \AA}^2$	570 \AA^2	$= 335 \text{ \AA}^2$
$\Delta v = 85 \text{ cm/sec}$	340 cm/sec	155 cm/sec
$\Delta v/\bar{u} = .0022$	$.0042$	$= .0084$

Note that because the CH₃F-CH₃F and NH₂D-NH₂D collisions are dominated by the long range dipole-dipole interaction, the cross sections are larger, particularly for Γ_{vc} . We can see also that $\frac{\Delta v}{\bar{u}}$ is much smaller in the polar molecules than is SF₆. This is to be expected since the shorter range intermolecular forces in SF₆ tend to make it look more like a "hard sphere" than the polar molecules.

Conclusions and Discussion

One can conclude from the above results that the frequency-switched system is indeed a sensitive tool in resolving the details of collisional decay in molecular systems. Using the hundreds of isotopic CO_2 laser lines available, one could investigate many polar and nonpolar molecular transition overlaps. At this point the system appears to have the potential to resolve more detail than the available theories. Further studies need be pursued to understand the physics of the intensity dependent dephasing. The pulsed experiments give no indication of this effect, consistent with the belief that the effect is related to the existence of the off-resonant beam. Since the intensity dephasing appears in Γ_{vc} , not γ_{ab} and since numerical simulations using the driving equations give no such effect, it may be that the effect is buried in the behavior of the velocity distribution and the kernel, w . Further, a detailed investigation of the assumption of the kernels independence of v'_z can easily be done with this system by varying the switching amplitude. Running experiments where the resonant gas is diluted in another nonresonant molecular gas can give information on inter-species interaction cross sections and test molecular interaction models. In particular SF_6 - noble gas mixes can be studied where the mean momentum of the nonabsorber can be varied by changing the particular noble gas used. As there are no complicating resonances in the noble gas to worry about, the observed changes in the VC parameters should lend themselves to reasonably easy interpretation. Finally, another rather different sort of experiment is naturally suited to the frequency

switched system. Due to the relative freedom of beam size choice and absorption cell length, a careful study of molecular transit effects can be made. By use of an easily constructed long absorption cell a very dilute, well known gas transition (.01 mtorr) could be studied via transient experiments with varying laser beam spot diameters. For the first time one could experimentally determine the actual detailed shape of molecular transit effects which have been assumed to be simple exponential decays in all previous transient experiments.

The frequency-switched laser opens a wider class of molecules to study and should bring a more detailed understanding and refinement of weak molecular interaction models and coherent optical transient studies.

CHAPTER 6

DELAYED NUTATION WITH ADIABATIC RAPID PASSAGE SYSTEM PREPARATION

Motivation

This chapter deals with delayed nutation experiments via the Stark effect where system preparation is accomplished using ARP techniques within the Doppler width of the subject gas. These nutation results are compared to the results from the more conventional two-pulse delayed nutation (Shoemaker, 1978) experiments done concurrently and from previous results obtained by Eric Van Stryland (Van Stryland, 1976).

As discussed in Chapter 2, ARP excitation produces a simpler prepared state for nutation experiments. We should be able to invert all the velocity groups that contribute to the nutation signal. Thus we can observe emission as well as absorption nutation peaks. Hence, given the greater average departure from equilibrium for ARP experiments, one would expect a higher resolution of decays than in the two-pulse experiments. The fact that this method is simply different makes it interesting as a comparison to the pulsed excitation experiments.

Optical ARP Background

ARP techniques have been used in NMR since 1961 (Abragam, 1961). The first application to the optical region was attempted to 1969 with the frequency-chirped output of a Q-switched CO₂ laser (Treacy and DeMaria, 1969). No quantitative measurements were made and doubts as to whether ARP was observed have arisen due to laser spectroscopic

studies of the transitions. The first quantitative experiments in the optical were done in 1974 (Loy, 1974). In this experiment, a high power wide-pulse CO_2 laser and Stark tuning techniques were applied to the 10.6 μm $\text{R}6$ CO_2 overlap with N^{14}H_3 (ν_2 , $s \rightarrow a; Q(J=s, K=s)$). The full Doppler width of the gas was inverted using a linear frequency chirp of the resonance produced by a linear voltage ramp added to the large DC tuning voltage on the Stark plates. A variably delayed return ARP ramp was used to probe the previously induced inversion. This clever experiment suffered from some disadvantages. Since large Stark tuning sweeps were needed, the Stark plates were spaced very closely, thus requiring narrow beam diameters. As a result, molecular transit time effects were accentuated. Furthermore, both ARP ramps had to occur within the relatively flat portion of the laser pulse, thus restricting the delay time to under $1.2\mu\text{s}$. Stark plate voltage ramps of short duration were needed to fit into the limited time interval and minimize decay effects during excitation and de-excitation. This demanded the use of high laser powers to insure adiabatic excitation conditions. These considerations led to the use of a pulsed laser system which gives only limited repeatability and reduced signal to noise.

In 1975 Lamb dip experiments were done where only a portion of the Doppler line was excited by ARP (Hamadani et al., 1975). The adiabatic inversion of population was seen as an amplification of the weak probe wave near line center. This limited frequency sweep allowed for slower frequency sweeps while still leaving the decay effects negligible. With slower frequency ramps, the power necessary to insure that the

pseudo-vector \vec{M} processes rapidly about the pseudo-force vector \vec{F} in the $\hat{u}-\hat{v}-\hat{w}$ vector representation compared to the motion of F , is greatly reduced. Thus one would not need to use a pulsed laser. However, a time resolved experiment using Loy's sequence would not work due to the contributions to the signal from the edges of the frequency sweep. These edge contributions see frequency sweeps much different from the center frequency contributions.

In the following ARP experiments the frequency sweeps were greater than twice the detector band width so that edge contributions would not be heterodyne amplified. One ARP ramp was used for system preparation but only the center velocity groups were probed with a fast voltage pulse on the Stark plates (see Figure 6.1).

The Subject Gases

Because of the large transition dipole matrix elements, high Stark tuning sensitivity, close coincidence with CO_2 laser lines and the existence of previous studies, the $(v, J, K, M): (0_a, 6, 6, +6) \rightarrow (1_s, 6, 6, +6)$ N^{14}H_3 transition resonance coincident with the $10.6\mu\text{m}$ R 18 line of the C^{13}O_2 laser (Asawg and Plant, 1977) and the $(0_a, 2, 2, +2) \rightarrow (1_s, 3, 2, +2)$ N^{15}H_3 coincidence with the $10.6\mu\text{m}$ R 40 line of the C^{12}O_2 laser line (Van Stryland, 1976) were studied. A disadvantage in the N^{14}H_3 resonance was that the power available from the C^{13}O_2 laser is less than the standard mix. However, for the above selection rules the transition strength is optimized. The N^{15}H_3 runs used the stronger C^{12}O_2 laser, however, the above selection rules do not give the strongest transition strength. $\Delta M = +1$ selection rules had to be avoided as the resonance

line structure is more complicated. With $\Delta M = \pm 1$ the Raman beat phenomenon has been observed (Van Stryland, 1976) indicating that our two-level models would not be applicable. Criteria in selecting the lines included the need for large frequency shifts for the possible applied voltage ramps, near coincidence of resonances with the available laser lines, Stark tunable under the breakdown limits of the gas, a D.C. tuning Stark splitting large enough to avoid exciting several different M_j lines, a large transition dipole matrix element to help meet the adiabatic condition, and a level structure which could reasonably be treated in a two-level manner.

The NH_3 molecule is a symmetric top molecule in the form of a pyramid with the Nitrogen atom at the apex and the Hydrogen atoms forming an equilateral triangle at the base. The normal from the apex to the base is a 3-fold symmetry axis. The vibrational transition that we are dealing with pertains to the motion of the Nitrogen atom along the symmetry axis. This motion is hindered by the repulsive potential of the Hydrogen plane. This potential is energetically greater than the four lowest order vibration modes. Hence, for these modes, the vibrational potential consists of two separate potential wells of half the original width and thus double the energy of the mode spacing. Since the potential barrier is finite, the separated lower levels communicate by tunneling. Thus, the degeneracy of the lower levels is broken. This a-s splitting of the lines which corresponds to the frequency of tunneling through the barrier is given in Table 6-1 along with other molecular parameters. This structure suggests that the ground and the

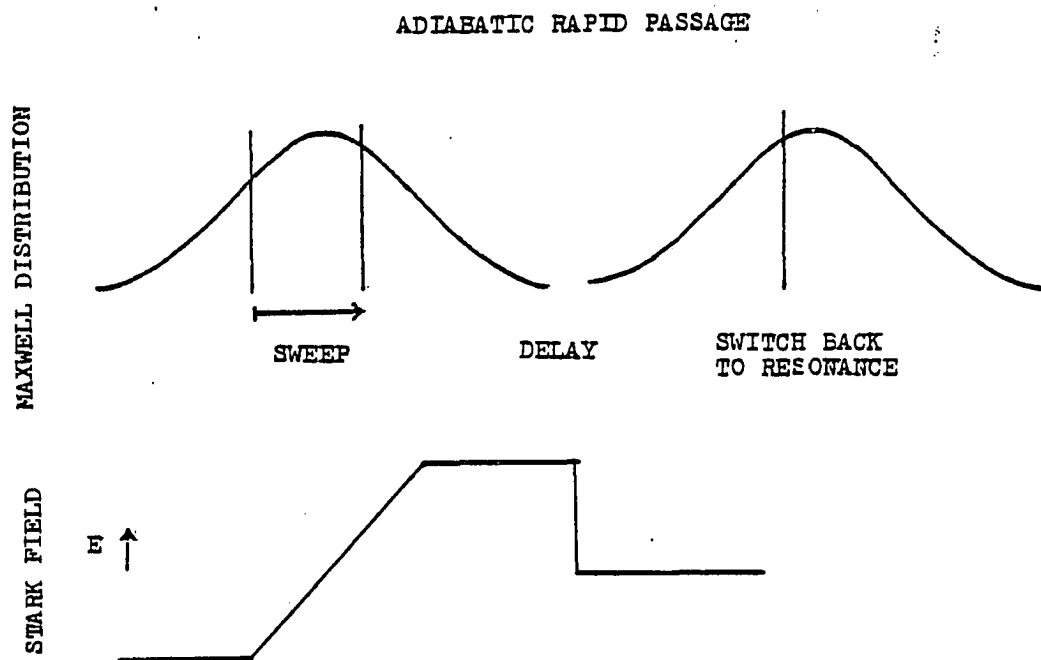


Figure 6.1. The adiabatic rapid passage sweep and pulse probe sequence studied here.

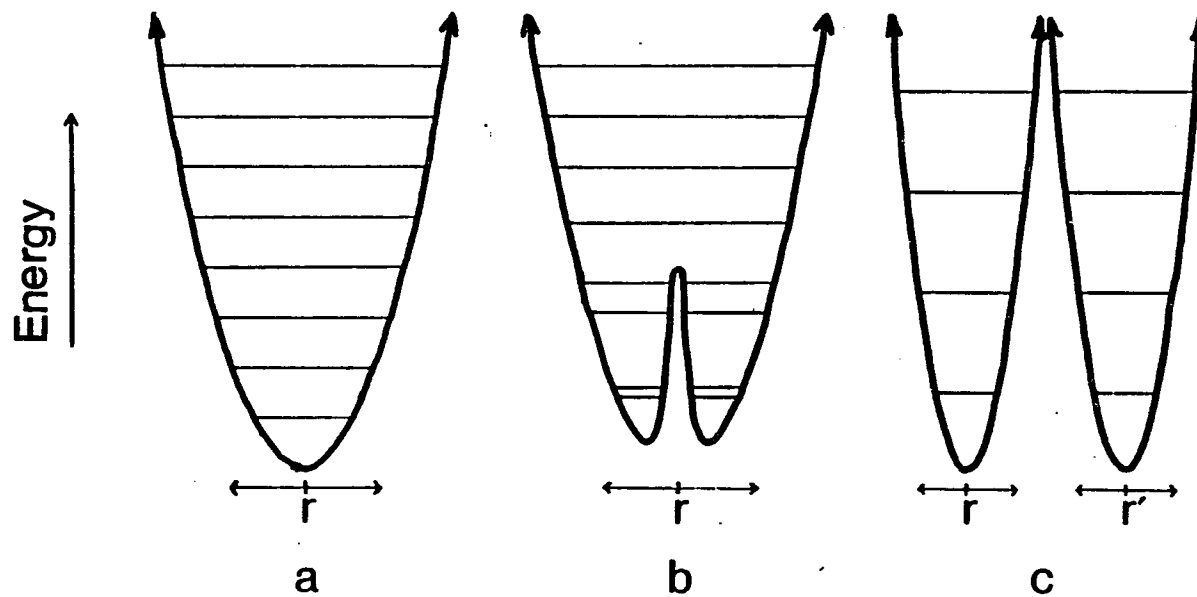


Figure 6.2. The effect of hindered motion on molecular level structure

- a) no hindered motion b) an intermediate case such as NH_3 c) the limit of an infinite potential barrier.

Table 6.1 NH₃ Parameters

$N^{15}H_3: (J,K): 2,2 \rightarrow 3,2$	$N^{14}H_3: 6,6 \rightarrow 6,6$
μ_0 : 1.48 Debye (Shimizu, 1970)	: 1.47 Debye (Townes and Schawlow, 1955)
μ_1 : 1.27 Debye (Van Stryland, 1976; Shimizu, 1970)	: 1.25 Debye (Shimizu, 1969)
$\mu\sigma_1$: .24 Debye (Shimizu, 1971)	: .24 Debye (Loy, 1974)
ν_0 : 22,707 MHz	: 25,056 MHz
ν_1 : 1,033,000 MHz	: 1,074,000 MHz
(Townes and Schawlow, 1955)	
Tuning Bias : 2700 Volts	: 2900 Volts
eqQ : 0	: -4.084 MHz (Townes and Schawlow, 1955)
$\mu_T : \frac{\sqrt{(J+1)^2 - K^2} \sqrt{(J+1)^2 - M^2}}{(J+1) \sqrt{(2J+1)} \sqrt{(2J+3)}} \mu_{0-1}$: $\frac{KM}{J(J+1)} \mu_{01}$
$\tilde{\kappa} : .21 \text{ MHz-cm/Volt } (M_j = \pm 2)$: .7 MHz-cm/Volt $(M_j = \pm 6)$

first excited levels would have different population decay times. The argument for this (Loy, 1974) is that the collision induced transitions for NH₃ should be dominated by the dipole-dipole interaction. This interaction depends on the product of the dipoles of the excited absorber and the unexcited non-absorber. The typical duration of collisional interactions is of order .1 to 1 psec. From Table 6.1 we see that the ν_0 inversion period is about 20 psec while that of the ν_1 state is about

.5 psec. Hence, for the ν_0 state the dipole would appear to be a constant throughout the interaction while for the ν_1 state, the average of its dipole through the period of the interaction would be reduced. Two further considerations that should lower the strength of the dipole-dipole interaction for ν_1 are that $\mu_1 < \mu_0$ and that collision-induced transitions are mainly between the doublets and the greater spacing of the ν_1 doublet should reduce its likelihood.

Due to the rapid inversion oscillation in which the NH_3 permanent dipole continually changes direction, there is no first order Stark effect. In terms of Stark splitting it must be considered to have a zero average dipole moment. The doublet lines are very much closer to each other than they are to any other lines in the system, so significant mixing induced by the Stark field is restricted to the doublet. For N^{15}H_3 we can solve this two-level mixing exactly (Townes and Schalow, 1955). We find that

$$\begin{aligned}\Delta W_{a_i} &= \left(\left(\frac{\nu_i}{2} \right)^2 + E^2 \mu_{ab_i}^2 \right)^{1/2} - \nu_i/2 \\ \Delta W_{b_i} &= \nu_i/2 - \left(\left(\frac{\nu_i}{2} \right)^2 + E^2 \mu_{ab_i}^2 \right)^{1/2} \\ \mu_{ab_i} &\equiv \frac{mK\mu_i}{J(J+1)} ; i = 0,1\end{aligned}\tag{6.1}$$

Using equations 6.1 and Table 6.1 gives Figure 6.3. We see that most of the Stark tuning is due to the more closely spaced ground doublet. It can be shown that small frequency shifts about the large shift due to the D.C. bias are linear in voltage upon expanding the roots in equations above. It is calculated that small shifts go as

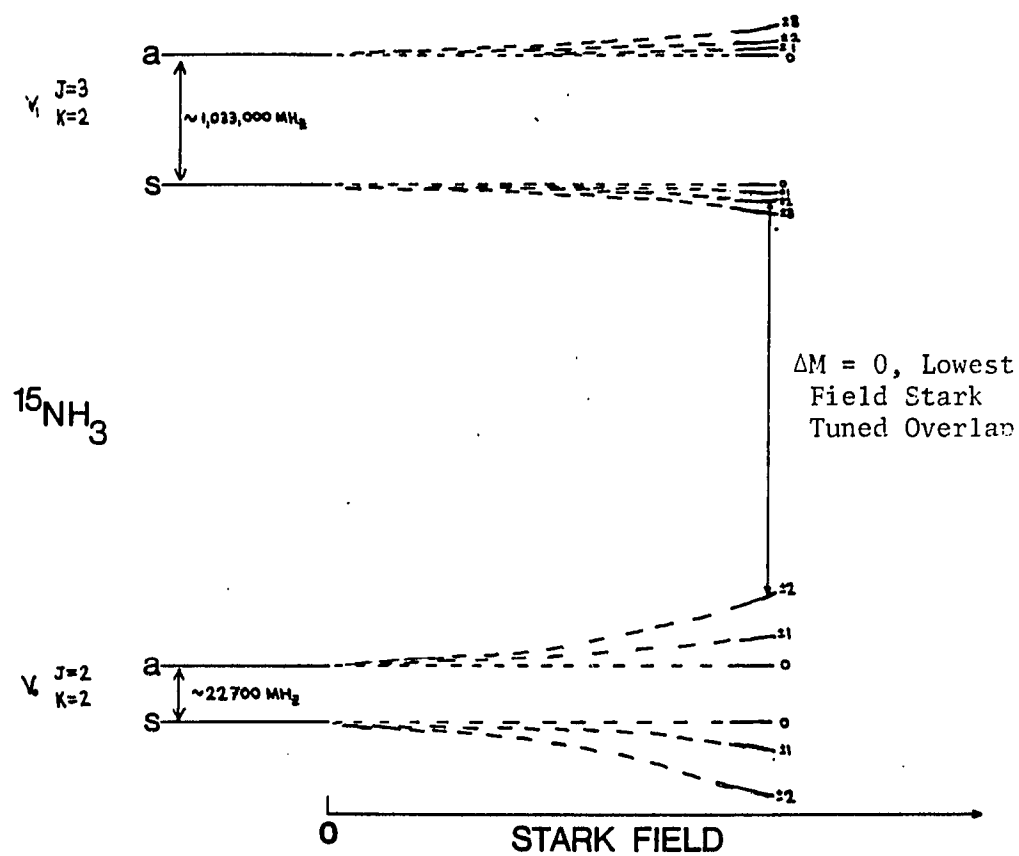


Figure 6.3. The transition studied in the $^{15}\text{H}_3$ work.

$$W/\text{volt} \approx 1.8 \text{ MHz}/\text{volt} \quad (6.2)$$

For $N^{14}H_3$, the considerations are more complicated owing to the quadrupole moment of N^{14} . In the ν_0 level the Stark effect are strong enough that the quadrupole effects may be considered as perturbations to the results in equation 5-10. The correction terms are given by (Townes and Schalow, 1955)

$$W(Q) = \frac{eqQ[\frac{3K^2}{J-+1} - 1]}{4I(2I-1)(2J-1)(2J+3)} \{3M_I^2 - I(I+1)\}(3M_J^2 - J(J+1)). \quad (6.3)$$

For the ν_1 levels the Stark and quadrupole effects can be comparable. Therefore, the secular equation is solved (Jauch, 1947). The results are illustrated in Figure 6.4 where we have used the uncoupled basis (J, K, M_j, I, M_I) and have written out just the terms containing $|6, 6, \pm 6\rangle$ contributions. From this diagram we see that for the $M_j = \pm 6$ to ± 6 transitions, the upper level is very nearly uncoupled. Assuming $\Delta M_I = 0$ as well as $\Delta M_j = 0$ selection rules gives the bulk of the transition interaction with the bottom three levels of the upper state (about 95%). These levels are only slightly distorted ($\Delta f \leq 200 \text{ kHz}$) from the ν_0 structure. This gives us a set of transitions degenerate in energy and each behaving as a two-level system. Once again the Stark tuning depends on only the lower level. Voltage shifts about the large D.C. bias are calculated to go as

$$W/\text{volt} \approx 2.95 \text{ MHz}/\text{volt} \quad (6.4)$$

Four complete ARP runs were made. Two with 100-volt ramps and two with 200-volt ramps. One of each of the voltage ranges was done on the $N^{14}H_3$ system and one on the $N^{15}H_3$ system. One 200 volt two-pulse delayed-nutation experiment was run for the sake of comparison. Two-pulse results for $N^{15}H_3$ were already available and thus not repeated.

The ARP experiments were done such that emissive nutation peaks were evident. This meant that certain trade offs were necessary. The full frequency scan range limits were pushed to allow short delay probings while the intensity was peaked to satisfy the ARP condition. In the 100 volt runs, for example, the frequency range of the sweep was below the ideal $10\tilde{\nu}E_0$ value. Table 6-2 lists the relevant parameters for each of the experiments. Equation (2.29) is used to describe the extent of the adiabatic nature of both the ramp sweep and the probe edge's frequency shift. We see that in the $N^{14}H_3$ runs, a stronger adiabatic inversion was made. This advantage was balanced by the probe step voltage being closer to the adiabatic condition than that of the $N^{15}H_3$ run. The probe voltage fall rates are nearly the same for the 200 volt and 100 volt experiments since faster switching and transitions are available for the smaller switching experiments.

In all the ARP runs, at least for the lower pressures, the probe pulse produced an emissive nutation peak at short delays which decreased for greater delay times till it became an increasingly deep absorption nutation peak. See figure 6.5. This demonstrated at least partial

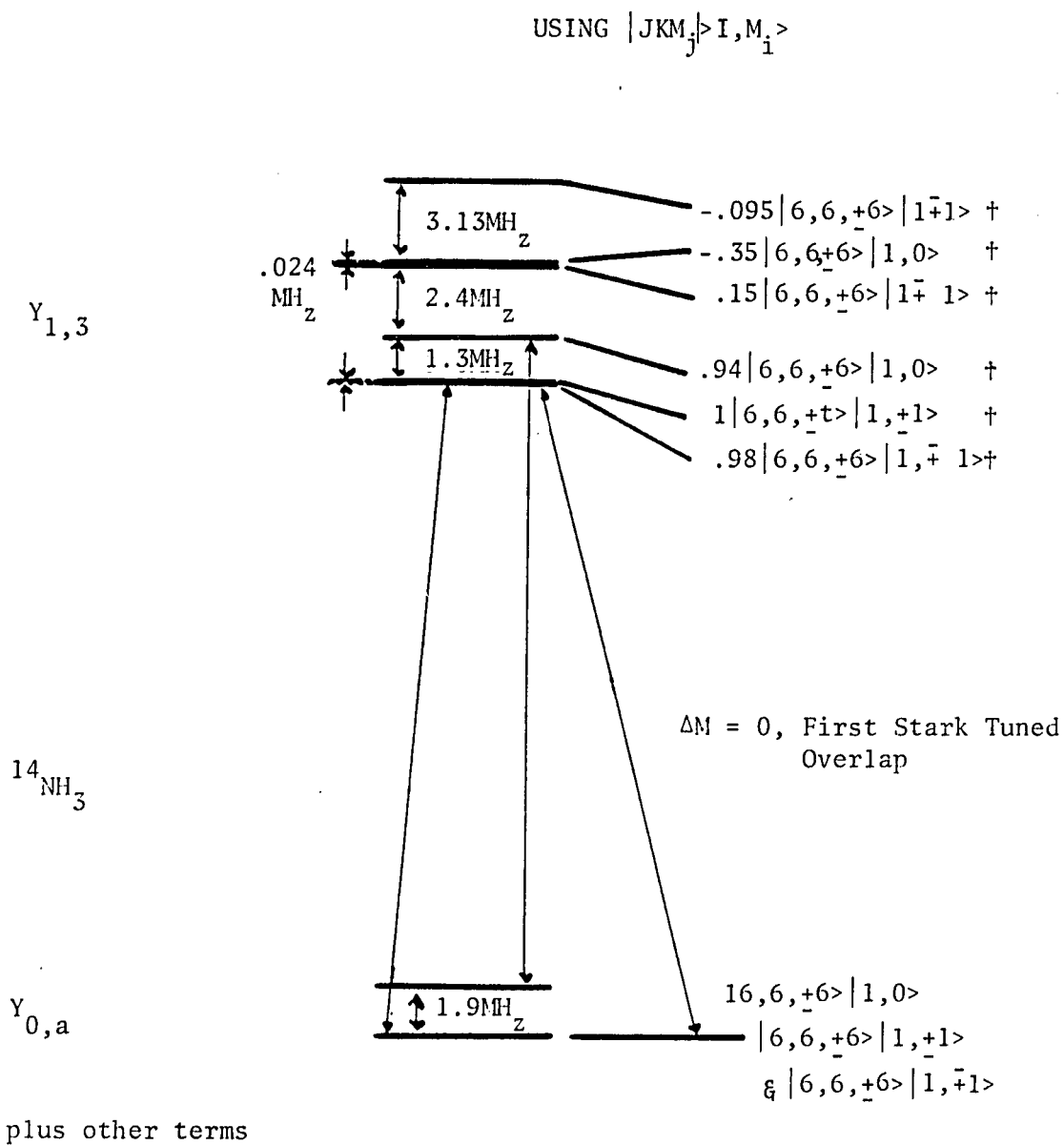


Figure 6.4. The transition studied in the N¹⁴H₃ work.

adiabatic population inversion and its decay. It should be noted that at the emission to absorption crossing point the signal is not zero. Instead one sees a small modulation which appears to phase reverse past the crossing-point. It is believed that this is due to the finite fall time of the probe step voltage.

Data Reduction and Results

Previous delayed nutation studies of NH_3 in the infra red (Loy, 1974; Van Stryland, 1976) have fit the data to simple exponentials. The decay rates obtained for each pressure have been plotted against pressure. The rationale has been that over the delay times observed, the presumably double exponential decay (equation 2.36) appears to behave like a simple decay.

Table 6.2 Experiment Parameters

Experiment	Frequency Range Swept Out (MHz)	Power (Watt)	E_0 (MHz)	E_0^2 (MHz^2)	$\frac{W_{\text{end}}}{W_{\text{start}}}$				
					R (MHz/s)	Ramp	Probe	Probe	
N^{14}H_3 ARP									
200 Volt	590	.2	38	1425	369	8400	-.91	.75	
100 Volt	295	.29	46	2114	369	7375	-.98	.60	
N^{14}H_3 ARP									
200 Volt	360	.93	24	586	240	5143	-.71	.83	
100 Volt	180	.94	25	600	240	4500	-.72	.80	

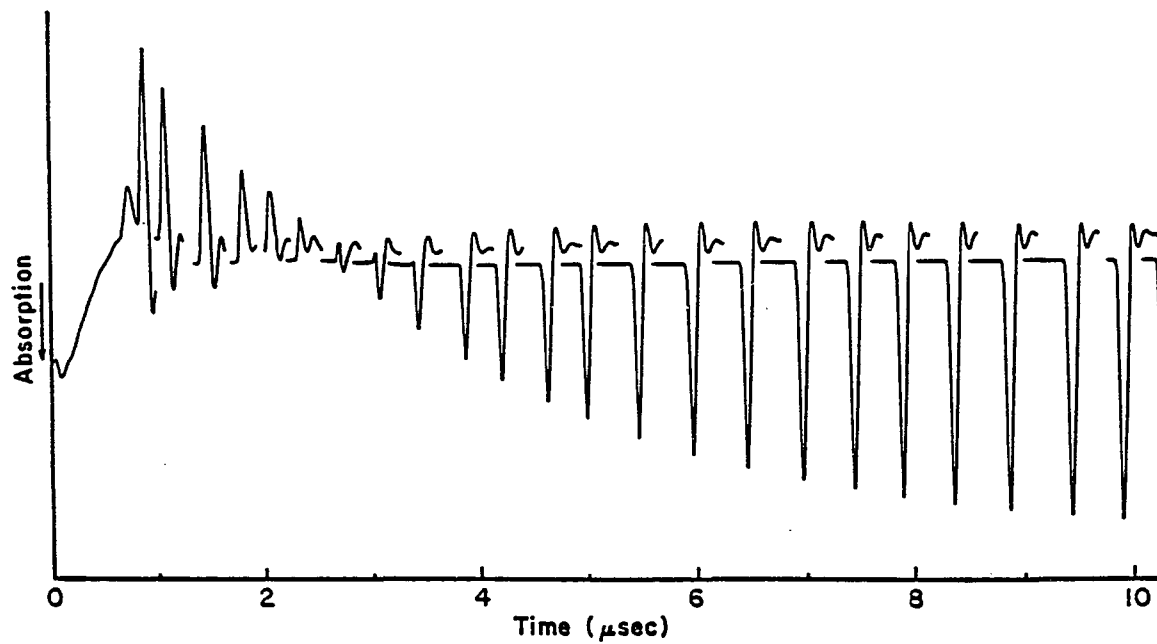


Figure 6.5. An x-y plot of an early ARP experiment.

Note that the zero amplitude "crossing point" displays a transient.

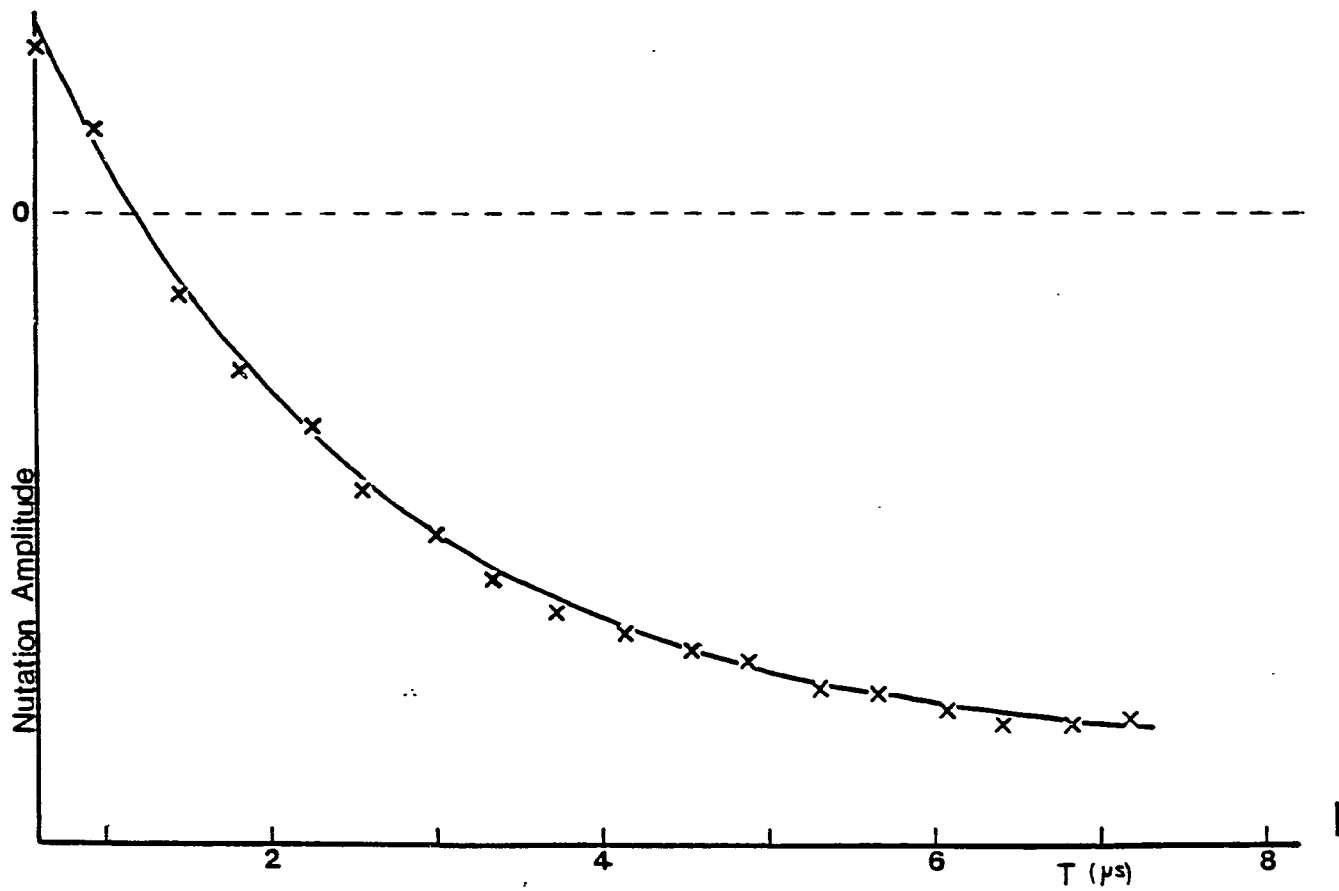


Figure 6.6. A plot of nutation data from $N^{15}H_3$ at 4mt and its simple exponential decay best fit curve.

Loy's work studied $N^{14}H_3$'s response over a pressure range from 8 to 40 mTorr. For each pressure, the decay appeared to be a simple exponential. Across pressure he found that the decay dependence was linear with a slope of $.035 \mu s^{-1} - mTorr^{-1}$. We note that microwave studies of the ground state have established a T_2^{-1} of $.176 \mu s^{-1} - mTorr^{-1}$ (Townes and Schalow, 1955; Wang et al., 1973) and that for closely spaced rotational manifolds, $T_1 = T_2/2$ (not T_2 as written in Loy's paper). We can equate $.352 \mu s^{-1} - mTorr^{-1}$ to Γ_b . Since our experiments were run in the 0.5 to 9 mTorr range, one would expect to see the pressure plots deviating from linearity or at least displaying a pressure dependent decay parameter intermediate to Loy's value ($\geq \Gamma_a$) and the short-time decay rate ($\frac{\Gamma_a + \Gamma_b}{2} > .176 \mu s^{-1} - mTorr^{-1}$).

Least-square best fits were applied to the data for simple exponential decays as in the previous work. It was found that a simple exponential decay fit the data quite well as indicated in Figure 6.6. Figure 6.7 shows the resulting decay rates versus pressure for the 100 volt ARP, 200 volt ARP, and 200 volt two-pulse experiments on $N^{14}H_3$. Figure 6.8 shows the same sort of plots for the $N^{15}H_3$ 100 volt ARP experiment and two sets of data taken by Van Stryland in 1976 using the two-pulse method. The results are tabulated in Table 6-3. The 200 volt ARP results for $N^{15}H_3$ are not listed as the results are very noisy due to detector preamp problems. However, the noisy data does appear to be centered about the 100 volt experimental results. From the figures, it is clear that the two techniques used are giving

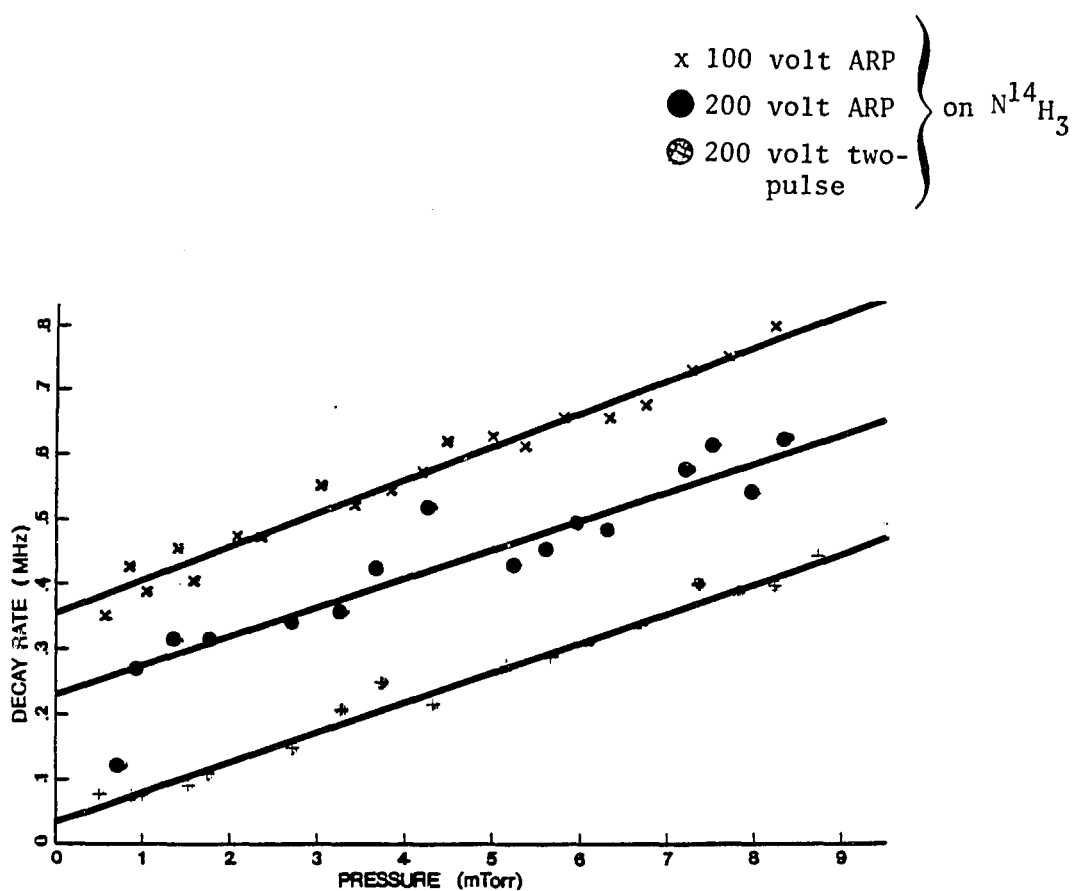


Figure 6.7. A plot of the least-squares obtained simple exponential decay/rate for each pressure run of the $N^{14}H_3$ experiments versus pressure.

$N^{15}H_3$:

- x Two-pulse-Van Stryland's unpublished data of 5/8/76
- 100 volt ARP
- ⊗ Two-pulse-Van Stryland's dissertation

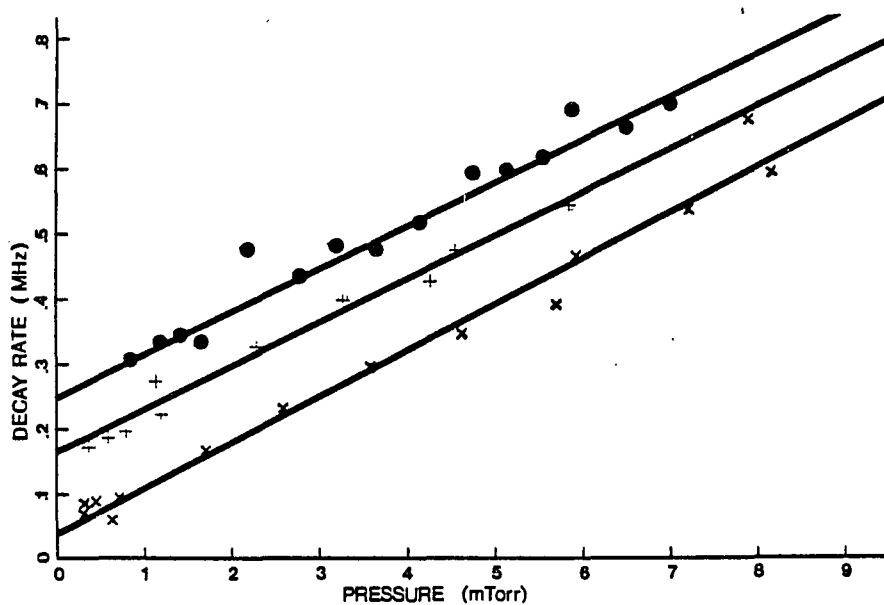


Figure 6.8. A plot of the least-squares obtained simple exponential decay/rate for each pressure run of the $N^{15}H_3$ experiments versus pressure.

similar results. Table 6-3 shows that the different experiments for the same molecules agree to within experimental error except for Loy's $N^{14}H_3$ result which is taken over different times and pressures. However, using Loy's value as the upper level decay rate, a nutation simulation over the times and pressures used here gives, upon the reduction, a decay rate which is not linear with pressure. This, coupled with the strongly simple exponential decay behavior with time and over pressure suggests that the above decay rate assumptions for NH_3 may not be valid.

Table 6.3 NH_3 Experimental Results

	Simple Exponential Decay Constant ($\times 10^{-2} \mu s^{-1} -mTorr^{-1}$)
1. 100 Volt $N^{14}H_3$ ARP	5.07 \pm .23
2. 200 Volt $N^{14}H_3$ ARP	4.38 \pm .29
3. 200 Volt $N^{14}H_3$ Two-Pulse	4.57 \pm .15
4. Loy's $N^{14}H_3$ Work	3.5
5. 100 Volt $N^{15}H_3$ ARP	6.64 \pm .34
6. Van Stryland's Data- $N^{15}H_3$ (from Dissertation)	6.68 \pm .36
7. Van Stryland's Data- $N^{15}H_3$ (taken 5/8/76)	7.05 \pm .26

Since error bars are not given for Loy's figure it is not clear to what degree his figure is truly off. Clearly, in all experiments done, nothing but a simple exponential decay has been indicated with a rate much less than the expected decay rate of the ground.

There is a significant difference between the $N^{14}H_3$ results and the $N^{15}H_3$ results. This is not in itself surprising. Though $N^{14}H_3$ and $N^{15}H_3$ are very similar, the transitions involved here are not. Due to the doublet structure of the lower levels of NH_3 , the levels involved in the optical transitions studied here are subject to decay via microwave rotational resonance (Townes and Schalow, 1955). In this decay mode, molecules' oscillating dipoles have a finite average interaction with each other because they are moving at the same rate. This effect is strongest for $J=K$. From this we would expect $N^{14}H_3$ to have a faster decay. Rotational resonance's contribution to the decay for a $J=6, K=6$ is about the same as that from a $J=3, K=3$ but much larger than that from a $J=3, K=2$ line. What we see though is that $N^{15}H_3$ decays faster. This is not at the present understood.

Conclusions and Discussions

These results suggest further work that can be done. The pressures used by Loy put him in the long time regime of equation (2.29). The present work was in what should have been, we believe, an intermediate regime. Yet, only simple exponential decay at rates much lower than have been observed. A study going down to lower pressures should be made to look for the characteristic change in decay rate. The present data gathering system in the laboratory can retrieve very weak signals. With very low pressures, gas breakdown is no problem so that larger Stark plate spacings can be used. This means that molecular transit effects in a two-pulse nutation experiment

can be reduced by using larger beam cross sections. In this way we can finally determine the point, if any, where the decay rate/pressure converges to a higher value, $\frac{\Gamma_a + \Gamma_b}{2}$. We could compare this obtained value to our expectations above. Further, as beam cross section effects on the nutation signal are smaller in the ARP excited case, the Stark plates can be reduced to a smaller than present spacing for work in the 10 to 40 mTorr range. With a narrow beam and the ARP method, Γ_a can be measured directly in a precise manner. In conjunction with the first experiment, we obtain measurements of both Γ_a and Γ_b . Also, if $\Gamma_a \neq \Gamma_b$, we would be able to resolve more clearly how $N^{15}H_3$ decays differently from $N^{14}H_3$ (i.e., does the difference in decay rates come from the upper level only or equally from both levels or in some other manner).

The present experiments demonstrate adiabatic inversion and that T_1 information obtained from it is consistent with the established two-pulse technique. These results failed to demonstrate any significant improvement in resolution though this should be possible with more care and practice. It is heartening that two radically different initial non-thermal conditions show good agreement.

LIST OF REFERENCES

- Abraham, A., The Principles of Nuclear Magnetism, Oxford University Press, London (1961).
- Alimpiev, S.S., and N.V. Karlov, "Photon Echo in the Molecular Gases BCl_3 and SF_6 ," Sov. Phys. JETP 36, 255 (1973).
- Alimpiev, S.S. and N.V. Karlov, "Nutation Effect in the Molecular Gases BCl_3 and SF_6 ," Sov. Phys. JETP 39, 260 (1974).
- Asawa, C.K. and T.K. Plant, "Wideband Modulation of the C^{13}O_2 Laser R(18) Line at $10.784\mu\text{m}$ with an N^{14}H_3 Stark Cell," Applied Phys. Lett. 30, 96 (1977).
- Berman P.R., J.M. Levy, and R.G. Brewer, "Coherent Optical Transient Study of Molecular Collisions: Theory and Observations," Phys. Rev. A 11, 1668 (1974).
- Christensen, C.P., C. Freed, and H.A. Haus, "Gain Saturation and Diffusion in CO_2 Lasers," IEEE J. of Quantum Electron. 5, 276 (1969).
- Feynman, R.P., F.L. Vernon, and R.W. Hellwarth, Geometrical Representation of the Schrodinger Equation for Solving Maser Problems, J. Appl. Phys. 28, 49 (1957).
- Freed, C., "Design and Short-term Stability of Single-frequency CO_2 Lasers," IEEE J. of Quantum Electronics 4, 404 (1968).
- Gordon, J.P., C.H. Wang, C.K.N. Patel, R.E. Slusher, and W.J. Tomlinson, "Photon Echoes in Gases," 179, 294 (1969).
- Gutman, W.M., and C.V. Heer, " SF_6 Photon Echo Polarization," Phys. Lett. 51A, 437 (1975).
- Gutman, W.M. and C.V. Heer, "Photon Echo Measurements in SF_6 and SiF_4 ," Phys. Rev. A 16, 659 (1977).
- Hamadani, S.M., A.T. Mattick, N.A. Kurnit, and A. Javan, "Observation of Adiabatic Rapid Passage Utilizing Narrow Infra-red Saturation Resonances," Appl. Phys. Lett. 27, 21 (1975).
- Heer, C.V. and R.J. Nordstrom, "Polarization of Photon Echoes from SF_6 Molecules," Phys. Rev. A 11, 536 (1975).

- Hocker, G.B., and C.L. Tang, "Observation of the Optical Transient Nutation Effect," *Phys. Rev. Lett.* 21, 591 (1968), and "Measurement of the Transition Moment by the Optical Transient Nutation Effect," 184, 356 (1969).
- Horwitz, P., "Population Inversion by Nonadiabatic Frequency Chirping," *Appl. Phys. Lett.*, 26, 306 (1975).
- Jauch, J.M., "The Hyperfine Structure and the Stark Effect of the Ammonia Inversion Spectrum," *Phys. Rev.* 72, 715 (1947).
- Keilson, J., and J.E. Storer, On Brownian Motion, Boltzmann's Equation, and the Fokker-Planck Equation, *Q. Appl. Math* 10, 243 (1952).
- Lehmberg, R.H. and J. Reintjes, "Generalized Adiabatic Following Approximation," *Phys. Rev. A* 12, 2574 (1975).
- Loy, M.M.T., "Observation of Population Inversion by Optical Adiabatic Rapid Passage," *Phys. Rev. Lett.* 32, 814 (1974).
- Lyman, J.L., R.G. Anderson, R.A. Fisher, and B.J. Feldman, "Absorption of Pulsed CO₂-Laser Radiation by SF₆ at 140 K," *Opt. Lett.* 3, 238 (1978).²
- McDowell, R.S., H.W. Galbraith, B.J. Krohn, and C.D. Cantrell, "Identification of the SF₆ Transitions Pumped by a CO₂ Laser," *Opt. Comm.* 17, 175 (1977).⁶
- Neckley, J.R. and C.V. Heer, "Photon Echoes from SF₆," *Phys. Lett.* 46A, 41 (1973).
- Namba, S. "Electrooptical Effect of Zincblend," *J. Opt. Soc. Am.* 51, 76 (1961).
- Patel, C.K.N., and R.E. Slusher, "Photon Echoes in Gases," *Phys. Rev. Lett.* 20, 1087 (1968).
- Sargent III, M., M.O. Scully, and W.E. Lamb, Jr., Laser Physics, Addison-Wesley, Reading, MA (1974).
- Shoemaker, R.L., In Laser and Coherence Spectroscopy, ed. J.I. Steinfeld, pp. 197-371, New York: Plenum, 1978.
- Shoemaker, R.L., R.E. Scotti, B. Comaskey, and J. Sotto M., "Design and Performance of a Frequency-switchable CO₂ Laser," to be published in 1982.

- Scotti, R.E. "Development of a Frequency-switched Laser for Infrared Time Resolved Spectroscopy," Ph.D. Thesis, Univ. of Arizona (1982).
- Shoemaker, R.L., and E.W. Van Stryland, "Direct Measurement of Transition Dipole Matrix Elements Using Optical Nutation," J. Chem. Phys. 64, 1733 (1976).
- Taylor, R.L. and S. Bitterman, "Survey of Vibrational Relaxation Data for Processes Important in the CO₂-N₂ Laser System," Reviews of Modern Physics 41, 26 (1969).
- Thomason, W.H., and D.C. Elbers, "An Inexpensive Method to Stabilize the Frequency of a CO₂ Laser," Rev. Sci. Instrum. 46, 409 (1975).
- Townes, C.H., and A.L. Schawlow, Microwave Spectroscopy, Dover Publications, Inc., New York (1975).
- Treacy, E.B., and A.J. DeMaria, "Adiabatic Inversion in the Infrared," Phys. Lett. 29A, 369 (1969).
- II-VI Data Sheet, "Materials for CO₂ and CO Laser Optics" II-VI Incorporated, Glenshaw, PA (1975).
- Van Stryland, E.W., "On High Resolution Spectroscopy: Theory and Experiment," Ph.D. Thesis, Univ. of Arizona (1976).
- Yariv, A., T.A. Nussmeier, and J.E. Kiefer, "Frequency Response of Intracavity Laser Coupling Modulation," IEEE J. of Quant. Elect. 9, 594 (1973).
- Yariv, A., Quantum Electronics, John Wiley & Sons, Inc. New York (1975).